Design and Optimization of Superconducting Magnet Systems for Energy Storage Application

By

UTTAM BHUNIA

(Enrolment No. PHYS 04200904008)

VARIABLE ENERGY CYCLOTRON CENTRE

Kolkata-700 064, India

A thesis submitted to the Board of Studies in Physical Sciences

In partial fulfillment of requirements

For the Degree of

DOCTOR OF PHILOSOPHY

of

HOMI BHABHA NATIONAL INSTITUTE

Mumbai

February, 2016

Homi Bhabha National Institute

Recommendations of the Viva Voce Board

As members of the Viva Voce Board, we certify that we have read the dissertation prepared by Uttam Bhunia entitled "Design and Optimization of Superconducting Magnet Systems for Energy Storage Applications" and recommend that it may be accepted as fulfilling the dissertation requirement for the Degree of Doctor of Philosophy.

Chairman: Prof. Saila Bhattacharyya S. Bhattacharyya Date: 26/2/16

Guide/Convener: Prof. Alok Chakrabarti Alok Chakrabarti Date: 26/2/2016

Examiner: Dr. Upendra Behera U. Behera Date 26/2/2016

Member: Prof. Parthasarathi Barat P. Barat Date: 26/02/2016

Member: Prof. Rajarao Ranganathan Date:

Technical Advisor: Shri Subimal Saha Date: 26/2/16

Final approval and acceptance of this dissertation is contingent upon the candidate's submission of the final copies of the dissertation to HBNI.

I hereby certify that I have read this dissertation prepared under my direction and recommend that it may be accepted as fulfilling the dissertation requirement.

Date: 26-02-2016

Alok Chakrabarti

Guide

Time:

STATEMENT BY AUTHOR

This dissertation has been submitted in partial fulfillment of requirements for an advanced degree at Homi Bhabha National Institute (HBNI) and is deposited in the Library to be made available to borrowers under rules of the HBNI.

Brief quotations from this dissertation are allowable without special permission, provided that accurate acknowledgement of source is made. Requests for permission for extended quotation from or reproduction of this manuscript in whole or in part may be granted by the Competent Authority of HBNI when in his or her judgment the proposed use of the material is in the interests of scholarship. In all other instances, however, permission must be obtained from the author.

UTTAM BHUNIA

DECLARATION

I, hereby declare that the thesis work presented has been carried out by me. The work is original and has not been submitted earlier as a whole or in part for a degree / diploma at this or any other Institution / University.

UTTAM BHUNIA

I dedicate this work to the memory of my Grand Mother

ACKNOWLEDGEMENT

I want to record my deep sense of gratitude and sincere thanks to my supervisor Prof. Alok Chakrabarti. This work would not have been possible without his guidance, support and encouragement. I am grateful to him for critically reviewing this thesis with comments and suggestions on almost every page despite of his busy schedule.

I take this opportunity sincerely thank and acknowledge the contribution of Dr. Rakesh Kumar Bhandari, Former Director, VECC, who has also been my first research supervisor and encouraged me to take up this research work.

I am grateful to the members of my dissertation committee for their helpful suggestions, and critically evaluating my research activities during my progress report presentations. I must pay my gratitude to Shri Subimal Saha, my technical advisor, for his keen interest to develop SMES system in the centre and the infrastructural support that was wholeheartedly provided. I would like to record my sincere thanks to Prof. Jane Alam, Dean (Science), HBNI for his unstinted effort to get the thesis examined in time.

I convey my sincere thanks to Shri Chaturanan Mallik, Former Head, Accelerator Physics Group, VECC for his moral support.

I am privileged to work with my senior colleague Shri Amitava Sur, who has been mentor for me ever since I joined the department. I acknowledge

my sincere and heartfelt gratitude to him for his generous help at any point of time.

I convey my sincere gratitude to Shri Gautam Pal, Head, Mechanical Engineering group, VECC for his scientific and technical advice in many occasions.

I could not have succeeded to carry out this work without the invaluable support of my colleagues Jedidiah Pradhan, Samit Bandopadhaya, Anirban De, Anindya Roy, Sajjan Kumar Thakur, Umashankar Panda, V. K. Khare, C S Prasad, and S K Bose. Special thanks are due to Chinmay Nandi and Javed Akhter for helping in Quench Analysis with OPERA-3D code and fatigue analysis for 4.5 MJ system. I express my sincere gratitude to Dr. Sandip Pal and colleagues of cryogenics plant for kindly providing cryogens and allied cryogenic facilities.

I convey my sincere thanks to Dr. Malay Kanti Dey, Head, SCBD, for his kind support all through and also for proofreading the thesis into a presentable shape. Special thanks are due to my dear colleagues Jayanta Debnath, Santanu Pal, Zamal Abdul Naser, Atanu Dutta, Vinay Singh, Chiranjib Das, Tanmay Das, and Ankur Agarwal and many more for their unconditional support. I would acknowledge the contribution of my friend Dr. Subhasish Rana, who has helped me in many ways right from paper writing to thesis completion.

I would like to pay my sincere gratitude to all my teachers who has taught me right from my school days and provided their blessings.

On a more personal level, I am grateful to my family members for their heartful support without that I could not have done this work. A special memory is to my grandmother Rajlaksmi Bhunia, who would have been very proud of this achievement. I am extremely thankful to my wife Subhra for all her support and understanding.

Finally, I express my gratitude to all persons who have not been listed here but helped to complete this work.

February, 2016 *Uttam Bhunia*

CONTENTS

SYNOPSIS

The Superconducting Magnetic Energy Storage (SMES) is a contemporary field of research having promising solutions for achieving high quality power that is required for many applications including accelerators. This thesis deals with SMES and consists of two parts. The first part describes the design, development and test results of a 0.6 MJ solenoid-type SMES system integrated with power-conditioning system. The second part describes design of two different configurations (solenoid-type and sector toroid-type) of a 4.5-5.0 MJ SMES system, where a novel approach of design optimization based on Differential Evolution algorithm has been adopted. Based on these studies, the toroid-type design has been chosen for future development.

The quality of power is one of the most important issues in power distribution systems. The quality of power is a stringent requirement in case of special voltage-sensitive electrical equipments, such as, compressor units in the cryogenic refrigeration facility in a large accelerator complex, critical industry processes including those that employ embedded processors or microcontrollers, *etc.* because of their sensitivity to any voltage sag or short interruptions in supply. There are various kinds of problems that can occur in electrical networks, such as, transient over-voltage, voltage sags, voltage harmonics, supply interruption, *etc.*

The voltage sag has the consequence of long restart time, lower production, machine disturbances or defects, *etc.* According to statistics by Electric Power Research Institute (EPRI), USA, the major interruption (more than 90%) in utility line occurs primarily due to voltage sags with duration of less than 1 second. The depth and duration of voltage sags depend on many factors such as the local network characteristics, faults and switching events in the grids, loads and their under voltage behavior, *etc.* Although uninterrupted power supply (UPS) has been widely used to maintain the power quality, it has several problems such as short life time of batteries, environmental problems caused by the chemicals, and requirement of large space. The SMES system is known to be a very good energy storage device and provides a promising solution for the voltage sag or short time power interruption problem since it has large energy storage density, ability to discharge large amount of power in a small amount of time (fast energy discharging capability), unlimited charging-discharging cycle, *etc.* The other diverse applications of SMES include load leveling, frequency regulation, enhancement of transmission capability, uninterrupted power supplies, *etc.*

The technical basis of SMES systems had its beginning in 1911 when superconductivity was discovered by Kammerlingh Onnes. A SMES system stores the energy as magnetic energy in a superconducting magnet cryogenically cooled, achieving a system with negligible loss. The SMES system is primarily composed of superconducting magnet with its mechanical support structure and current leads, a cryogenic system (cryostat, closed cycle cryogenic refrigeration unit, vacuum pump, *etc.*), a fairly sophisticated AC-DC power conditioning system (PCS) that interfaces between the superconducting magnet and loads, and a controller. The PCS that consists of a DC-DC chopper and a three phase voltage source converter (VSC) is the interface between SMES coil and power system. The desired charge and discharge requirement of SMES coil is achieved by controlling the duty cycle (D) of chopper circuit. Research and development of SMES system has been carried out to realize efficient electric power mitigation for several decades. The primary difficulty of SMES systems that limits its application is its investment and operating cost to maintain cryogenic temperature. One possibility to reduce the operating cost is to use high temperature superconductor (HTS) based SMES system has been focused on conduction-cooled operation at about 20 K. However, commercially available HTS are not yet technically feasible for large AC or transient application as required in SMES operation. Moreover, a higher critical current density and better mechanical performance is desired to reduce the investment cost. After the commercial availability of 4 K cryo-refrigerator in recent years, it has been found that NbTi based low temperature superconductor (LTS) along with helium re-condensing technology is still far better choice for small scale SMES development compared to (HTS) as far as operational reliability and capital investment are concerned. Variable Energy Cyclotron Centre (VECC) at Kolkata has taken up research and development program of SMES technology capable of mitigating voltage sags. In this thesis, work is pursued to develop optimization approaches for designing the SMES system and to establish the correlation among the geometrical and operating parameters of the same, in context of investment cost and performance reliability.

The selection of appropriate superconducting cable and the cooling technology are very important in developing a reliable SMES system. In VECC SMES project, it is planned to use both cryostable superconductor with high copper to superconductor ratio as well as non-cryostable conductor. A cryostable conductor provides very good stability against magnetic field transient but contributes a large transient loss due to higher copper to superconductor ratio (~10:1 or more). The cryostable conductor has been used in a laboratory scale 0.6 MJ SMES system in the centre. On the other hand, for a non-cryostable conductor transient loss is quiet low because of lower copper to superconductor ratio ($\leq$ 2:1). In this case, sufficient stability margin needs to be kept along with a fail-safe quench protection system. In the designing of a 5 MJ SMES system, the non-cryostable Rutherford-type cable has been chosen, since it offers relatively lower AC loss. The system will be liquid helium bath cooled using cryo-refrigerator based recondensation technology.

The SMES magnet design includes design of the coil, quench detection and protection system, cooling system and magnet cryostat. There are two traditional cooling methods: one is bath cooling (liquid helium pool boiling) method, where coil is dip in liquid helium and the other is forced pressure cooling method (supercritical helium), each having its own merits and demerits. For small scale SMES system, liquid helium bath cooling provides a more economic solution.

A liquid helium bath cooled 0.6MJ / 0.1 MW SMES system using cryostable conductor, integrated with the power-conditioning system, has been designed, developed and tested for carrying out research on the interaction between SMES and electrical power system. There are several design issues of a SMES magnet, including the amount of stored energy, operating temperature, operating current, cooling method, operating cost, conductor stability against fast field-transients, *etc.* The essential basis of the design is the critical characteristics of the particular superconductor at the operating temperature. The thesis-work includes a detailed magneto-structural analysis of the system to determine minimum winding tension that ensures radial compressive stress of the coil in all possible scenarios. A passive shielding made of ferromagnetic material has been used to reduce the stray magnetic field outside the cryostat down to an acceptable limit. The primary objective of this development is to study the issues like AC loss in superconductor, eddy loss in coil former, *etc.*, related to high magnetic field transients. Various parameters of the magnet coil have been optimized to maximize the stored energy and minimize the capital cost in terms of conductor length. A protection scheme with modular type air-cooled dump resistors and three-channel quench detection circuit (QDC) have been used. The effect of eddy current induced force on helium vessel has also been investigated to ensure that helium vessel remains safe against any buckling. Niobium-tin (Nb_3Sn) sandwiched in copper bus bar is used to reduce the steady state heat load from vapor-cooled current leads. The coil is initially energized to its nominal operating current (800 A) and magnet load line is found. Finally, the system is connected to the load through the power conditioning unit and voltage sag compensation of various magnitudes is demonstrated. The voltage-sags of about 80% depth of the utility line (440 V, 3Ø) with duration of several cycles up to 2 seconds have successfully been compensated.

Further, feasibility of developing a 4.5-5.0 MJ/1MW SMES system using 4.2 K cryo-refrigerator based liquid helium re-condensation capable to mitigate voltage sags in critical components in our accelerator complex has been studied in the thesis. Two configurations of superconducting coil system, a solenoid-type and sector toroidal-type geometry with niobium titanium (NbTi) alloy based non-cryostable low temperature superconductor (LTS) operating at 4.2 K temperature are considered. The solenoid coil has advantages of higher stored energy per unit length of conductor, simple structure, but produces leakage magnetic field surrounding it. The toroidal-type system has the low magnetic flux leakage compared to solenoid-type SMES of the same energy storage capacity. Therefore, from electromagnetic compatibility issue the toroidal system is becoming more and more attractive to SMES designers. However, it requires a complicated mechanical structure and cryostat since effective electromagnetic force in each sector coil is inward towards the center of the torus.

The critical characteristics $(I_c - B)$ of the cable are measured at the operating temperature of 4.2 K. The operating current density (J) is determined from the measured critical characteristics data of the superconducting cable (i.e. J_C vs B), considering the space or filling factor of the coil and the safety margin factor at the coil peak field (B_m).

For small scale SMES system the operational cost is mainly due to AC loss and steady-state loss in to the magnet cryostat. A novel generalized approach has been developed to minimize overall cryogenic refrigeration load for solenoid-type coil during fast discharge operation, considering the practical engineering constraints such as electromagnetic stress, stability margins, *etc*. Both the AC loss in superconductor and steady state load in the cryostat due to radiative heat flux and current leads at operating temperature of 4.2 K have been considered. This work gives an analytical formulation of the optimization problem in terms of coil parameters and aims to minimize cryogenic refrigeration load into the cryostat using differential evolution (DE) algorithm. The dynamic loads are primarily due to eddy loss in strands (inter-strand and intra strand loss), loss due to crossover resistance (adjacent crossover and transverse crossover) and hysteresis loss in the superconducting filaments. The optimal design of 5 MJ class SMES coil using Rutherford-type cable is discussed as a case study. The variation of the refrigeration load and coil's geometric parameters (α, β, a) are also investigated as a function of allowable hoop stress in the winding and maximum allowable voltage across the coil.

A multi-objective optimization design approach for sector toroidal superconducting magnetic energy storage coil has been developed considering the practical engineering constraints. The objectives include the minimization of necessary superconductor length and torus overall size, which determines a significant part of capital cost. Unlike the single objective optimization, the solution of multi-objective optimization problem is not a single point, but a set of non-dominating points, known as Pareto optimal solution. The best trade-off between the necessary conductor length for winding and magnet overall size for different number of sector coils is achieved in the Pareto-optimal solutions. Compactness of the magnet leads to increase in required superconducting cable length or vice versa. The final choice from the Pareto optimal configurations and selection of number of sectors are done considering other issues such as AC loss during transient operation, stray magnetic field outside the coil assembly, available discharge period, *etc.* The iso-gauss contour line of 0.5 mT, which is the average earth magnetic field and is considered to be the safe stray field for human health, is found in the equatorial plane of torus at a distance of 2.0 m away from torus center for eight sector configuration. The best feasible Pareto solution for the 4.5 MJ / 1MW system is determined (*major radius* = 0.62-0.67 m) considering the practical engineering aspects without losing the optimality. Furthermore, the validity of the representative Pareto solutions is confirmed by finite-element analysis (FEA) with a reasonably acceptable accuracy.

The thesis also includes 3D design analysis of an eight-sector toroidal magnet using commercially available FEA code (ANSYS Multiphysics). The magnet system consists of eight superconducting solenoid coils made of custom-make NbTi based Rutherford-type cable and arranged in toroidal fashion with finite inter-sector gap. The coils will be epoxy impregnated and liquid helium bath cooled at 4.2 K. Since the strong electromagnetic force distributed to the coil is asymmetric and non-uniform in nature around the coil azimuth, a precise 3-D finite element analysis has been carried out to study the behaviour of circumferential or hoop stress, radial stress and von Mises stress under various operational scenarios. The objective of the magneto-structural study is to ensure that equivalent stresses (von Mises stresses) of all the component materials never exceed the yield stress; all parts of the coil remain in compression at full excitation, and maintain compression between innermost layer of the coil and outer surface of the bobbin under various operational scenarios. The results reveal that maximum stress developed on coil and its support structure is below allowable stress limit. During its life time, the SMES will be subjected to many numbers of cycles of charging and discharging. Therefore, fatigue life assessment is a critical part of the design. The various approaches to fatigue assessment are: stress life, strain life and fracture mechanics. Stress life is based on the S-

N (Stress vs. Number of cycles to failure) curve and is suitable for high cycle fatigue. Strain life approach is particularly suitable for low cycle fatigue, and is typically concerned with crack initiation. Fracture mechanics starts with an assumed flaw and determines the crack growth. For the purpose of present analysis, the strain life approach is used to determine the number of cycles before a crack is formed. After the stress distribution from the static stress analysis, the fatigue life is obtained using strain-life equation and equation for cyclic stress strain curve. The fatigue analysis during operation of SMES is very important so as to suitably select the structural material and ensure that coil is safe under fatigue failure.

Magnetic field transient analysis has also been carried out to evaluate transient loss and assess the feasibility of using helium re-condensation technology with commercially available cryo-refrigerators. The total transient loss comprising of both the AC loss from superconductor and the eddy loss from coil former along with support structure would be around 1000 J at 4.2 K (considering about 25 % contingency) and must be handled by cryogenics system. This energy is equivalent to boil-off of 0.4 liter of liquid helium. If the discharge occurs eight times a day, this provides an additional heat load of 2% to the steady state heat load. The steady state load to the helium chamber is calculated to be around 2.0 W at 4.2 K. It is proposed to have three numbers of two-stage Gifford-McMahon (GM) type cryo-refrigerator (1.5 W at 4.2 K each) to mitigate both transient and steady state load. The total heat load (steady state and transient) on the intermediate thermal shield around the liquid helium system is about 180 W at 60 K. This is within the capacity of a standard commercially available single-stage cryo-refrigerator. In adiabatic situation, the maximum temperature rise of thermal shield during transient of 200A/s (1.2 T/s) is found to be less than 0.3 K. The mechanical von Mises stress developed on the intermediate shield due to interaction of induced current density and magnetic field for the maximum field transient is found to be about 6.2 MPa, which suggest that the thermal shield would be safe from any structural deformation.

Finally, quench protection scenario has also been investigated for this toroidal-type SMES system. Sector coils are electrically interconnected in series. In case of quench like fault in one coil, magnet safety requires that temperature and voltage developed during a quench remains below certain level. The stored energy either is to be extracted or distributed uniformly in coils at the onset of quench by suitable quench protection scheme. One important requirement in the circuit arrangement is to maintain electromagnetic forces balanced azimuthally and vertically during a quench. The self and mutual inductance matrix among the sector coils is computed by calculating the internal energy and interaction energy of neighboring coils respectively. The three-dimensional heat balance equation is solved with circuit element to study quench propagation behavior between turns. OPERA-3D Quench code is used to understand and finalize the quench protection scheme. A viable electrical connection scheme for quench protection is developed. Heater induced active quench protection in fail-safe mode is found to be better option for quench protection ensuring no magnet damage.

A major part of the work included in this thesis is published in peer reviewed journals.

LIST OF PUBLICATIONS

[1] **U. Bhunia**, S. Saha, A Chakrabarti, "Design optimisation of superconducting magnetic energy storage coil", *Physica C*, **500** (2014) 25-32.

[2] **U. Bhunia**, S. Saha, A Chakrabarti, "Pareto-optimal design of sector toroidal superconducting magnet for SMES", *Physica C*, **505** (2014) 6-13.

[3] **U. Bhunia**, J. Akhter, C. Nandi, G. Pal, S. Saha, "Design of a 4.5 MJ/1MW sectored toroidal superconducting Energy storage magnet", *Cryogenics*, **63** (2014)186-198.

[4] **U. Bhunia,** J. Pradhan, A. Roy, V. Khare, U. S. Panda, A. De, S. Bandopadhaya, T. Bhattacharyya, S. K. Thakur, M. Das, S. Saha, C. Mallik, R. K. Bhandari, "Design, Fabrication and Cryogenic Testing of 0.6 MJ SMES Coil", *Cryogenics*, **52** (2012) 719-724.

LIST OF FIGURES

LIST OF TABLES

SYMBOLS AND ACRONYMS

	Description
l	Half length of solenoid coil, m
N_s	Number of sector or elemental coils
a/b	Solenoid coil inner/outer radius, m
a/b	Superconductor dimension, m
r_0	Major radius, m
$r_1/ r_2/ r_c$	Inner/outer/mean radius of sector coil, m
h	Length of each sector coil, m
h	Heat transfer coefficient, $Wm^{-2}K^{-1}$
α	Geometry dependent factor , r_1/r_0
α	Geometry dependent factor , b/a
β	Geometry dependent factor , r_2/r_0
β	Geometry dependent factor , l/a
d	Minimum inter-sector gap, m
B_m	Peak magnetic field in the winding, T
E	Stored energy in the magnet, J
J_{op}	Overall average operating current density, A/m^2
I	Operating current, A
I_c	Critical current, A
J_c	Critical current density, A/m^2
A_c	Conductor cross section ($a \times b$) area, m^2
n_r	Number of winding layers in sector coil
n_y	Number of turns in each layer of sector coil
n_f	Number of filaments in a superconducting strand
$\lambda_r / \lambda_y / \lambda$	Radial/axial/overall filling factor for coil winding
ζ	Operational margin factor
σ_c	Maximum hoop stress in the winding, Pa
L	Conductor length, m

t_s	Discharge or carry over period, s
V_{DC}	Voltage across DC link of chopper circuit, V
$V_i/V_m/\ V_{SMES}$	Voltage across SMES Coil, V
V	Winding volume, m^3
D	Duty cycle of chopper circuit
d_f	Diameter of each filament, m
P_0,P	Peak/ Rated power output to the load, W
$C(T)$	Specific heat per unit volume of composite material, $Jm^{-3}K^{-1}$
$\rho_m(T)$	Electrical resistivity of matrix material, Ω-m
T_{max}	Maximum peak temperature after quench, K
Top/T_b	Operating/ bath temperature, K
$T_c/\ T_{cs}$	Critical/ current sharing temperature, K
r_{cu}	Copper to superconducting ratio in the conductor
$L_1/L_2/L_{SMES}$	Self inductance of coil, H
M	Mutual inductance, H
M	Magnetization of superconducting filaments. Am^{-1}
k	Thermal conductivity, $Wm^{-1}K^{-1}$
A	Superconductor cross-sectional area, m^2
A_f	Superconductor filament cross-sectional area, m^2
S	Surface area, m^2
l_{MPZ}	Minimum propagation length, m
μ_0	Free space permeability, $4\pi\times10^{-7}\ Hm^{-1}$
$\dot{q}$	Heat flux, Wm^{-2}
h_l	Latent heat of evaporation, Jm^{-3}
σ_r/σ_θ	Radial/azimuthal stress, Pa
u	Displacement, m
υ	Poisson's ratio
Y	Young modulus, Pa
$\varepsilon_r/\varepsilon_\theta$	Radial/azimuthal strain
R_d	Dump resistance, Ω
E_θ	Electric field, Vm^{-1}
P	Eddy loss, W

p	Eddy loss, Wm^{-1}
$k_1=Y_f/Y_t$	Ratio of Young moduli
N	Number of cycles corresponding to fatigue
N	Element shape function
$K_{i,j}$	Stiffness matrix elements
R	FEA load vector/ Resistance, Ω
R_a	Adjacent resistance of Rutherford cable, Ω
R_c	Crossover resistance of Rutherford cable, Ω
U	FEA degree of freedom (DOF)
SMES	Superconducting Magnetic Energy Storage
CAES	Compressed Air Energy Storage
BESS	Battery Energy Storage System
FES	Flywheel Energy Storage
CICC	Cable-In-Conduit-Conductor
WIC	Wire-In-Channel
LTS	Low Temperature Superconductor
HTS	High Temperature Superconductor
PCS	Power Conditioning System
IGBT	Insulated Gate Bipolar Transistor
VSI	Voltage Source Inverter
RRR	Residual Resistivity Ratio
MQE	Minimum Quench Energy
MPZ	Minimum Propagation Zone
QDC	Quench Detection Circuit
VSC	Voltage Source Converter
DSP	Digital Signal Processing
DVR	Dynamic Voltage Restorer
DE	Differential Evolution
EPRI	Electric Power Research Institute, USA
AC	Alternating Current
DC	Direct Current

CHAPTER 1

INTRODUCTION

With the advent of superconducting magnet technology, commercially available 4.2 K cryo-refrigerators and the power conditioning system, superconducting magnet based energy storage device has become a very attractive option to prevent interruptions in power system, voltage fluctuations, compensation for load, and so on. This chapter outlines the essential components of a magnetic energy storage device and the issues related to its design and development. A brief discussion has been presented on the algorithm for magnet design optimization, used further in this thesis work.

1.1 Energy Storage Technology

Energy storage has long been recognized as a potential method to improve voltage stability, frequency control, reactive power compensation, and to provide rapid response power during momentary faults or complete power outage in utility line. Among these, voltage sags are the most common. Voltage sags lead to significant and serious consequences such as frequent shut down, large down time, unexpected maintenance period, production loss, *etc.*, in industrial manufacturing sectors as well as in large accelerator based scientific research facilities and nuclear fusion power plants. A survey by Electric Power Research Institute (EPRI), USA, over a period of years from 1992 to1997, reveals that major interruption occurs primarily due to voltage sags with duration of less than 1 second [1], as shown in Figure1.1.

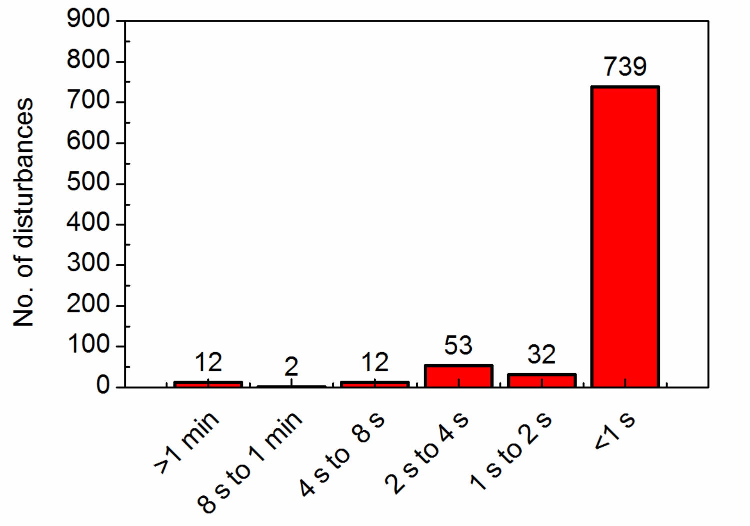

Figure 1.1: Power quality statistics surveyed by EPRI, USA, for a typical facility over 6 years [1].

Several energy storage technologies are currently being developed worldwide, *e.g.*, Compressed Air Energy Storage (CAES), Battery Energy Storage System (BESS), Superconducting Magnetic Energy Storage (SMES), Flywheel Energy Storage (FES), *etc.*, for power quality mitigation. The time response of different energy storage systems depend on the physical principle on which they are based. For instance, the speed to store and deliver energy for a FES system that is driven by rotational motion of high speed rotor, is typically much slower than a SMES system that is based on the principle of storing magnetic energy. A SMES system will be able to store energy more efficiently and its fast response is more suitable for voltage-sag mitigation with durations of the order of seconds as compared to conventional energy storage system. For different energy storage requirements there could be various types of SMES: 1000 MJ to 5000 MJ for large scale SMES, 100 kJ to 1 MJ is termed as micro-scale SMES and the capacity in between is known as small-scale SMES. Depending on the stored energy capacity, the application of SMES system could be summarized as shown in Figure 1.2.

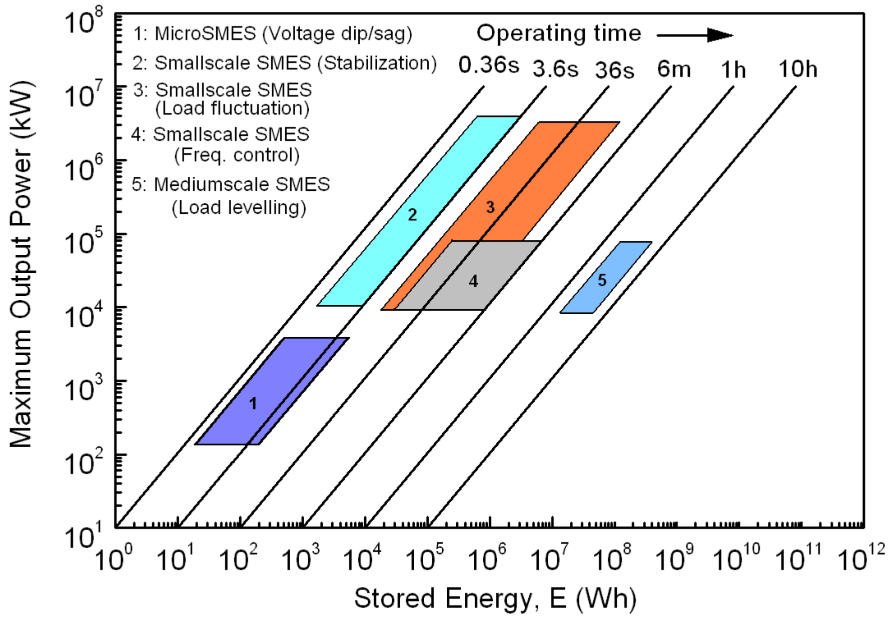

Figure 1.2: Application of SMES system with different capacity of stored energy and power output [2].

Advances in superconducting technology and power electronic devices led to improved performance characteristics of SMES system such as rapid response time (~ms), high power (~MW or more), high efficiency, *etc.* A SMES coil can also endure a high frequent cycle (thousands of charging/discharging cycles), which corresponds to several decades of operation. Further, SMES system is a promising device and offer flexible, reliable and fast-acting power compensation to active and reactive loads. Successful implementation of SMES devices requires extensive study to identify and solve the technological challenges with respect to the superconducting magnet, allied cryogenic system, power conditioning and control system. Development scenario of SMES and its perspective in recent years has been discussed in details by P. Tixader [3].

1.2 History of SMES Technology Development

The technological basis for SMES system had its beginning in 1911 by Hein Kammerlingh Onnes at the University of Leiden in Netherlands when he discovered superconductivity.

Serious interests in SMES began in 1960's by several groups in USA, Japan and Europe [4-5] after the low temperature superconductors became commercially available. The practical commercial demonstration of world's first 30 MJ/ 10 MW SMES system [6] using NbTi cable was done by Los Alamos National Laboratory (LANL), USA, along with Bonneville Power Administration (BPA) in early 1980for damping power oscillation in the Tacoma substation. The SMES system was of solenoid coil configurations made of NbTi superconductors. Afterwards, several small and medium scale SMES systems were developed in USA. AMSC (American Superconductor, USA) installed six SMES units in the grid of northern Wisconsin, USA, to improve its stability [7] in 2000. A 2.4MJ/1.4 MW SMES unit was installed in Brookhaven National Laboratory (BNL), USA, to offer high quality power for synchrotron radiation source. A 100 MJ/50 MW system [8] is developed and commissioned at Center for Advanced Power Systems (CAPS) by Florida State University (FSU) in collaboration with EPRI, USA, using cable-in-conduit-conductor (CICC) in 2003.

Other countries have also developed several SMES systems. The 2MJ Low Temperature Superconductor (LTS) based solenoid type SMES unit was built by Accel Instrument, Germany [9] in 2000 is one among those. SMES has been developed as national projects in Japan [10-13] since 1991 for compensation of load fluctuation and subsequently several SMES systems were built. A 10 MJ SMES system was developed in 2003 by Chubu Electric Power, Japan and now in operation using NbTi conductor at 4 K. A 20 MJ/10 MW SMES prototype [14] for a 100 MW commercial system was developed by New Energy and Industrial Technology Development Organization, Japan. Korea Electrotechnology Research Institute (KERI) has developed a 3MJ/750 kW SMES [15] system to improve the power quality in sensitive electric loads in 2005.

Several High Temperature Superconductor (HTS) based SMES projects have been taken up on R&D basis in USA, Japan, Korea, and China. However, due to anisotropy and immature HTS magnet technology, SMES development with HTS is relatively few in comparison to LTS SMES. American Superconductor Corporation (ASC) developed first HTS based 5 kJ SMES for research purpose in 1996. Chubu Electric Power in Japan developed a 1MJ/1 MW HTS (Bi-2212) SMES unit in 2004. KERI has also developed a conduction cooled solenoid type 600 kJ SMES with first generation (1G) HTS (Bi-2223) pancake winding in 2008 [16]. In Korea, further a toroidal-type 2.5 MJ SMES is under development by KERI using second generation (2G) HTS (YBCO-123) tape [17]. Recently, Li Ren et al. [18] in China has developed a movable HTS SMES system 150 kJ range/ 100 kW SMES unit using HTS tapes in 2015.

To summarize, the power conditioning technology has become quite mature due to advances in semiconductor technology and of course due to continuous research effort worldwide. However, till date the major limitations of commercial SMES development for voltage dip mitigation or large load leveling are the superconducting coil and allied cryogenics. In fact, it is found that the 75-85% of total investment cost in SMES development is solely due to superconducting coil and allied cryogenic facility. Further, the superconducting coil and cooling technology could be different for different energy storage capacity, power rating and discharge period. Therefore, the design parameters of a SMES system need to be optimized considering practical engineering constraints for different ranges of applications, thus minimizing the capital as well as running cost.

1.3 General Description of SMES System

A SMES system stores the magnetic energy in a superconducting magnet, hence having negligible loss. The SMES system is primarily composed of a superconducting magnet with its mechanical support structure and current leads, a cryogenic system (cryostat, closed cycle cryogenic refrigeration unit, vacuum pump, *etc.*), an AC-DC power conditioning system (PCS) that interfaces among the superconducting magnet, loads and controller, as schematically shown in Figure 1.3.

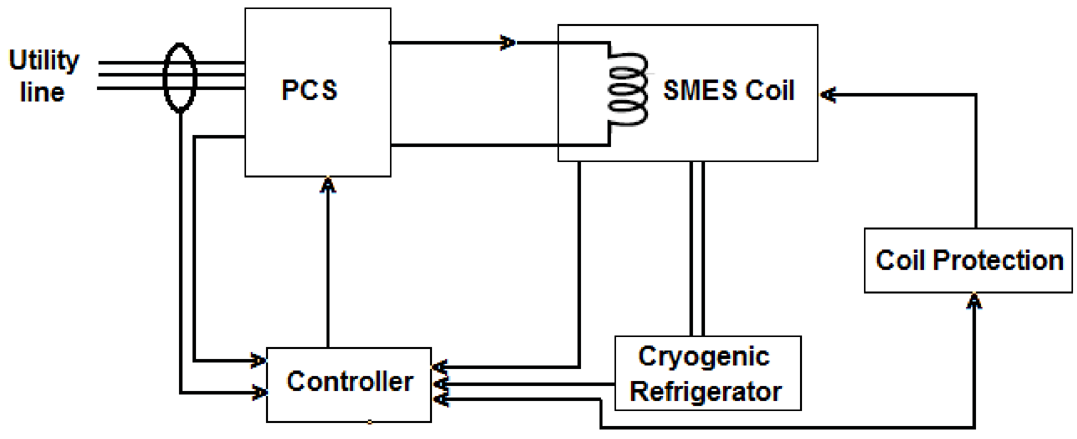

Figure 1.3: Schematic of a typical SMES system.

The magnetic energy stored in a superconducting magnet of inductance L_{SMES} and at operating current I is given by

$$E = \frac{1}{2\mu_0}\int_V B^2 dV = \frac{1}{2} L_{SMES} I^2 \tag{1.1}$$

Maximum power (P) delivered to the load is given as

$$P = \frac{dE}{dt} = L_{SMES}\, I \frac{dI}{dt} \tag{1.2}$$

The maximum energy stored in an inductive device and its power rating is, thus, dependent on its ability to carry very high current. The rating of the SMES system depends on the type of application. The cryogenic system is required to maintain the operating temperature of the superconducting magnet. The design of insulation and protection system of the SMES coil plays an important role during its transient mode of operation. During transient operation the high voltage developed in between turns or across the coil terminals requires sufficient insulation.

According to main circuit topology of power electronic converter, the SMES is classified into current source and voltage source. The voltage source converter is currently more matured technology and having lower cost to implement. In the voltage source configuration, the PCS consists of an input filter, rectifier/inverter unit using Insulated Gate Bipolar Transistor (IGBT), a two quadrant DC-DC chopper using IGBT. The DC-DC chopper is mainly used to keep the current through the SMES coil near-constant and to transfer the power to the Voltage Source Inverter (VSI) through the DC link capacitor. This DC link capacitor acts as a temporary DC voltage source to inject active/reactive power into the utility line. The VSC based circuit topology of the voltage-sag compensation system followed at Variable Energy Cyclotron Center (VECC), Kolkata, is as shown in Figure 1.4. The coil is charged or discharged by making voltage across the DC bus V_{DC} positive or negative.

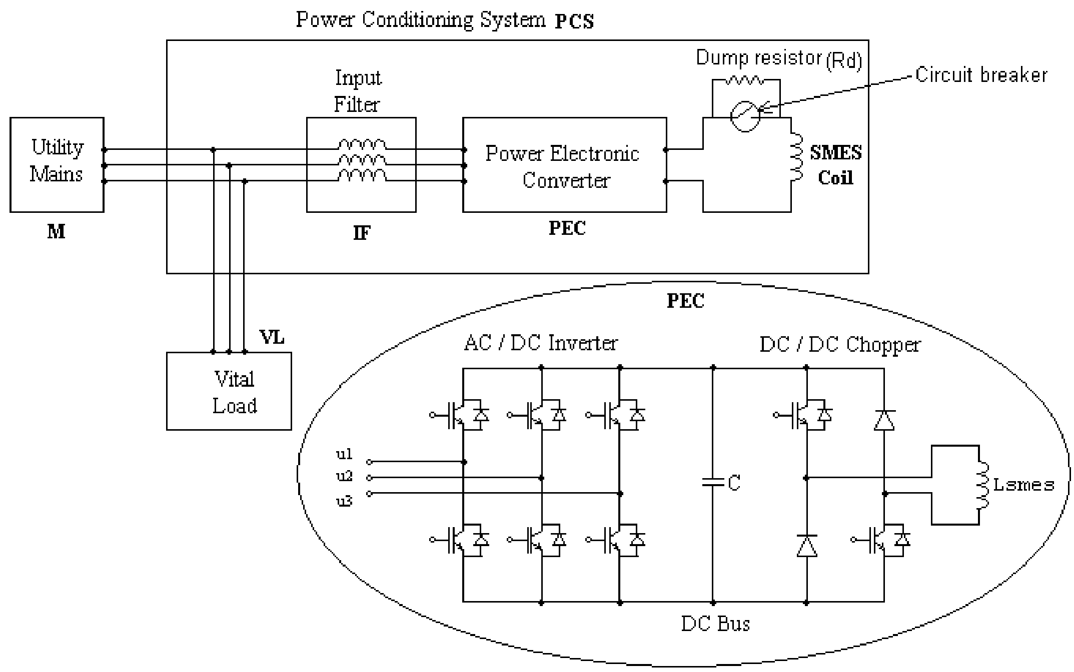

Figure 1.4: Basic circuit topology of SMES system at VECC, Kolkata.

The overall performance of a SMES system is determined by the performances of its major components, *viz.*, the controller, the superconducting magnet along with its cryogenic system and power conditioning system. The control system supervises both the converters (AC / DC Inverter and DC / DC Chopper) independently in real time according to the operating condition. For that the controller has to monitor selected parameters in the main load connection to choose the proper control strategy. Hence three main tasks that are to be realized by the control system:

- Detection of the Operation condition of the PCS
- Control of AC / DC Inverter
- Control of DC / DC Chopper

The controller uses digital signal processing that is very fast and has enough peripherals to control both the inverter chopper and measure all the required signals of the mains and load. Suitable safety interlocks also need to be implemented considering various operational scenarios for the reliable performance of SMES system.

1.4 Design Issues of Energy Storage Magnet

A number of mutually conflicting issues need to be considered while designing a superconducting magnet for fast acting, small-scale energy storage system for voltage-sag mitigation. The study needs to be focused on transient application as required in SMES. The primary factors need to be considered in the design of the coils to achieve best possible performance of a SMES system are as follows:

1.4.1 Choice of Superconducting Materials

The selection of superconducting material plays a key role in the design of a SMES system. The phenomena of superconductivity are explained in the BCS microscopic theory developed by J. Bardeen, L. N. Cooper and J. R. Schrieffer [19] in 1957. Today many superconducting metals and alloys are known, but only a few of them are technologically suitable for superconducting magnet development till date.

1.4.1.1 Low Temperature Superconductors (LTS)

The superconducting materials with critical temperature T_c< 30 K are known as low temperature or BCS superconductors. Two commercially available LTS, NbTi (an alloy of niobium-titanium [20-21]) and Nb_3Sn (an inter-metallic compound of niobium-tin [22-23]), are typical work-horse for magnet applications. Most of the practical SMES systems installed to date are based on NbTi operating at boiling point of liquid helium (4 K). This is mainly because of its ductility that allows conventional coil-winding scheme and low influence of mechanical strain on its current carrying capacity (up to 1% strain there is no appreciable reduction of critical current and with a stress limit of typically ~500 MPa to 600 MPa).

NbTi wire is made of fine filaments embedded in a high purity, highly conducting normal metal known as stabilizer (like Oxygen-Free-High-Conductivity (OFHC) copper or aluminum) to absorb heat and conduct it to the coolant minimizing heat generation during a disturbance. NbTi rod is inserted into a copper can, covered with lid and welded following evacuation. The monofilament billet is then hot extruded. The extruded rod is cold drawn and is shaped in hexagonal form, which is afterwards stacked in a multi-filamentary billet. The multifilament billet is again extruded and drawn down to desired diameter. The typical engineering current density of commercially available superconductors is as shown in Figure 1.5.

A higher field can be reached with the application of inter-metallic compound Nb_3Sn. However, it has some inherent technological problems like brittleness, strain induced degradation in critical current, *etc.* Because of its brittleness, Nb_3Sn must be formed in-situ at its final size and shape before a high temperature heat treatment at ~ 650 ^{0}C, during which the tin reacts with niobium to form the superconducting inter-metallic compound (the wind and react winding). The critical strain limit is usually less than 0.4% with a critical stress limit of 100-200 MPa range depending on the manufacturing process. The current carrying capacity at 4.2 K of Nb_3Sn decreases sharply after 20 T. After a superconducting phase of Nb_3Sn is formed, even a slight bending can cause irreversible degradation of its performance.

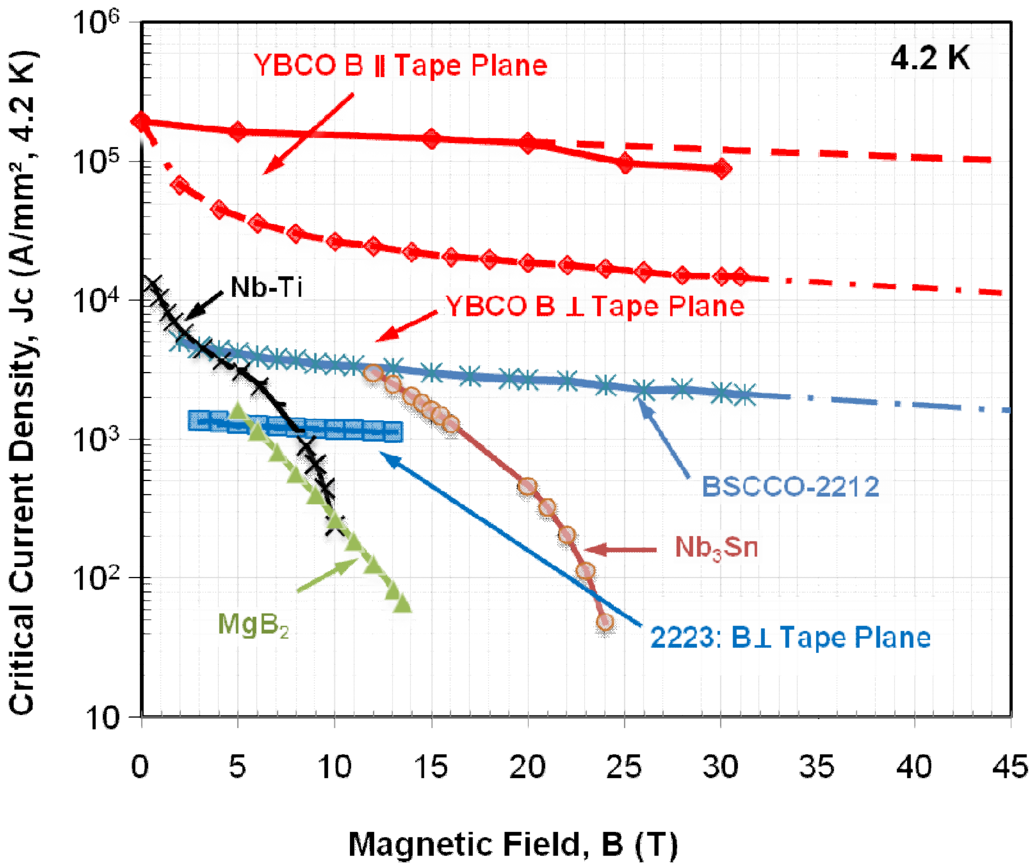

Figure 1.5: Typical critical characteristics (J_C *vs. B*) of available superconductors [24].

1.4.1.2 High Temperature Superconductor (HTS)

Since the discovery of high temperature superconductors in ceramic copper oxides in 1986 [25], efforts have been put to develop tapes and wires for magnet application. In general, superconductors with transition or critical temperature T_c > 30 K are referred as high temperature superconductors or "Non-BCS Superconductors". Two commercially available leading HTS superconductors are bismuth strontium calcium copper oxide (BSCCO-2223 or $(Bi\ Pb)_2Sr_2Ca_2Cu_3O_{10+x}$ and BSCCO-2212 or $(Bi\ Pb)_2Sr_2Ca_1Cu_2O_{8+x}$) based first generation tape [26] and yttrium barium copper oxide (YBCO) based second generation or coated conductor [27-29]. The HTS materials are characterized by higher critical temperature (normally more than the boiling point of liquid nitrogen) and higher critical field (Some cuprates have critical field B_{c2} of more than 100 T). However, cuprate materials are brittle ceramics, expensive to manufacture and is not easily turned into wires or tapes. BSCCO tapes are commercially manufactured mostly by powder-in-tube (PIT) process, where the sintered raw materials (stoichiometrically mixed BSCCO-2223 or BSCCO-2212) are put inside the silver tubes and extruded. A bundle of such tube is formed and again put inside a silver tube and extruded. As high concentration of oxygen atmosphere is crucial to exhibit superconductivity, heat treatment under oxygen rich atmosphere is carried out. The silver matrix is used since it has very high oxygen permeability and stabilizes the superconductor electrically and thermally. The misalignment of crystalline grain boundaries in HTS materials limits the critical current. In order to achieve high critical current, the *c*-axis (perpendicular to the tape surface) of the grains needs to be mostly aligned so that current can easily flow in the ab plane (the plane the tape surface). The c-axis orientation is achieved by rolling and texturing process. BSCCO materials are mechanically weak and therefore, must be laminated with a stronger material such as stainless steel, copper, brass, *etc.* Depending on the laminations, the critical strain that degrades the current density varies approximately from 0.2-0.6% [30]

due to fracture of the filaments. BSCCO composite wire contains about 60-75% of silver resulting manufacturing cost heavily depends on silver. BSCCO wire is not an ideal material since it needs to be refrigerated at 20-30 K to carry high current in high magnetic field.

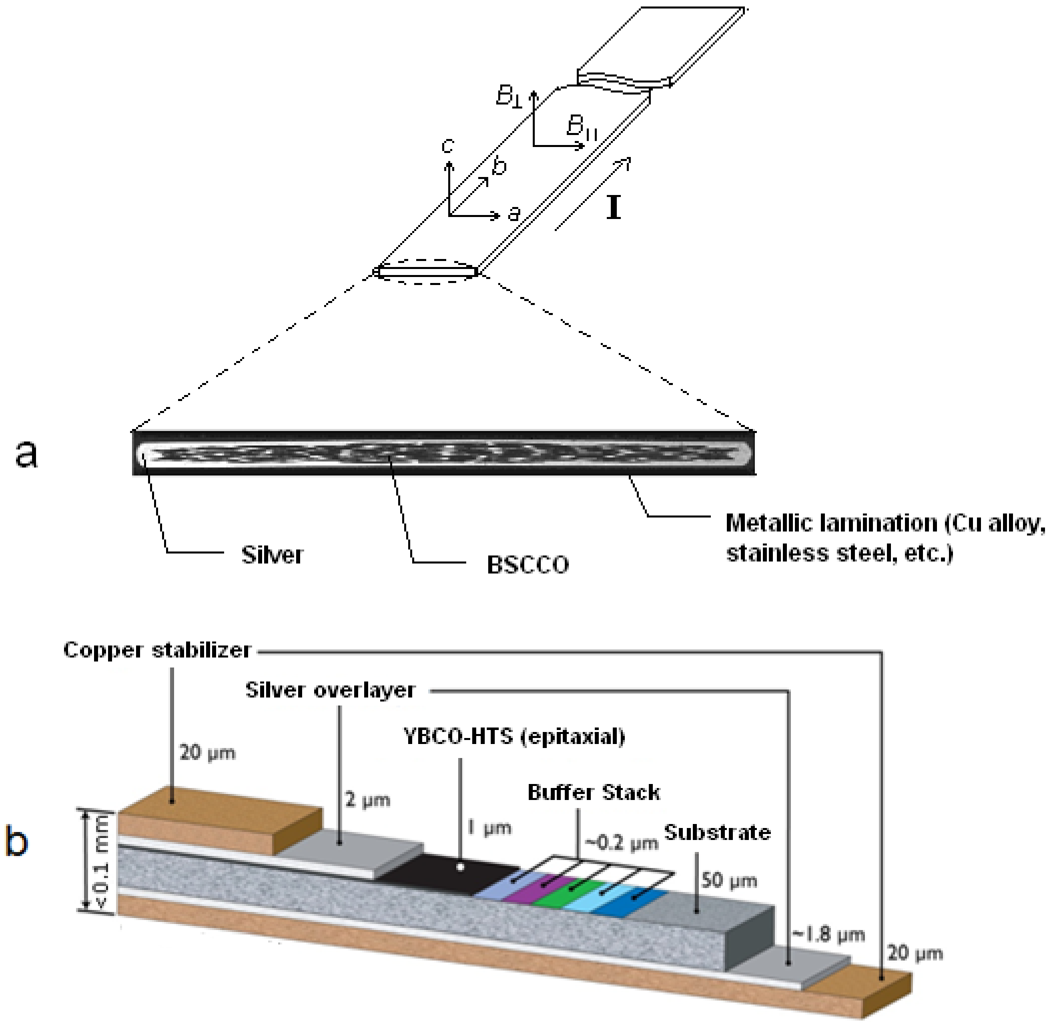

Figure 1.6: a) Cross-section of BSCCO-2223/Ag tape (0.3× 4.5 mm) in silver matrix [29], b) Structure of textured 2G HTS coated conductor [28, 35].

The in-field performance of coated conductor based on YBCO ($YBa_2Cu_3O_7$-x) is much superior to BSCCO and is therefore under commercial development. Moreover, the silver content in 2G HTS wire is almost two orders of magnitude lower than the 1G HTS tape/wire. The coated conductor development involves textured substrate and a thin film deposition of YBCO over it. There are two leading technologies to align grains in YBCO: The Ion Beam Assisted Deposition (IBAD) [31] and the Rolling Assisted Biaxially Textured Substrate (RABITS) [32] technique. Super Power Inc., USA uses IBAD/MOCVD (Metal Organic Chemical Vapour Deposition) [28] whereas; American Superconductor, USA uses RABITS/MOD (Metal Organic Deposition) method [29]. Grain to grain misorientation in a polycrystalline HTS thin film is responsible for reduction in current density. Because of their polycrystalline properties, they do not have symmetric behavior under tension and compression. The scaling up of 2G HTS conductor is still remains a challenge from R&D to manufacturing process while writing this thesis for a continuous long length (over km length). Further, it has been reported [33-34] that delaminating of tapes occurs at high magnetic field when using resin based insulation system in 2G HTS coils.

The cross-sectional view of typical BSCCO-2223/Ag tape and YBCO-123 HTS tape are shown in Figure 1.6. There are many industrial and scientific applications (fault current limiter, magnet current leads, power cable, HTS transformer, *etc.*) where HTS tapes are successfully used. Both 1G and 2G HTS tape have homogeneity problem, i.e., over a long length critical current density J_c is not uniform. Therefore, the minimum J_c over the length determines the operating current density. Further research and development on HTS tape is needed to improve their performance for the development of future SMES system.

The conductor chosen for initial development of prototype SMES system at VEC centre, Kolkata, is cryostable NbTi conductor. Based on our specifications and after significant R&D effort, Luvata, USA, could develop a suitable customerized Rutherford-type NbTi cable for the VECC's 4.5 MJ SMES system.

1.4.2 Cable Configuration

The superconducting cable for magnet development must meet several requirements such as high engineering current density, good mechanical strength, ductility, and low cost. Different cable configurations such as cable-in-conduit conductor (CICC), Rutherford-type conductor, Wire-in-channel conductor, *etc.*, are used depending on the energy and power levels.

The large scale SMES system typically uses CICC with high current carrying capacity, forced flow supercritical operation, and high voltage electric insulation capacity. The CICC as in Figure 1.7 is typically composed of many strands twisted in multiple stages in a rectangular/circular stainless steel conduit. The coolant flows (forced cooling) inside the void area of the conduit to cool the superconducting strands. The requirement of forced flow cooling indeed makes the cryogenic system complicated and also is economically not a good choice for micro and small scale SMES system.

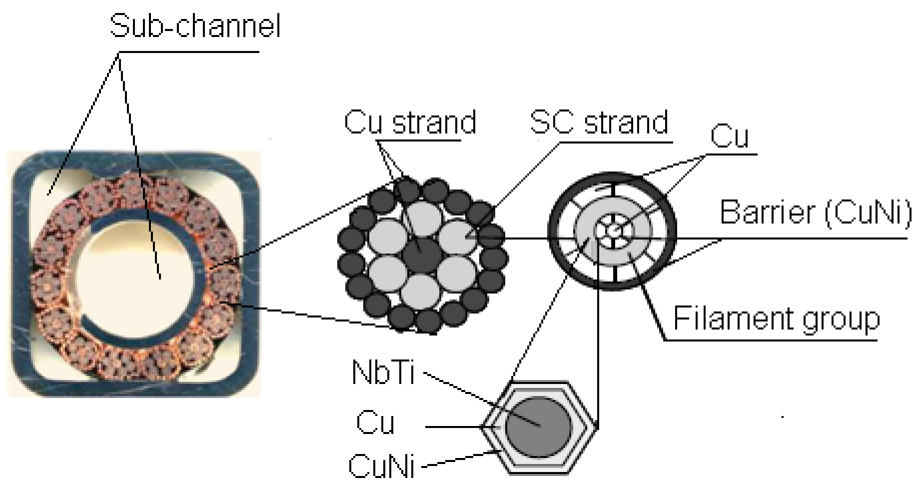

Figure 1.7: Schematic of a typical CICC (Courtesy: Chubu Electric Power Co. Ltd., Japan) with internal helium channel.

The conductor configuration of Wire-in-channel and Rutherford-type cable is shown in Figure 1.8. The wire-in-channel conductors is cryogenically stable and in case of quench-transition transport current flows into the copper matrix and heat-transfer to surrounding coolant is more than the joule heating. This type of conductor is inherently very stable; however, higher copper to superconductor ratio (10:1 or more) contributes eddy current loss during magnetic field transients of SMES operation. The 0.6MJ SMES system in VECC, Kolkata, uses wire-in-channel conductor in pool-boiling liquid helium.

The Rutherford-type of cable consists of two flat layers of strands sloping one layer to the right and other to the left and fully transposed. SMES coil with Rutherford-type cable immersed in pool-boiling helium is preferred for small scale SMES unit desired to mitigate voltage dip application because of its high current carrying capacity or critical current density with relatively low AC loss during magnetic field transients due to transposition of the strands. Further, conventional winding technology is possible with Rutherford cable because of its flexibility.

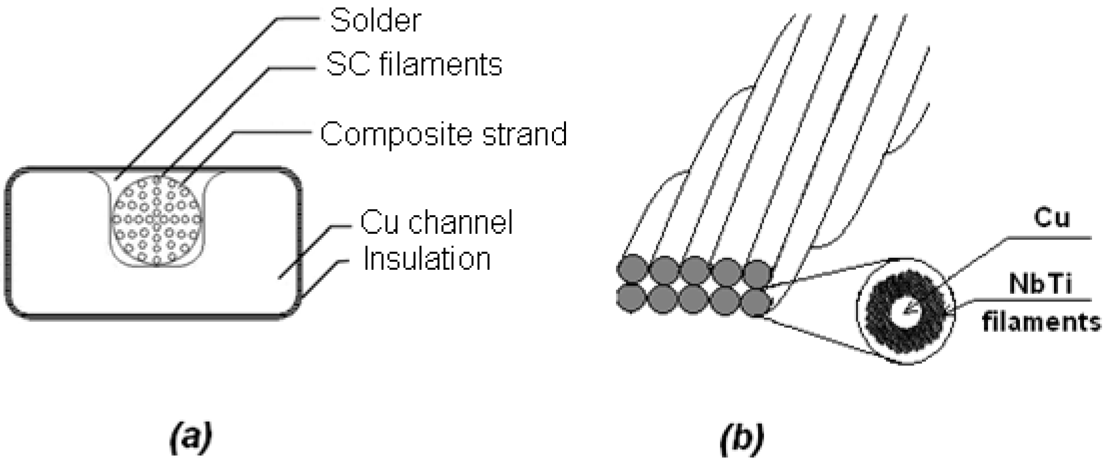

Figure 1.8: Schematic of (a) Wire-in-channel (WIC) conductor, (b) Rutherford-type cable.

For high energy physics accelerator multipole magnet application, Rutherford type cables are widely used and therefore, the manufacturing technology has already been matured. Design of the 4.5 MJ/1MW toroidal SMES coil is studied in the thesis with a suitable custom-made Rutherford type cable.

1.4.3 Stability of Superconductor

Stability refers to the phenomenon of the superconducting magnet system to operate reliably despite the presence of disturbance events. At the operating temperature of LTS superconducting magnet, the heat capacity of materials decreases almost by a factor of three from that at room temperature. At this temperature even a small amount of heat generated due to any instability or disturbances cause local temperature to rise beyond the critical temperature. The disturbances are primarily due to mechanical, electromagnetic, thermal, *etc.*, distributed over a zone of superconducting winding or localized (point disturbance). Therefore, a major requirement of superconducting magnet of transient operation, as in SMES, is its stability margin. Stability of the conductor is described by the proximity of the operating point to the critical surface in (I, B, T) space, where I is transport current, B is magnetic field and T is temperature. Thermal stability of the cable against transient heat-input like a conductor movement, fluctuation in magnetic field, heat in-leaks, *etc.*, are important parameters to be considered in the design of superconducting magnet. Other source of disturbance is flux jump or sudden movement of the pinned vortices due to development of Lorentz force larger than the pinning force and resulting reduction of critical current density. The flux jumping is solved either by reducing the disturbance (adiabatic stability) or conducting away the generated heat (dynamic stability). Both the stability criteria and protection against quench imply the requirement of small filament sizes.

The stability of a magnet is characterized by the minimum propagating zone (MPZ) and minimum quench energy (MQE) [36]. A normal zone larger than MPZ will grow in length and smaller than MPZ will recover. It is required to deposit an amount of energy more than MQE to initiate a quench. The intersection of the magnet load line to the critical surface is the quench point. In a one dimensional adiabatic approximation, neglecting heat transfer to the surroundings, MPZ may be written as:

$$\frac{2kA}{l_{MPZ}}(T_c - T_{op}) = J^2 \rho_m \, A \, l_{MPZ} \tag{1.8a}$$

$$l_{MPZ} = \left(\frac{2k(T_c - T_{op})}{J^2 \rho_m} \right)^{1/2} \tag{1.8b}$$

where, ρ_m is the normal state resistivity of the strand matrix material, J is the current density, T_c is critical temperature, T_{op} is temperature of the coolant and k is the thermal conductivity of the strand dominated by copper matrix, A is the conductor cross-sectional area. Superconducting materials such as NbTi or Nb_3Sn have very poor electrical as well as thermal conductivity beyond critical temperature, and therefore, thermal and electrical conductivity of the matrix material can only be taken in to account while calculating MPZ of the conductor analytically. However, detailed quench analysis considering the heat transfer, *etc.*, provides more realistic value of MPZ. The energy required to develop MPZ of length l_{MPZ} is known as minimum quench energy (MQE). The higher the MQE, more is the conductor stability against any transient disturbance. MQE is calculated as

$$MQE = \int_{T_0}^{T_C} l_{MPZ} \; A \, C(T) \, dT \tag{1.9}$$

where, $C(T)$ is the volumetric specific heat of conductor as a function of temperature.

Stekly et al. [37] defined a stability criteria based on the steady state heat diffusion equation mentioning if the current in the superconducting sample is below the critical current and if the heat generated in the normal zone is less than the heat removed by the heat transfer to the surrounding coolant, then thermal stability is ensured or the conductor is said to be cryostable. The condition of cryostability is defined as

$$\alpha_{st} = \frac{I_c^2 R}{h S (T_c - T_b)} < 1 \tag{1.10}$$

Where, h is the heat transfer coefficient, I_c is the critical current, R is the resistance developed in the normal zone, S is the surface area of the normal zone, α_{st} is known as Stekly parameter. The cryostability indeed allows recovery from operational disturbance in the sense that even if the entire winding becomes resistive it can still return back to superconducting state provided cooling is present.

1.4.4 Mechanical Design

The stress and deformation in the coil depends on stages of fabrication and environment temperature. The pre-tension on the superconducting cable during coil-winding transforms in to tensile and radial stress. Winding tension creates a stress accumulation in the bobbin. During cooling down, due to differential thermal contraction of different materials in the coil and bobbin, the stress developed can exceed the allowable limit. On the contrary, when the coil is energized, the magnetic force $F= J\times B$ (acting per unit volume) acts to relax the stress in the bobbin. If the magnetic force is too large compared to pre-tenson, it may even lead to separation of the innermost layer of the coil from the bobbin, which may cause conductor movement or cacking of impregnation. The associated frictional heating may even lead to quench of the magnet. Therefore, with a proper material and thickness of the bobbin and with an appropriate winding tension, it is possible to have the coil in contact with the bobbin during energization, in other words, the radial stress can be maintained as compressive in nature. In addition, the deformation or strain level in the coil depends on parameters like the stress-strain characteristics, differential thermal contraction among constituent winding materials during cool-down, pre-stress during winding, *etc.* The objectives of the mechanical design are:

i) The equivalent stress of all the constituent materials of the coil and associated structure never exceed the yield stress.

ii) All parts in the coil remain in compression at full excitation.

iii) Always maintain compressive stress between innermost layer of the coil and the outer surface of the bobbin.

Therefore, to design a SMES magnet the overall mechanical stability of the system must be considered.

1.4.5 Magnet Quench and Protection

Quench is an irreversible transition from superconducting to normal state of the magnet. For a variety of reasons, the local temperature in the coil winding may exceed the critical transition temperature of the superconducting strand resulting propagation of normal zone. The origin may be conductor motion under the influence of Lorentz force resulting heating of the cable by release of frictional energy. The other reasons of quench may be due to cracking of epoxy, insufficient cooling, *etc.* Coil must be protected against over-heating during quench and possible destruction of normal conducting part of the coil. It is important to understand the quench behavior of the coil in details while developing a quench protection system.

Reliable detection of quench onset is another important issue. After detection of the quench, the current in the coil must be reduced to a safe level in short period of time, typically within a few seconds or less, depending on the quench protection scheme, stored magnetic energy, winding details, *etc.* Large voltage to the ground may develop during quench and therefore, adequate measure needs to be considered to prevent breakdown of insulation and reduce risk to personnel. Therefore, a reliable quench detection and magnet protection system is one of the most important safety features of the design. Finally, it is important to develop the large scale magnets in such a way that it is inherently stable against quench.

1.4.6 Transient/ AC Loss

In SMES system, the current and magnetic field varies during energy charging and discharging. Despite zero loss in stationary condition, transient field will cause energy dissipation (AC loss) in superconductors. The dissipated loss might degrade the performance of superconductor due to rise in temperature since superconductor does have very poor thermal diffusivity and further, the dissipated loss must be removed by the cryogenic cooling system. The main loss mechanism in filamentary composite superconducting cables exposed to a time-varying magnetic field are hysteretic magnetization losses in superconducting filaments, coupling current losses among filaments and eddy current losses in the normal conducting matrix materials. The magnetic field variation inside the material induces electric field $\vec{E}$ following Faraday's law $\nabla \times \vec{E} = -\dot{\vec{B}}$. The electric field drives the screening current in the material with a critical current density of $\vec{J}_c$ (Bean's model). The screening current dissipates energy at a local power density of $\vec{E}.\vec{J}_c$. However, the hysteretic loss can be reduced by decreasing the dimension of superconductor.

Composite superconductors are made of many thin superconducting filaments embedded in a normal-conducting metal matrix. In the loop formed by the filaments, an induced current develops due to change in magnetic field perpendicular to the plane of the loop. Inside the filament, the current flows without any resistance, however, it encounters resistance only at the ends where it crosses the normal conducting matrix of the composite. The current is called coupling current since it couples the filaments into a large magnetic system. The coupling current can be decreased by twisting the filaments with a small twist pitch and by increasing the resistivity of composite materials, *etc*. Suitable materials like Cu-Ni or Cu-Mn alloy is normally used as matrix material to reduce the coupling loss. The low loss coils are important since typical cooling power of 1 W at 4.2 K demands electrical power of 500 W at room temperature. Further, in adiabatic winding, the AC loss due to magnetic field transients can raise the conductor temperature to its critical value T_c. AC loss in SMES system plays a vital role in system performance and efficiency. During discharging and charging operation of SMES, magnetic field changes causing AC losses in superconducting coil and eddy current losses in the cryostat. These contributions need to be kept to a very low level by a suitable design of the cryostat and a proper choice of superconducting cable. The measured magnetization in two different types of superconductors (cryostable conductor of filament diameter of 40 μm with copper matrix and Rutherford-type cable of filament diameter of 10 μm and Cu-Mn alloy matrix) chosen for the SMES development in VECC is shown in Figure 1.9.

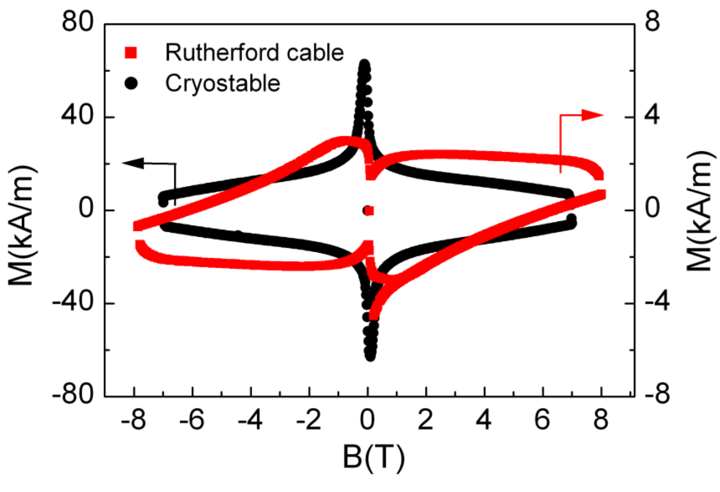

Figure 1.9: Magnetization (M-B) loop for the cryostable wire-in-channel NbTi conductors (Cu to superconductor ratio = 20) and Rutherford-type NbTi cable (Cu to superconductor ratio = 2) measured with SQUID magnetometer.

It is very clear that the Rutherford-type cable does have much less contribution to magnetization or hysteretic loss compared to the cryostable conductor.

1.4.7 Coil Configurations

Depending on the size and application, SMES coil can be constructed in many different configurations. The typical configuration is solenoid or toroid type. With regard to installation of SMES systems, the limit of acceptable stray field is set at 0.5 mT [38], which is approximately the average earth magnetic field. Further, the transient magnetic field might interfere with the operation of other electrical components in the power conditioning system. For small scale SMES system (~kWh-MWh range), different following configurations are proposed.

A solenoid-type SMES is widely used due to its simplicity and cost-effectiveness. Unfortunately, solenoid-type SMES suffers from their stray magnetic field. Passive ferromagnetic shielding may be used around the solenoid to reduce the stray field at outside. The inconvenient magnetic stray field of solenoid SMES configuration can be reduced significantly by adding extra coaxial solenoid coil or active shielding in a way that the current in second coil is directed in opposite to the first coil as shown in Figure 1.10.

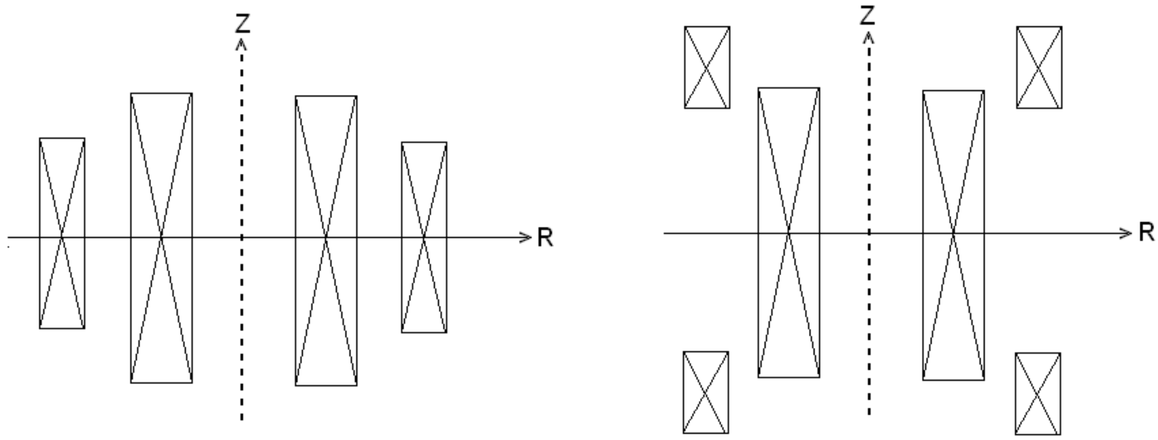

Figure 1.10: Schematic of actively-shielded solenoid configurations.

Suitable optimization scheme could reduce the stray field outside within allowable limits. However, the conductor requirement in this configuration would be as high as two times of that in single solenoid for the same level of stored energy.

The stored energy is expressed as

$$E = \frac{1}{2}L_1 I_1^2 + \frac{1}{2}L_2 I_2^2 - M I_1 I_2 \tag{1.11}$$

Where, L_1 and L_2 are the self inductances of each coil, M is the mutual inductances between the coils, I_1 and I_2 are the current in each coil. Ampere-turns in inner coil are much higher than that of outer coil so that most of the energy is stored in the inner coil. The ratio of outer coil to inner coil radius is very important to determine the effective use of superconducting material. Active shield configuration is quiet attractive since the stray field decreases outside the system as $1/r^7$ w.r.t. $1/r^3$ dependence of a single solenoid coil [39]. However, small deviation of coil size and mismatch of axes due to fabrication error increases the stray field appreciably. Optimal design of actively shielded SMES coils with objective of stored energy and minimal stay field are studied by different groups [40-41].

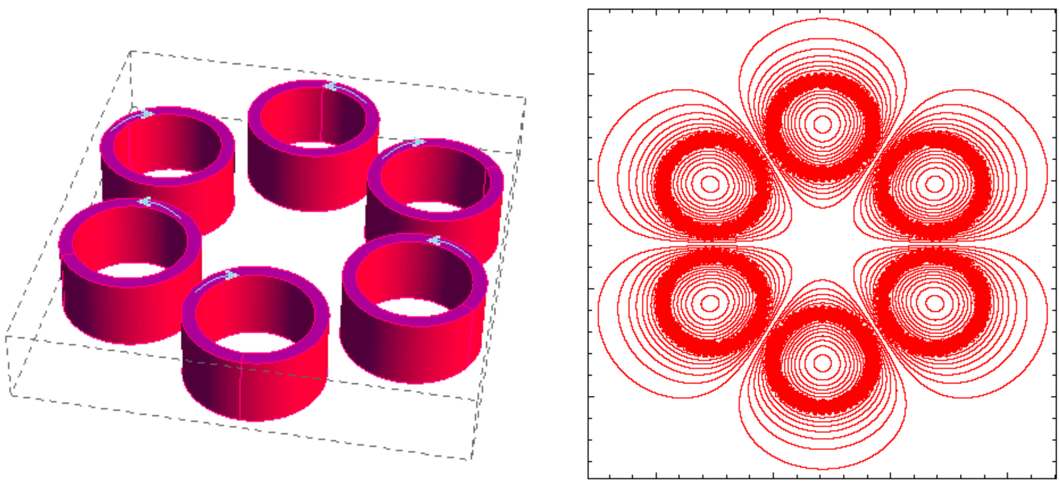

(a) (b)

Figure 1.11: (a) Solenoid coils with anti-parallel momenta configurations, (b) Magnetic lines of forces at coil median plane.

Multipole solenoid configurations with antiparallel moment is another feasible solution to reduce stray magnetic field of a SMES system at outside the coil where even numbers of coils with same size are arranged in alternative magnetic moment directions as shown in Figure 1.11.

The multipole coil configurations are very attractive compared to other coil configurations because of its modularity. Optimal SMES design using four similar solenoids in a configuration of anti-parallel momenta is studied [42] primarily to reduce stray magnetic field. Chubu Electric Power Co. Ltd. [2] in Japan has developed SMES with similar four quadrant configurations. However, it was reported that the conductor requirement increases by 60-80% for a 0.5 MJ SMES system in this configuration w.r.t. single solenoid of same stored energy capacity.

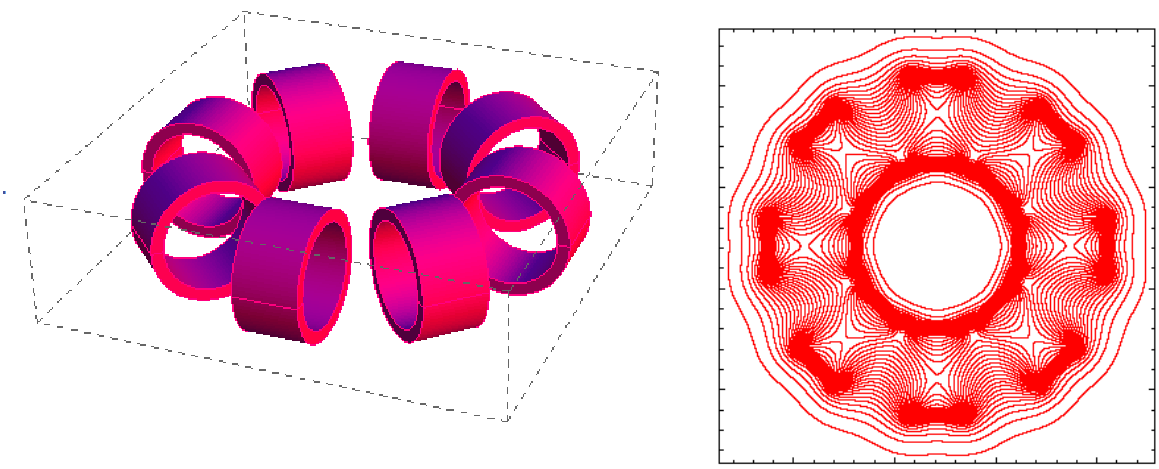

(a) (b)

Figure 1.12: a) Schematic of sector-toroidal configurations, (b) magnetic flux lines at median plane of coil system.

The most efficient way to reduce stray magnetic field at outside the coil assembly is the toroidal configuration. The main advantage of toroidal configurations is that magnetic field is completely contained within the coil and magnetic field leakage can be reduced significantly within a very small distance away from the structure. A perfect toroidal coil does not have any stray magnetic field, but the manufacturing process and maintenance is a major issue. Therefore, a practical coil system must necessarily be made up of a number of discrete coil segments or modules (sector-toroidal) for manufacturing ease and maintenance purpose.

The sector-toroidal coil is composed of several coils (solenoids, racetracks, or D-shaped coil) connected in series and arranged in a toroidal symmetrical form as shown in Figure 1.12. The optimum numbers of solenoid coil module and its sizing are of major design aspect. Further, in sector-toroidal configuration, sector experiences a net inward radial force to be arrested mechanically. Parameter survey of toroidal magnet with double pancake circular module or single solenoid elemental coil using HTS tape has been investigated by different groups for varied range of stored energy capacity [9, 43-46]. However, with regard to reliability of the operation, LTS based system is still probably the preferred choice.

1.4.8 Cooling Selection

For stable operation of the superconducting magnet an efficient cooling of the coil is essential. Various sources of heat input into the cryostat and coil system have to be compensated by the cooling system. A cooling system must be incorporated in such a way that it ensures the cooling down of the magnet system in a reasonable period of time and maintain the operating temperature despite any thermal perturbation that are likely to occur. The cooling principle used is primarily determined by the temperature range of operation, heat load (both dynamic and static), heat exchange, allowed pressure levels and the nature of application. There are primarily three modes of cooling: pool-boiling, forced-flow and conduction cooling method.

1.4.8.1 Pool-boiling mode

In this mode, the superconducting coil is completely immersed in a bath of liquid cryogen in thermal equilibrium with vapour. The heat is removed by evaporating liquid and by convection. Saturated helium-I at atmospheric pressure with a temperature of 4.3 K is normally used for bath cooling. Helium boils at constant temperature defined by the saturated pressure in the bath. At the interface between superconductor and liquid, bubble formation (nucleate boiling) and vapour film (film boiling) may occur depending on amount of heat generation. The steady state heat transfer coefficients are measured by various authors with a sizeable spread in results due to measurement set up, conductor material and its surface condition, inclination, presence of cooling channels, *etc*. However, typical nature of heat transfer coefficient on a heated surface on saturated liquid helium at ambient pressure is shown in Figure 1.13. Following Schmidt [47], a conservative approximation for pool-boiling heat transfer for saturated liquid helium at atmospheric pressure is given by

$$\dot{q}(W/m^2) = 10^4 \times (T_s - T_b)^{2.5} \tag{1.13}$$

Where T_s is the hot surface temperature to be cooled, T_b is the liquid bath temperature.

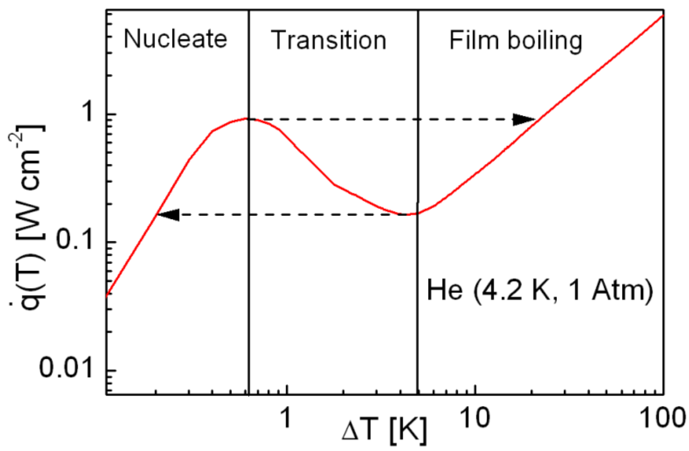

Figure 1.13: Typical heat flux at saturated liquid helium at ambient pressure.

A heat flux of around 3000 W/m^2 may develop for boiling helium at a temperature difference of around 0.5 K between metal surface and liquid helium. Following the correlation of Sydoriak et al. [48], a guide line of critical heat flux, $\dot{q}_{\max}(W/m^2)$ due to the presence of cooling channels in the winding is calculated as

$$\dot{q}_{\max} = \frac{w}{\sqrt{z}}.\frac{h_l \rho_l}{2}\left[\frac{qg}{\chi - 1}.\left(1 - \frac{\ln(1 + f_q(\chi - 1))}{f_q(\chi - 1)}\right)\right]. \tag{1.14}$$

Where, *w (m)* is the coolant gap, h_l *(J/kg)* is the latent heat of boiling liquid, ρ_l *(kg/m^3)* is liquid density, χ is the ratio of liquid to vapour density, g is the earth acceleration (9.81 m/s^2), f_q is the quality factor, considered as 0.35 for short gap length.

For lower operating temperature, one has to pump on the helium bath down to 50 mbar (below lambda point temperature). The superfluid helium in the temperature range of 1.8-2 K is preferred because of both excellent heat transfer from superconductor and improved critical current density at superfluid temperature compared to operating temperature at 4 K. However, operation at sub-atmospheric pressure increases the risk of both dielectric break down due to transient voltage developed in coil and contamination of liquid helium system due to occurrence of leaks. Therefore, for sub-cooled operation at 1.8-2.0K, a pressurized helium system operating at little more than atmospheric pressure is often chosen.

The cooling mode considered for the SMES program in VECC, Kolkata uses pool-boiling liquid helium because of the simplicity of adopting the cryogenic system.

1.4.8.2 Forced-flow mode

The other option for large scale magnet system is to use forced flow liquid helium at a pressure above the critical pressure of 2.26 bar (Supercritical helium). Above critical pressure, supercritical helium behaves like a standard fluid with no bubble formation since saturation line will never be crossed with temperature rise. Heat is absorbed by sensible heat of helium. The superconducting cable requires void or cooling channels for forced-flow cooling. The liquid and vapour phases are indistinguishable in supercritical helium. Forced-flow supercritical helium (as required in CICC conductor) provides excellent heat transfer characteristics with no bubble formation. The forced flow cooling is quiet complex requiring dedicated cryogenic system with helium liquefier, circulating pump, *etc.*

1.4.8.3 Conduction-cooled mode

Conduction cooling with a closed-cycle refrigerator is an excellent option for small superconducting magnet system avoiding complicated networks of piping generally requires for forced flow cooling. In addition, conduction-cooling system is more efficient in terms of energy consumption since storage and transfer loss of cryogenic fluid is alleviated. Conduction-cooling system is most effective for HTS magnet with operating temperature of 20-30K. The refrigeration capacity of the cryocooler at the operating temperature and integration of cryocooler and magnet play an important role on overall performance.

1.5 Optimization Algorithm

Numerical procedures for constrained nonlinear optimization can broadly be grouped into two methods: gradient-based method and direct search method. The gradient-based method such as sequential quadratic programming (SQP), augmented Lagrangian method, and the non-linear interior point method, *etc.* use first derivative (Gradient) or second derivative (Hessian) of objective function. Traditional gradient-based optimization techniques have many limitations such as the difficulty of finding global optimum in presence of local optima and there exists convergence issues as well. The direct search methods are Nelder-Mead, genetic algorithm (GA), differential evolution (DE), and simulated annealing (SA), *etc.* The direct search method converges more slowly, but robust and computationally more expensive. The evolution algorithm structured from the mechanism of natural evolution comprising of selection and reproduction operator in a search space has become very successful and popular to find global optimum for constrained optimization problem mostly due to its very good convergence capability. Differential evolution (DE) algorithm is a population based search method developed originally by Storn and Price [56]. The DE algorithm is used to find the optimal parameters of SMES coils.

Optimization in the superconducting magnet design for energy storage application is a systematic approach with a goal of finding a good balance satisfying the requirements such as minimization of conductor length, transient loss, *etc.* utilizing the available superconducting materials in a manner to reduce capital cost as well as operating cost.

Optimization of conductor requirement for superconducting solenoid-type coil has been studied for past few decades [49-52]. The published articles were dealt mostly with the relationship between geometrical parameters of coil and magnetic field to reduce the conductor volume. Borchi [53] developed a multi-objective optimization technique using fuzzy logic (FL) along with finite element method to optimize the volume of micro-superconducting energy storage system for toroidal type and axisymmetric configuration. Higashikawa [54] used genetic algorithm (GA) along with finite element (FE) to optimize high temperature superconducting (HTS) coil geometry for SMES to minimize AC loss. Aki Korpela et al [55] and several other groups used sequential quadratic programming

(SQP) together with FEM to minimize conductor volume of HTS based SMES coil. The thesis gives an analytical formulation of the optimization problem in terms of coil parameters and aims to minimize either overall conductor requirement or cryogenic refrigeration load including both dynamic and static heat load into the cryostat using differential evolution (DE) algorithm, which in turn reduces the operating cost of the system. Further, Multi-objective optimization approach using DE algorithm is also used to design a sectored-toroidal SMES system using Rutherford-type cable.

Considering the objective function to be minimized as $f(x)$, $x=\{x_1, x_2, x_3, \ldots, x_n\}$ subject to the set of constraints $g_i(x)$, the augmented objective function is written using panalty function approach.

The DE algorithm starts with establishing the initial population. The population size should not be too small in order to avoid local minima or stagnation. Again, larger the size is more will be the computation period. In general, it sufficient to choose initial population size (N_P) = 10 D, where D is the dimension of the problem or number of design variables. The mutation ratio (F), cross-over ratio (C_R) and number of generations are set initially. In each step the DE mutates trial vector by adding weighted random vectors to them. If the cost of trial vector is better than that of target vector, target vector is replaced by trial vector in next generation. During each iteration, a new population (N_P) is generated. The j^{th} new point is generated by picking three random points, x_u, x_v, and x_w from the old population and forming $x_F = x_w + F(x_u - x_v)$. A new point x_{new} is constructed from x_j and x_s by taking i^{th} coordinate from x_s with crossover probability C_R and otherwise taking coordinate from x_j. The crossover probability is also chosen from the optimal range of {0.5, 1}. The augmented objective function corresponding to trial vector is compared with augmented objective function with target vector, i.e. if $f(x_{new}) < f(x_j)$ is satisfied then x_{new} replaces x_j in the next population.

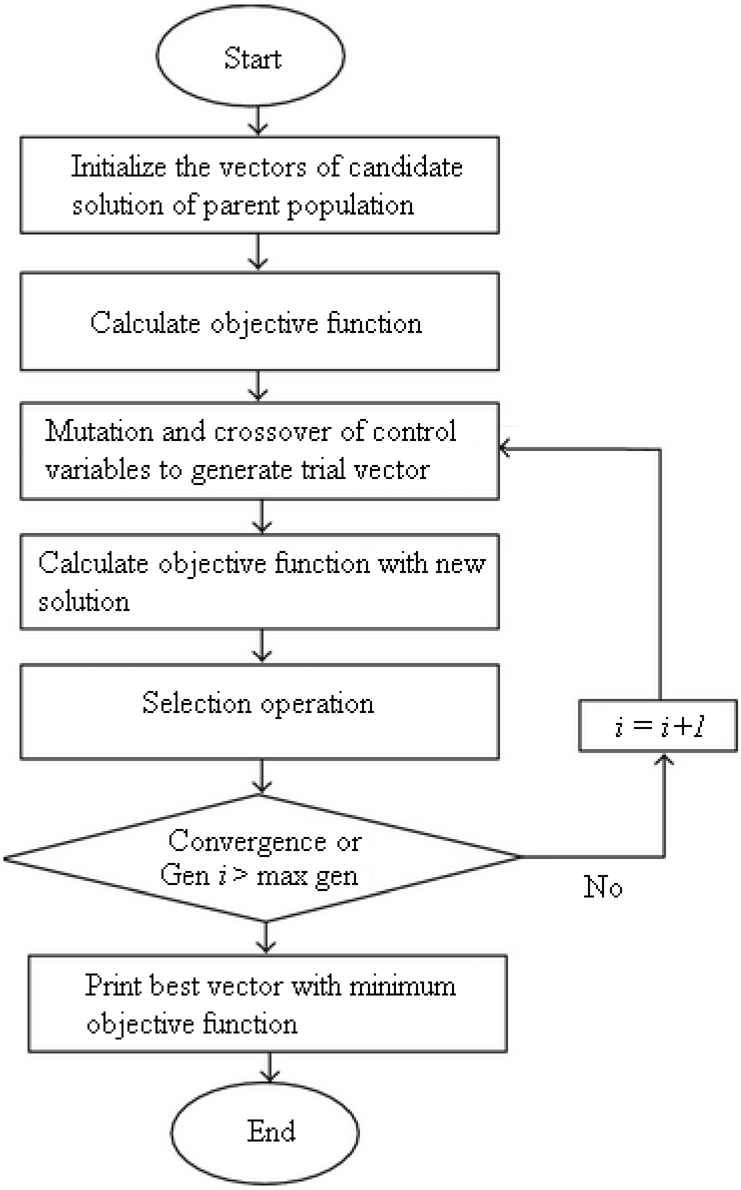

Figure 1.14: Flow chart of differential evolution (DE) optimization algorithm.

This process is continued until termination criteria of a preset maximum number of generation is met or the difference in objective function between two consecutive generations is acceptably small. The basic working algorithm of DE method is highlighted in Figure 1.14.

1.6 Objective of the Thesis

In this thesis, work is pursued to develop optimization approaches for designing the SMES system and to establish the correlation among the geometrical and operating parameters of the same, in context of investment cost and performance reliability. This thesis consists of two parts. The first part describes the superconducting cable characterization, design, development and test results of a 0.6 MJ solenoid-type SMES system integrated with power-conditioning system. The second part describes the design of two different configurations (solenoid-type and sector toroid-type) of SMES system. In this context a novel approach of design optimization has been adopted based on DE algorithm. The design optimization includes the practical aspect such as measured critical characteristics, maximum allowable stress, *etc.* for a desired level of stored energy of SMES coil. State-of-the-art multiobjective Pareto-optimal design is presented for sector-toroidal SMES system considering the practical engineering aspects. Detailed magneto-structual analysis to design a structurally sound coil support system and cryostat for 4.5 MJ sector-toroidal coil assembly has been developed. Finite element modeling using commercial code ANSYS is developed to analyze transient heat load in the liquid helium system as well as in intermediate thermal shields. Based on these studies, the sector toroidal-type design has been chosen for future development.

1.7 Overview of the Thesis

This thesis is organized in the following way:

Chapter 2 describes the details critical characteristics measurements, joint development technology, measurement of yield stress for various component materials, residual resistivity ratio measurement, *etc.*

Chapter 3 introduces generalized design optimization of solenoid-type SMES coil using cryostable conductor. This chapter also addresses other design issues such as quench protection study, design of dump resistor, transient loss evaluation, *etc.*

Chapter 4 describes the development of 0.6 MJ SMES coil and its integration with the power conditioning system. The design results such as quench evolution, AC loss, *etc.* are validated with coil test data. Results of voltage sag mitigation are also highlighted in this chapter.

Chapter 5 describes a generalized design strategy of solenoid type superconducting magnet for energy storage purpose. The design minimizes the transient as well as steady state cryogenic refrigeration loads and provides geometric as well as operating points. Effects of circumferential or hoop stress on coil design parameters are investigated.

Chapter 6 describes a generalized Pareto optimal design of sectored toroidal superconducting coil for energy storage application that minimizes both required length of superconducting cable as well as toroid overall size. The design also investigates the effect of coil stress, AC loss, stray magnetic field outside, *etc.*

Chapter 7 describes detailed magneto-structural and transient analysis of a 4.5 MJ/1MW toroidal SMES system using Finite Element Analysis (FEA) using commercial available codes. This study is very important and mandatory in order to design coil support structure and cryostat as well. Further, detailed quench analysis study is performed to determine the protection system of the coil.

The conclusion of the thesis together with further scope of research is given in Chapter 8.

CHAPTER 2

EVALUATION OF THE SUPERCONDUCTING CABLE

One of the most important parameter that needs to be known while designing a superconducting magnet system is the dependence of critical current of the superconducting cable on the magnetic field at operating temperature. This is because the critical current largely depends on the metallurgical process and microstructures such as distribution of imperfections like grain boundaries, dislocations, precipitates, *etc.*, acting as flux pinners and heat treatment process during fabrication. This chapter presents the experimental measurement and evaluation of superconducting wire used for the magnet optimisation study and development. Two conductors are investigated: Copper embedded niobium-titanium (NbTi) alloy based wire-in-channel type and Rutherford-type NbTi cable.

2.1 Wire-in-Channel Conductor

In wire-in-channel superconductor, the composite of multifilamentary superconductor is first produced with nominal Cu to SC ratio (2:1 in this case) and then soldered into a normal-conductive (Copper or aluminium mostly) channel of suitable dimension thus providing cryostability. Use of aluminium over copper presents several manufacturing difficulties such as compatibility of flux, soldering temperature, *etc.* Therefore, copper or its alloy based channel is normally preferred. Selection of overall copper to superconductor ratio primarily depends on the issues related to stability and mechanical stress considerations. Under normal transition of superconducting wire, the transport current will partially or completely switch to the stabilizer, and return back to the superconductor matrix material after the matrix temperature drops below transition temperature.

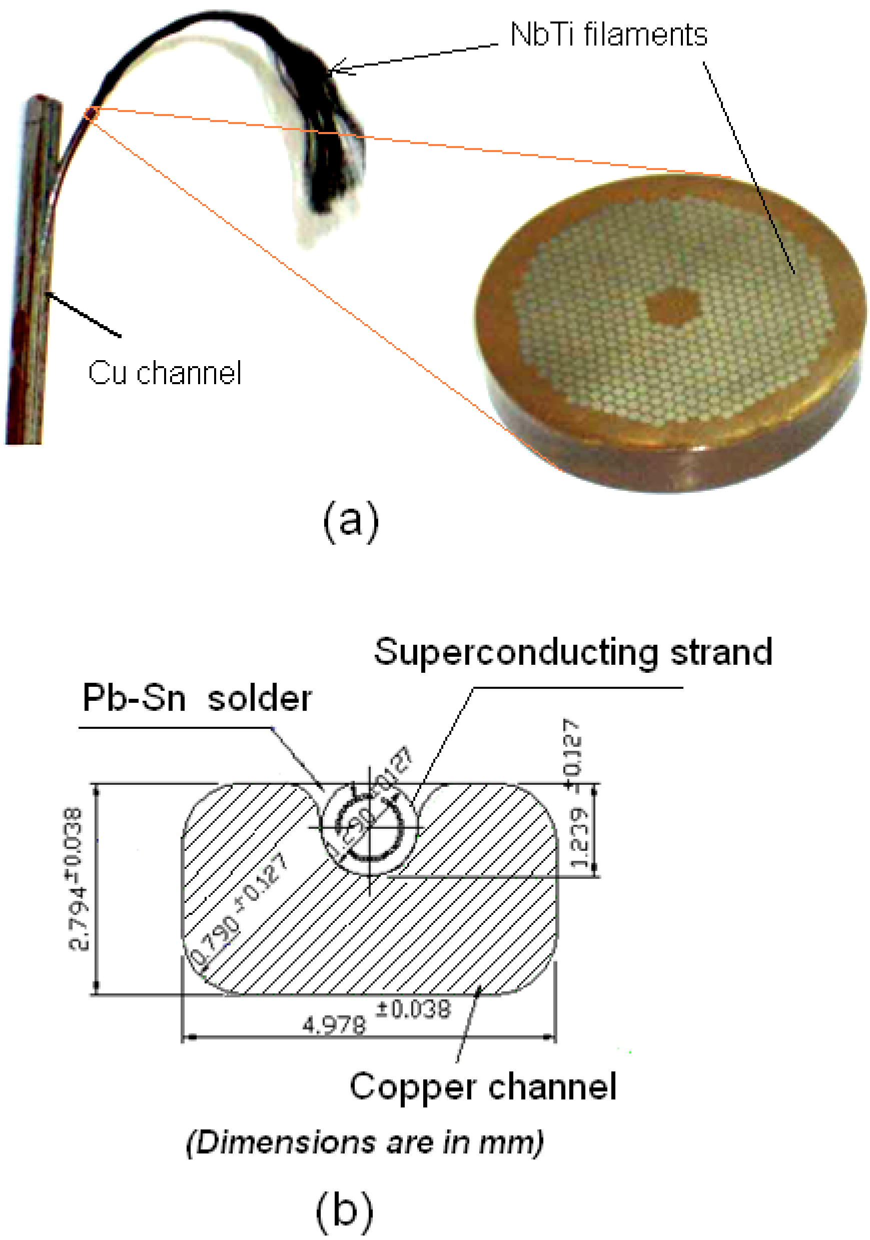

Figure 2.1: Wire-in-channel conductors: (a) Photograph of wire-in-channel conductor, (b) Cross-sectional view of the conductor.

It is very important to provide good electrical and thermal contact between copper stabilizer and superconducting strand, since other wise, the cryostability of the conductor looses locally. The thermal and electrical contact gets affected due to the development of air voids in the process of soft soldering of the superconducting wire into the normal conductive channel. Dimension of flaw or void accepted for a particular superconducting magnet depends on the position of the flaw in winding, local magnetic field level, heat transfer to surrounding coolant, *etc.*

Table 2.1: Specifications of wire-in-channel NbTi conductor

Parameters	**Values**
Conductor dimension (mm)	2.97×4.79
Number of strands	1
Diameter of strand (mm)	1.29
Number of filaments	500
Diameter of filaments (μm)	40
Filament twist pitch (mm)	~12.7
Copper to superconductor ratio	
In strands	1.3:1
Overall	20:1
Critical current I_c (A) at 5 T	1080
RRR (B=0 T)	120

The wire-in-channel conductor (as specified in Table 2.1) considered in this thesis work was developed by Outokumpu Advanced Superconductor, USA (presently Luvata, USA) and is shown in Figure 2.1.

2.1.1 Critical Current Measurement

For the evaluation of the superconducting state, following criteria is adopted [56]: The current level at which longitudinal electric field E_c = 0.1μV/cm or the strand resistivity equals to $\rho_s \sim 10^{-14}$ Ωm is defined as critical current. The conductor test facility has several major components such as a helium cryostat, a vacuum pump station, and superconducting magnet to prive background magnetic field, sample holders, power supplies for the magnet and superconducting samples, instrumentation, data acquisition system, and helium gas recovery system. The critical current measurement has been performed at various background magnetic field levels at the operating temperature of 4.2 K (at liquid helium normal boiling point) by ramping up the current and monitoring the voltage across the voltage taps (four-probe-method) of the short sample. The spiraled sample is wound over a stainless steel former and placed at the center of a solenoid magnet to produce background magnetic field. Current is supplied from a constant current source (1500 A/20V, Danfysik Power Supply, Denmark).The electromagnetic noise due to nearby power supply, *etc.* is arrested using metallic shielding around the sample. The voltage between voltage taps is measured with programmable Keithley make nanovoltmeter (Model 182 & Model 2182) with a sensitivity of 1 nV. The nulling offset is done for every background magnetic field to minimize the offset voltage due to background noise. For each current level, fifty numbers of samples are taken with the trigger interval of 1 second to have an acceptably low standard deviation.

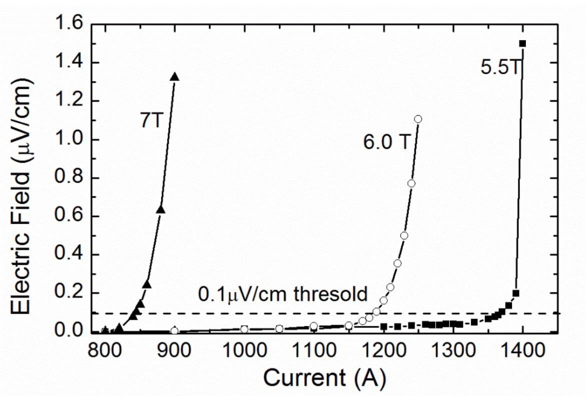

Figure 2.2: V-I characteristics of the wire-in-channel conductors at 4.2 K.

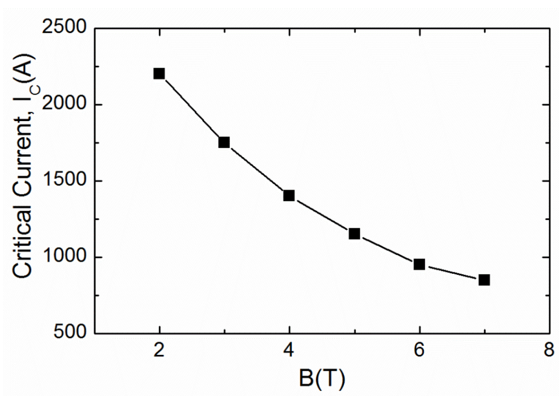

Figure 2.3: Critical characteristics of the wire-in-channel conductor at 4.2 K.

The *V-I* characteristics is studied with different short samples until an irreversible transition or quench occurs with a representative plot as shown in Figure 2.2. For current less than the quench current, the *V-I* curve is reversible. The critical characteristic of the conductor at 4.2 K is shown in Figure 2.3. The transition from superconducting to the normal state of a cable is continuous function provided by a semiemperical law as

$$E = E_c \left(\frac{I}{I_c} \right)^n \tag{2.1}$$

Where, I being the current crossing through the sample, E_c is the critical electric field that defines critical current I_c and n is an integer representing the resistive transition index or quality index of the superconducting wire. The quality index (n) measures the sharpness of superconducting to normal transition when the operating current is very close to the critical current. The n-value is determined through the conductor's voltage-current characteristics (V *vs.* I plot) as

$$n = \frac{\ln(E_2 / E_1)}{\ln(I_2 / I_1)} \tag{2.2}$$

Where E_1=0.1μV/cm and E_2=1.0μV/cm corresponding to current I_1 and I_2 respectively.

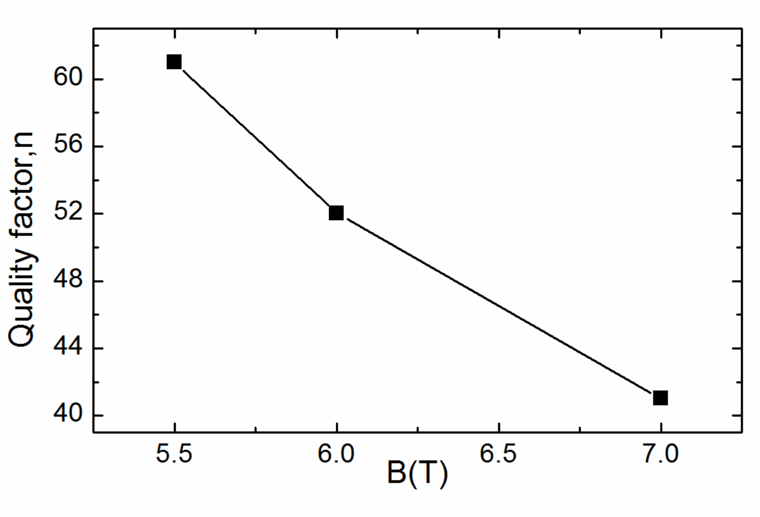

Figure 2.4: Variation of quality factor (n) with magnetic field at 4.2 K.

It is believed that the finiteness of the quality index is caused by the non-uniformity i.e. sausaging effect, in the diameter of the filaments during the extrusion of the superconducting billet. Therefore the quality number is also the index of quality production of superconducting wire in terms of distribution of superconducting filament size after the process of drawing and distortion in filaments developed. The index value is also a strong function of temperature and magnetic field. The quality index at different magnetic fields is as shown in Figure 2.4. Usually low *n*-value is associated with conductor damage due to cabling, whereas large *n*-values are indication of uniform filaments.

2.1.2 RRR Measurement

Evolution of normal zone during transition in a superconductor largely depends on the resistivity of the matrix material, which in turn is a strong function of material residual resistivity. The residual resistivity ratio (RRR) defined as the ratio of resistivity at room temperature over its residual resistivity is an important parameter to be measured prior to understand the quench evolution scenario.

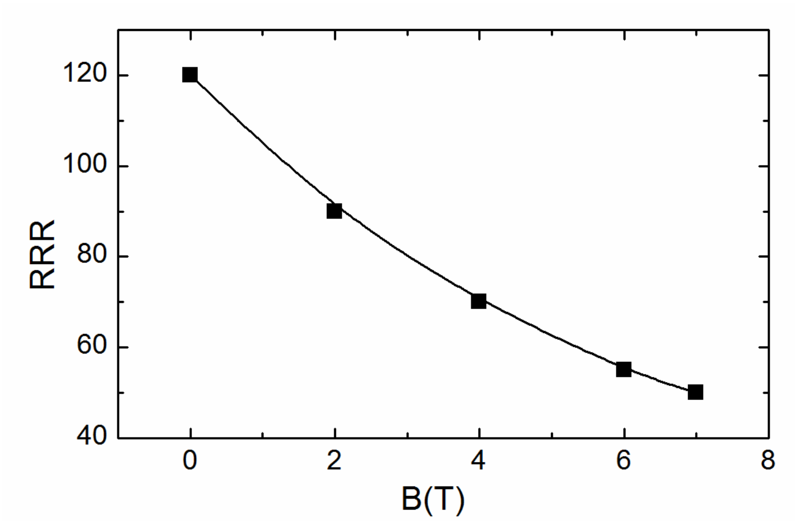

Figure 2.5: Dependence of measured RRR of the copper matrix with magnetic field.

The critical current measurement test set-up is also used to measure wire resistance per meter at room temperature (300K) and just above superconducting transition temperature

(~10K for NbTi). Resistance at 300K is primarily determined by the copper matrix of the wire. For a given dimension of the superconducting cable, it provides a measure of copper to non-copper volume [57]. RRR is a measure of strand copper purity, which is very important with regard to strand thermal stabilization and magnet quench protection. For a given wire, copper to non-copper volumetric ratio is also determined with RRR. The RRR value of the OFE grade copper is measured at different background magnetic fields to find the magneto-resistive effects as shown in Figure 2.5.

2.1.3 Superconducting Joint Development

The superconducting magnet coil might have joints in different location of the coil. If joints are resistive, joule heating occurs raising the temperature of joint. Joint resistance being a continuous disturbance must be made to a reasonably acceptable value. Joint techniques are dealt with highly confidential manner in commercial superconducting magnet. Maximum operating current, heat transfer into available cooling, magnetic field in joint location, *etc.* determines the acceptable value of Joint resistance. Therefore it is required to standardize procedure for superconducting jointing for minimum resistance and sufficient mechanical strength to withstand the tension, during winding of the coil.

Most conventional way of joint is splicing or lap joint. Numbers of lap joints are made in-house on the coil winding machine by brazing copper substrate and soft soldering the superconductor elements of the cable as shown in Figure 2.6. The groove in the brazed joined copper substrate has been enlarged from 1.27 mm to 3.07 mm to provide space between two superconducting elements side by side with an overlapping length. Different lapping length (80-200 mm) is kept between superconductors in the joint and the performance is studied. The average void fraction is kept below 10% (in ultrasonic flaw detector) over the lap length to achieve efficient heat and current transfer from NbTi to NbTi filament as well as NbTi filament to copper stabilizer.

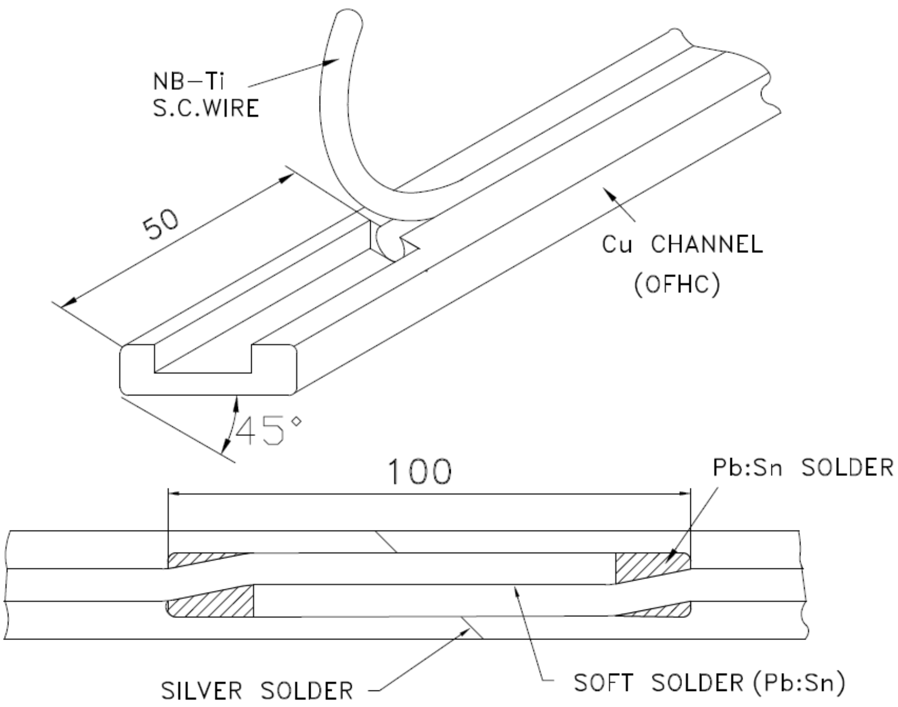

Figure 2.6: Schematic lay-out of developed lap joints with wire-in-channel conductor with Pb: Sn (60/40) solders material.

Superconducting short samples with joint are made and tested up to the background magnetic field of 7 T at 4.2 K as illustrated in Figure 2.7.

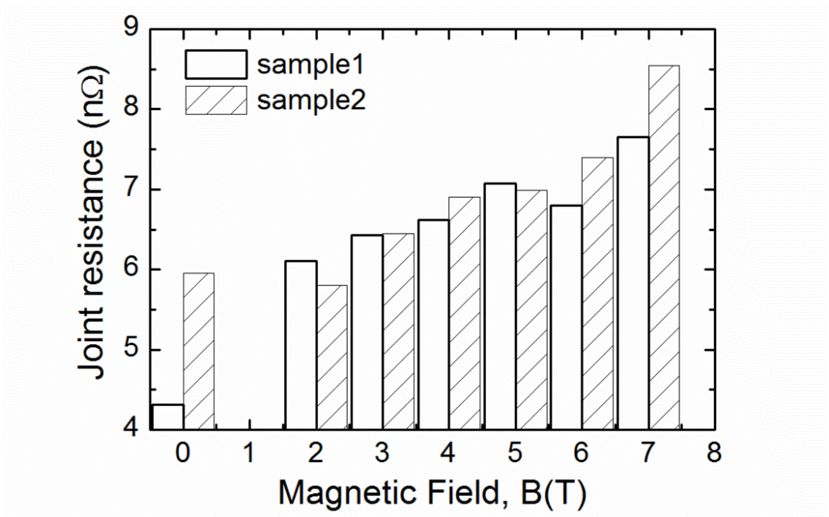

Figure 2.7: Typical joint resistance of developed lap joints at 4.2 K.

It is observed that the joint resistance is within 10 nΩ at maximum field of 7 T after following the 100 mm lap length and a standardised technique of joint for different samples.

2.1.4 Mechanical Properties of Winding and Structural Materials

A superconducting magnet undergoes substantial mechanical stress that limits the performance of the magnet. During fabrication superconducting composite wire is subjected to both bending stress as it is wound in the form of coil and uniaxial stress due to pretension during winding. Further, when the magnet is cooled different materials within the composite materials contracts differently. Finally, magnetic force is developed in the coil during energisation due to interaction of background magnetic field and transport current. Therefore, it is necessary to measure the tensile stress for each of the constituent materials in the winding to determine the allowable tensile as well as von-Mises stress in the winding.

Table 2.2: Mechanical performance of NbTi wire-in-channel conductor, glass epoxy picket fence (G10), SC-SC joint, and mylar tapes.

Specimen	Specifications	Results at Room Temperature
Copper stabilizer with NbTi soldered joint	Gripped at 55 mm away from either side	UTS (MPa): 195 MPa Yield Stress (0.2%): 119 MPa % Elongation: 7.2 %RA: 44.2
Glass-epoxy specimen (G-10)	Thickness: 1.68 mm	UTS: 324 MPa Yield Stress (MPa) (at 0.2%): 170 % Elongation: 4.7
Mylar tape	Width : 2.85 mm Thickness: 0.12 mm Specimen length: 70 mm	UTS (MPa): 120 % Elongation: 107 % % Reduction of area: 49

The stress-strain effect measurement system is composed of a tensile stress machine, a pull rod connecting a specimen holder on which sample is mounted to the servo-hydraulic based universal tensile test machine. The force on the sample is measured with a load cell (strain gauge balanced) on the stationary top crosshead. The bottom crosshead holds the hydraulic actuator which loads the sample. The material deformation is determined by means of a strain gauge extensometer. The initial slope of the stress-strain curve provides the Young Modulus. The slope of stress-strain plot gradually decreases with increasing tensile load and finally become minima at a strain value.

The ultimate tensile strength (UTS) is defined as the stress at which the final slope is reached. Table 2.2 shows the details of the test sample used. The ultimate tensile strength (UTS) measured for various winding materials are shown in Figure 2.8.

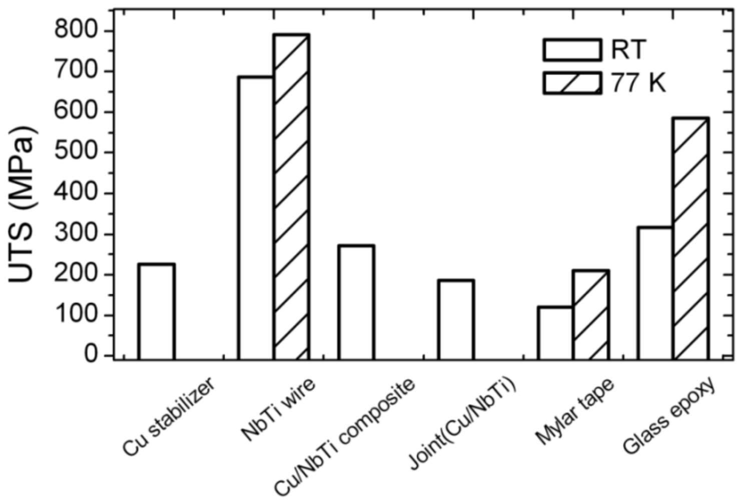

Figure 2.8: UTS of wire-in-channel cable, its components, superconducting joints, mylar tape, NEMA G10 glass epoxy picket fence, *etc.*

2.2 Rutherford-type NbTi Cable

Rutherford-type cable is mostly preferred because of its very low AC loss and large engineering current density. The Rutherford type NbTi cable composing of several strands is suitable for energy storage magnet especially with cryo-refrigerator based SMES system since the transient or AC loss could be minimized during its various modes of operation. A custom-made Rutherford type multi-strand cable (as specified in Table 2.3) is developed and supplied by Luvata Inc., USA. The strands are twisted and compressed into a flat two layer cable. The stability of the conductor is increased by coating of silver tin alloy (Staybrite). The optical microscopic photograph of the cable strands is shown in Figure 2.9.

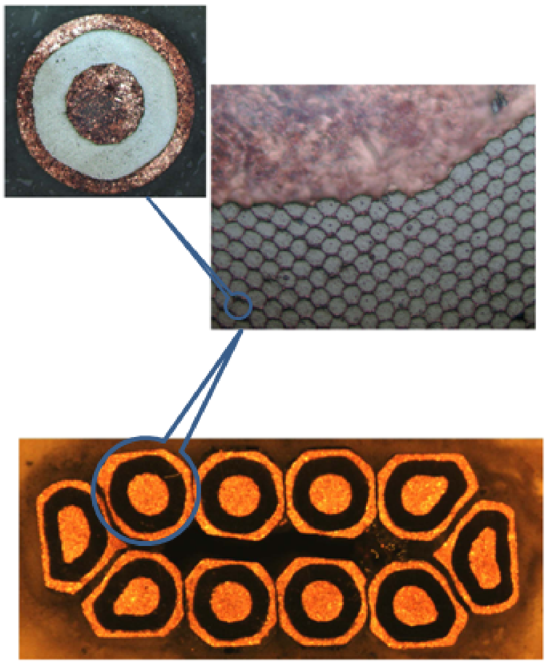

Figure 2.9: Optical microscopy of custom-make Rutherford-type NbTi cable for SMES development in VECC, Kolkata showing the filaments (3900 filaments in each strand) and strands (Courtesy: H. Kanithi, Luvata Inc., USA).

The cable is wrapped with polyimide (Kapton) film of 25 μm thickness with 50% overlap to provide inter-turn insulation.The degradation in critical current due to cabling procedure is determined by measuring cable samples at operating temperature of 4.2 K in at various background magnetic field.

Table 2.3: Specification of NbTi based Rutherford-type cable

Parameters	Values
Cable cross-section (mm^2)	1.29 × 3.67
Number of strands	10
Diameter of strand (mm)	0.72
Number of filaments	3900
Diameter of filaments (μm)	6.7
Filament twist pitch (mm)	~15
Approximate cable lay pitch (mm)	50
Copper to superconductor ratio	
In strands	2.0:1
Critical current I_C (A) at 5 T, 4.2 K	~4000
RRR (B=0 T)	80

2.2.1 Critical Current Measurement

Similar to the measurement for wire-in-channel conductor, four-probe-method is used to measure the critical behaviour of the Rutherford-type NbTi cable. Samples from different spools are taken and critical behaviour is studied for various magnetic fields. At different background magnetic fields, the representative critical characteristic of the cable at 4.2 K is shown in Figure 2.10. For the purpose of optimisation study, the minimum critical current among the samples at a given magnetic field is considered as shown in Figure 2.11. The quality index is found to be around 40 (minimum among the samples) at 7 T as shown in Figure 2.12 and improves at lower magnetic field as expected.

Further, the critical current measurement on individual strand is also performed at 4.2 K up to the magnetic field level of 7 T. It is found that the critical current of the strand is more than 220 A at 7 T conforming the critical current obtained to the measurement of the cable as a whole.

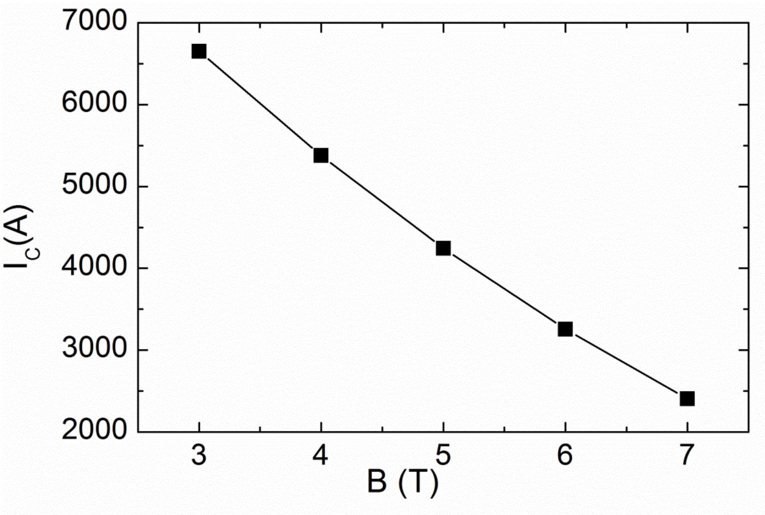

Figure 2.10: Critical behaviour (*Ic-B*) of Rutherford-type NbTi cable at 4.2 K.

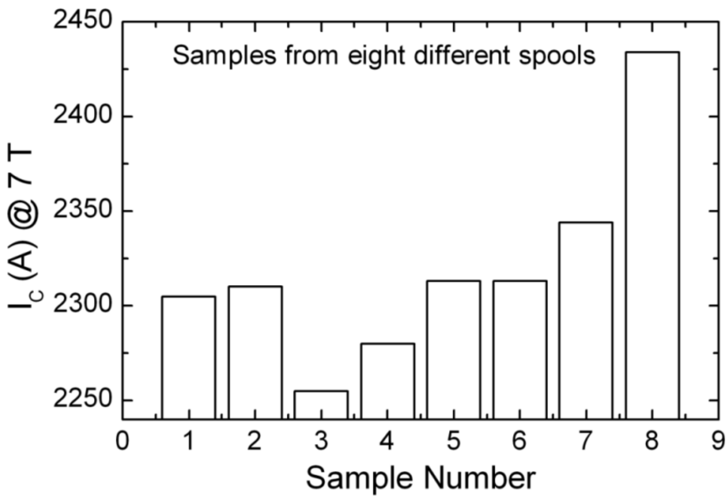

Figure 2.11: Critical current for various Rutherford-type NbTi sample cables at 7 T, 4.2 K.

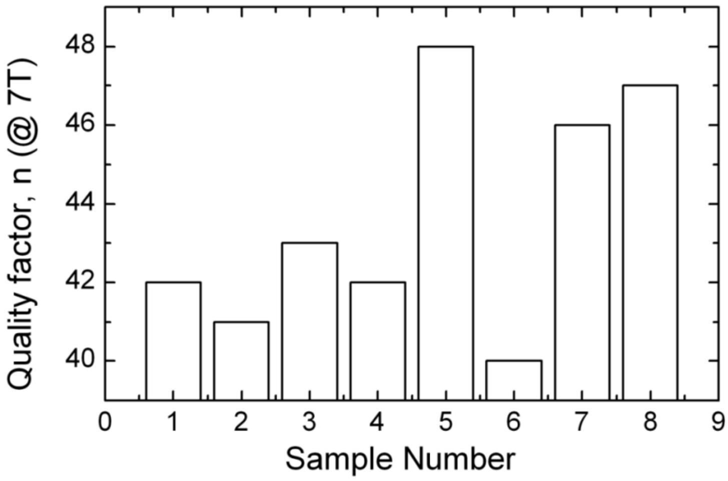

Figure 2.12: Quality index (n) of Rutherford-type NbTi samples from different spools at 7 T, 4.2 K.

2.2.2 Mechanical Strength of Rutherford-type NbTi cable

It is necessary to measure the yield strength, tensile strength, *etc.* of the superconducting cable prior to the design of a superconducting magnet in order to determine the allowable overall stress in the windings. To understand the mechanical property of NbTi Rutherford type conductor, the stress strain measurements are performed on straight samples without any previous strain history. The standard flat type Rutherford-type cable is found be inadequate to directly grip on the Instron machine holder since it leads to stress concentration at the gripping position leading to premature rupture while increasing the strain. The gripping positions of the samples are suitably determined (around one inch length each on both sides) and brazing materials are put over the gripping length so that during sufficient gripping no weak point occurs at the gripping zone. The strain is applied typically at a rate of 0.1% per minute. Stress-strain characteristic is observed with the INSTRON machine at room temperature for different samples and the yield point value at the strain value of 0.1% and 0.2% is as shown in Figure 2.13. It is observed that yield stress corresponding to 0.1% strain is more than 400 MPa at room temperature. The allowable stress for ductile materials may be considered as one-third of yield stress value (at 0.2% strain) at room temperature. Further, the mechanical properties improve at lower operating temperatures.

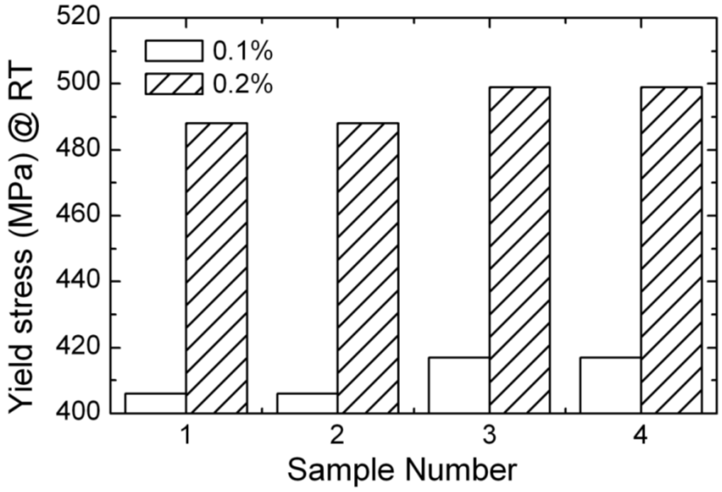

Figure 2.13: Yield stress (YS) of Rutherford-type NbTi samples from different spools at room temperature.

2.3 Conclusions

The superconducting wire or cable used for magnet developments is extensively characterized both electrically and mechanically. The critical characteristics at the operating temperature at various background magnetic fields are studied and are further used for the optimisation study described in the following chapters of the thesis. The maximum allowable stress level in the winding is derived from the measured yield stress and tensile stress of the cable and other materials used for the windings. The index quality (n) is important to study the quench protection scenario of the magnet system. Suitable on-line joint development during winding is very crucial for the reliable performance of the magnet system.

CHAPTER 3

DESIGN OF SOLENOID-TYPE SMES WITH WIRE-IN-CHANNEL CONDUCTOR

Optimization of conductor requirement for solenoid-type SMES coil has been studied for past few decades [59-62]. The published works were mostly dealing with the relationship between geometrical parameters of coil and magnetic field to reduce the conductor volume. However, optimization formulation of solenoid type coil that minimizes the conductor volume for a given stored energy capacity with various practical engineering constraints such as peak mechanical stress on the coil winding for a given stored energy, critical current margin to avoid any quench-like scenario, *etc.* is developed in this chapter.

3.1 Stored Energy and its Dependence

We consider solenoid type coil with basic dimensions as are shown in Figure 3.1. The geometry of a solenoid is defined by its inside radius (a), shape factor $\alpha = b/a$ and $\beta = l/a$, where 2 l is solenoid length and b the outside radius.

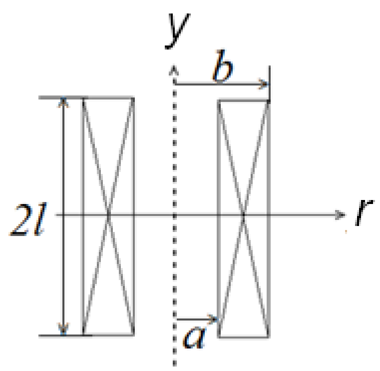

Figure 3.1: Cross-section of solenoid coil.

The center magnetic field B_0 and peak magnetic field B_m on winding for a thick solenoid coil of finite length may be written as

$$B_0(\alpha,\beta,a) = \mu_0 aJ(B_m)K_0(\alpha,\beta) \tag{3.1}$$

$$B_m(\alpha,\beta,a) = \mu_0 aJ(B_m)K_m(\alpha,\beta) \tag{3.2}$$

Where, $\mu_0 = 4\pi \times 10^{-7}$ H/m is the magnetic permeability in free space, $J(B_m)$ is the operating current density of the coil.

For a thick solenoid coil, peak or maximum field exists at the innermost layer at coil mid-plane ($y=0$). The parameter $K_m(\alpha,\beta)$ is expressed in a Legendre polynomial series expansion [62] as

$$K_m(\alpha,\beta) = K_0(\alpha,\beta) - \frac{1}{2}K_2(\alpha,\beta) + \frac{3}{8}K_4(\alpha,\beta) - \frac{5}{16}K_6(\alpha,\beta) + ... \tag{3.3}$$

The polynomial terms K_0, K_2, K_4, and K_6 are dimensionless form factors expressed as

$$K_0(\alpha,\beta) = \beta \ln \frac{\alpha + (\alpha^2+\beta^2)^{1/2}}{1+(1+\beta^2)^{1/2}} \tag{3.4a}$$

$$K_2(\alpha,\beta) = \frac{1}{2\beta}(c_1^{3/2} - c_3^{3/2}) \tag{3.4b}$$

$$K_4(\alpha,\beta) = \frac{1}{24\beta^3}[c_1^{3/2}(2+3c_2+15c_2^2) - c_3^{3/2}(2+3c_4+15c_4^2)] \tag{3.4c}$$

$$K_6(\alpha,\beta) = \frac{1}{240\beta^5}[c_1^{3/2}(8+12c_2+15c_2^2-70c_2^3+315c_2^4) - c_3^{3/2}(8+12c_4+15c_4^2-70c_4^3+315c_4^4)] \tag{3.4d}$$

where,

$$\left.\begin{array}{l} c_1 = \dfrac{1}{1+\beta^2}; \quad c_2 = \dfrac{\beta^2}{1+\beta^2}; \\ c_3 = \dfrac{\alpha^2}{\alpha^2+\beta^2}; \; c_4 = \dfrac{\beta^2}{\alpha^2+\beta^2}; \end{array}\right\} \tag{3.5}$$

The inductance (L_{SMES}) of the air core thick solenoid coil of finite length is given by

$$L_{SMES}(\alpha,\beta,a) = a\,N^2\,\theta(\alpha,\beta) \tag{3.6}$$

Where, $N\ (\alpha,\ \beta,\ a)$ is the total number of turns of the solenoid. Knowing the conductor dimension, N may be determined in terms of coil parameters as

$$N(\alpha,\beta,a) = n_r(\alpha,a).n_y(\beta,a) \tag{3.7a}$$

Where $n_r\ (\alpha,\ a)$ and $n_y\ (\beta,\ a)$ are radial layers and number of turns per layers respectively expressed in terms of conductor dimension and coil parameters as

$$\begin{aligned} n_r(\alpha,a) &= \frac{a(\alpha-1)}{\Delta x} \\ n_y(\beta,a) &= \frac{2\beta a}{\Delta y} \end{aligned} \tag{3.7b}$$

Where, Δx and Δy are the effective breadth and width of the conductor with insulation. The geometry dependent factor $\theta(\alpha,\beta)$ in equation (3.6) is given by [52]

$$\theta(\alpha,\beta) = \frac{\mu_0\pi}{8\beta}\,\frac{(\alpha+1)^2}{1+0.9\dfrac{\alpha+1}{4\beta}+0.64\dfrac{\alpha-1}{\alpha+1}+0.84\dfrac{\alpha-1}{2\beta}} \tag{3.8}$$

The energy stored in a solenoid-type SMES coil is expressed as,

$$E_S(\alpha,\beta,a) = \frac{1}{2}L_{SMES}I^2 = \frac{2\,a^3\ B_m(\alpha,\beta,a)^2\,\beta^2(\alpha-1)^2\,\theta(\alpha,\beta)}{K_0(\alpha,\beta)^2\,x(\alpha,\beta,a)^2} \tag{3.9}$$

Peak field to center magnetic field ratio is defined as, $x(\alpha,\beta,a) = \dfrac{B_m(\alpha,\beta,a)}{B_0(\alpha,\beta,a)}$ (3.10)

The winding volume is written as,

$$V(\alpha,\beta,a) = 2\pi a^3\beta(\alpha^2-1) \tag{3.11}$$

3.2 Operating Current Density

The coil is immersed in a pool of liquid helium at 4.2K. The operating current of superconducting coil depends upon the critical characteristics of the superconducting cable, which is a strong function of peak magnetic field (B_m) inside winding and operating temperature. Considering the space or filling factor (λ) of the coil, the safety margin factor (ζ) over critical characteristics of the superconducting cable (i.e. J_C *vs B*), operating current density (*J*) of coil is determined in terms of coil peak field (B_m) as follows:

$$J(B_m) = J_C(B_m)\lambda(1-\zeta) \tag{3.12}$$

Safety margin factor ζ needs to be considered carefully depending on critical current degradation, minimum quench energy (MQE) of the cable, cooling and winding details, operating temperature margin, *etc.* In the present study, we vary the degradation factor from 5 % to higher values following the quench protection analysis. The safety margin factor ensures that the coil will not quench in normal operation. The winding packing fraction (λ) depends on winding details such as insulation thickness, inter-turn spacers, *etc.* Over the available type of conductor, wire-in-channel conductor has been chosen since it guarantees cryogenically stable operation in liquid helium bath cooling mode of operation. For the present study, glass epoxy spacer (picket fence) of thickness 1 mm is considered to put for inter-turn insulation as well as for easy passage of liquid helium through narrow channels. The winding space factor (λ) is calculated for the present winding scheme to be 0.73. However, depending on the winding scheme, insulation, *etc.*, space factor needs to be determined appropriately. In order to relate the coil parameters with operating current density (*J*), *J* is fitted with peak magnetic field B_m in the following form as,

$$J(\alpha,\beta,a) = \frac{p}{q + \dfrac{B_m}{J(B_m)}} \tag{3.13a}$$

Here, *p* and *q* are the parameters fitted from *J* vs. B_m/J plot. Substituting from equation (3.2), operating current density can be expressed as,

$$J(B_m) = J(\alpha,\beta,a) = \frac{p}{q + \mu_0 a K_m(\alpha,\beta)} \tag{3.13b}$$

The NbTi alloy based cryostable conductor as specified in Table 2.1 has measured critical characteristics as shown in Figure 3.2 and operating current density J at 4.2 K varies with B_m/J as shown in Figure 3.3. Considering the winding scheme, packing fraction and stability margin, *etc.*, the fitted parameters for this particular cable are found as, p =9.00784 T and $q = 4.7483\times10^{-8}$ Tm^2/A.

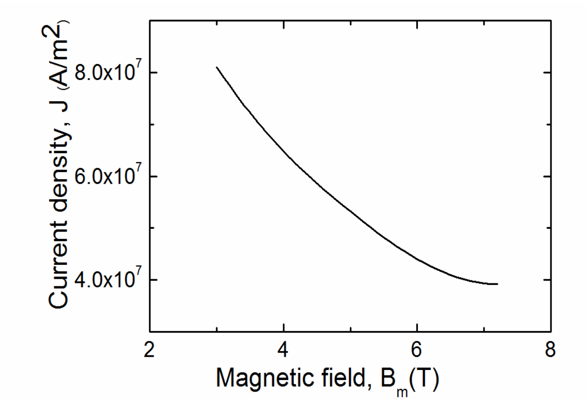

Figure 3.2: Variation of operating current density (J) with magnetic field (B_m)at 4.2 K.

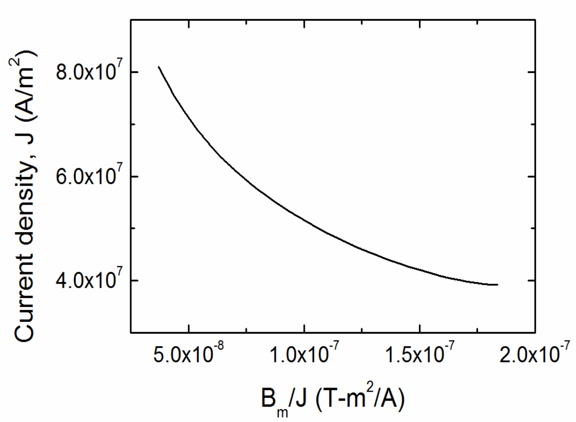

Figure 3.3: Variation of operating current density (J) vs. B_m/J at 4.2 K.

3.3 Electromagnetic Stress Consideration

It is well known that internal electromagnetic force develops within the winding of a magnet coil due to currents flowing in the magnetic field of the coil. These forces must be taken into account in the design of a superconducting coil. In fact, the magnetostructural stress developed due to electromagnetic force could be a limiting factor in the design of high field superconducting magnet. The dominant stress pattern among others is hoop stress due to circumferential tension. The maximum stress in the winding occurs in the inner layer of coil median plane [63]. Under the assumption of negligible shear stress and axial stress developed due to the radial magnetic field is considerably lower compared to overall stress developed, maximum hoop stress may be calculated analytically considering isotropic elastic properties. The variation of axial magnetic field inside the winding may be approximated as a linear fall-off as

$$B(r) = \frac{(\alpha - r/a)B(a) + (r/a - 1)B(b)}{\alpha - 1} \tag{3.14}$$

Considering the local displacement (u) in the radial direction in a small elemental winding as shown in Figure 3.4, Y as Young's modulus, υ as the Poisson's ratio, equilibrium between radial stress (σ_r), hoop stress (σ_θ) and body force ($B\ J\ r$) provides the following differential equation [64]:

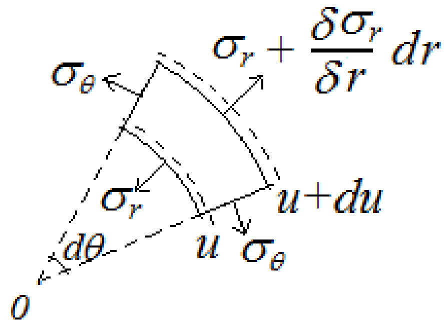

Figure 3.4: Stress components in an axisymmetric winding at coil median plane.

$$\frac{1}{r}\frac{d}{dr}\left(r\frac{du}{dr}\right) - \frac{u}{r^2} = -\frac{(1-\upsilon^2)}{Y}BJ \tag{3.15}$$

The circumferential and radial stress are expressed as

$$\sigma_\theta = \frac{Y}{1-\upsilon^2}\left(\frac{u}{r} + \upsilon\frac{du}{dr}\right) \tag{3.16}$$

$$\sigma_r = \frac{Y}{1-\upsilon^2}\left(\frac{du}{dr} + \upsilon\frac{u}{r}\right) \tag{3.17}$$

Similarly, the circumferential and radial strains are expressed as

$$\varepsilon_\theta = \frac{u}{r} = \frac{1}{Y}(\sigma_\theta - \upsilon\sigma_r) \tag{3.18}$$

$$\varepsilon_r = \frac{du}{dr} = \frac{\sigma_\theta - \sigma_r}{r} \tag{3.19}$$

Writing the following substitution

$$
\begin{aligned}
&r = \xi\, a \\
&b = \alpha\, a \\
&w = u\,Y / [a\,(1-\upsilon^2)] \\
&B\,J\,a = K_1 - M_1\xi \\
&K_1 = (\alpha B_a - B_b) Ja / (\alpha - 1) \\
&M_1 = (B_a - B_b) Ja / (\alpha - 1)
\end{aligned}
$$

Eq. (3.4) is simplified as

$$\frac{1}{\xi}\frac{d}{d\xi}\left(\xi\frac{dw}{d\xi}\right) - \frac{w}{\xi^2} = -K + M\xi \tag{3.20}$$

The solution of Eq. (3.9) is

$$w = C\xi + \frac{D}{\xi} - \frac{K\xi^2}{3} + \frac{M\xi^2}{8} \tag{3.21}$$

The coefficients C and D are determined from the boundary conditions $\sigma_r(r=a) = \sigma_r(r=b) = 0$. Using the Poisson's ratio (υ) of $1/3$, following expression of circumferential stress may be obtained

$$\sigma_\theta(\alpha,\beta,a) = \frac{J(\alpha,\beta,a)\,a}{\alpha-1}\left[\begin{array}{l} \dfrac{7(\alpha\,B(a) - B(b))}{9(\alpha+1)}\left(\alpha^2 + \alpha + 1 + \dfrac{\alpha^2}{\xi^2} - \dfrac{5}{7}\xi(\alpha+1)\right) \\ -\dfrac{5}{12}\big(B(a) - B(b)\big)\left(\alpha^2 + 1 + \dfrac{\alpha^2}{\xi^2} - \dfrac{3}{5}\xi^2\right) \end{array}\right] \tag{3.22}$$

The maximum hoop stress developed at the median plane of inner layer of winding (i.e. *r = a* & *z = 0)* of an isotropic solenoid-type winding expressed as,

$$\sigma_{\theta m}(\alpha,\beta,a) = \frac{2J(\alpha,\beta,a)\,a}{\alpha-1}. \left\{\frac{7(\alpha\,B_m(\alpha,\beta,a) - B_b(\alpha,\beta,a))}{9(\alpha+1)}.(\alpha^2 + \frac{\alpha}{7} + \frac{1}{7}) - \frac{5}{12}(B_m(\alpha,\beta,a) - B_b(\alpha,\beta,a)(\alpha^2 + \frac{1}{5})\right\} \tag{3.23}$$

Axial magnetic field at outer radius (b) of a long finite size solenoid in its median plane ($z=0$) is approximated [65] as

$$B_b(\alpha,\beta,a) \cong -\frac{B_0(\alpha,\beta,a)}{2\beta^2}\left(1-\frac{3}{2}\left(\frac{\alpha}{\beta}\right)^2-\frac{3}{4\beta^2}\right) \quad (3.24)$$

Further, one must consider the pre-stress during winding, thermal cool-down stress, *etc.* depending on winding scheme and cooling details. Winding pretension or pre-stress part may be determined in later stage after getting the initial optimization results to ensure that radial stress is compressive during excitation at 4 K.

3.4 Peak Voltage across Coil during Discharge Mode of Operation

During supply of constant power (P_0) by SMES coil to the critical load, energy stored in SMES coil at any instant of time *(t)* is

$$E(\alpha,\beta,a,t) = E_S(\alpha,\beta,a) - P_0 t \quad (3.25)$$

In designing a SMES coil of a given power rating, it is extremely important that the voltage developed across the coil is kept within safe value so that no dielectric breakdown, damage in insulation, *etc.* occurs. Initial voltage developed across the coil at time instant $t = 0$ of discharge is written as,

$$V_i(\alpha,\beta,a) = \left.\frac{P_0}{J(\alpha,\beta,a)A_C}\right|_{t=0} \quad (3.26)$$

where, A_C is conductor cross-section. Considering the carry over or discharhing period as t_s and the depth of discharge as η, the fraction of stored energy discharged from the SMES coil, maximum voltage developed towards the end of discharge period in constant power output (P_0) mode of operation is expressed as,

$$V_m(\alpha,\beta,a) = \frac{V_i(\alpha,\beta,a)}{\sqrt{1-\eta\frac{P_0 t_s}{E}}} \quad (3.27)$$

Here, η is the depth of discharge of SMES coil that defines the fraction of stored energy delivered to the load to maintain constant power P_0 over the discharge period of t_s. For the present design, we consider η to be 0.7, i.e. 70% of the stored energy can be utilized during discharge operation. Depending upon insulation scheme of conductor, cooling modes *etc.*, maximum allowed discharge voltage, V_m is fixed to a safe value for a given stored energy E, maximum power rating of P_o and discharge period of t_s.

3.5 Objective Function and Optimisation

Minimum length of superconducting material of a particular winding scheme and critical current characteristics for a given stored energy of SMES coil needs to be found out. The length of superconducting material $L(\alpha,\beta,a) = 2\pi\,\beta\,a^3(\alpha^2-1)/(\Delta x \times \Delta y)$ is set as the objective function. The optimization problem can be stated as follows:

$$\text{Minimize } f(X) = L(\alpha,\beta,a) \tag{3.28}$$

Subject to constraints:

$$\begin{pmatrix} g_1(\alpha,\beta,a) = E_S(\alpha,\beta,a) - E_i = 0 \\ g_2(\alpha,\beta,a) = P(\alpha,\beta,a) - P_0 = 0 \\ g_3(\alpha,\beta,a) = \sigma_\theta(\alpha,\beta,a) - \sigma_m \le 0 \\ g_4(\alpha,\beta,a) = V_m(\alpha,\beta,a) - V_a = 0 \\ \alpha > 1.01 \\ \beta > 0.01 \\ a > 0.01 \end{pmatrix} \tag{3.29}$$

Where, $X = [x_1, x_2, \ldots\ldots\ldots, x_n]$ being a decision vector consisting of n design variables. Here, E_i, P_0, σ_a and V_a are required stored energy, power rating, the allowable hoop stress in winding and allowable voltage across terminals respectively. We have intentionally used equality constraints for maximum allowed voltage across the coil since it will be connected in reality across a capacitor bank known as DC link of maximum rated voltage.

Constraint on design variables (*α, β, a)* are adopted with a lower and upper bound to have a feasible solution space of design variables. This is a multivariable nonlinear constrained global optimisation problem. In order to solve the problem successfully a simple and efficient global optimisation method i.e. the Differential Evolution (DE) method is employed.

Since DE is an evolutionary computation, it executes a direct search which utilizes N_p real valued parameter vectors x_i^G, $\{i=1, 2,\ldots, N_p\}$ as a population for each generation G. The initial population is chosen randomly with uniform distribution in search space. Here, N_p is the number of design variables. DE has three operators: mutation, crossover and selection. For each target vector x_i^G, a new mutant vector v_i^G is generated by adding the weighted difference between two vectors to a third vector in the current population, i.e. $v_i^{G+1} = x_{r1}^G + F(x_{r3}^G - x_{r2}^G); r_1 \neq r_2 \neq r_3 \neq i$. Here, the indices $r_1, r_2, r_3 \in \{1,2,\ldots\ldots, N_p\}$. Here, F is a real number to control the amplification of the difference called mutation parameter. The mutated vector's parameters are then mixed with the parameters of another predetermined vector, or the target vector to create the so-called trial vector. This parameter mixing operation is called "crossover". The target vector is mixed with mutated vector during crossover as

$$u_{ij}^{G+1} = \begin{cases} v_{ij}^{G+1}, Random(j) \leq C_R \ \ or \ \ j = Random(n(i)) \\ x_{ij}^{G}, Random(j) > C_R \ \ and \ \ j \neq Random(n(i)) \end{cases} \tag{3.30}$$

Here, C_R is the crossover probability determined by the user. For the purpose of present optimization C_R=0.5 is considered and found to be acceptable for fast convergence of the optimization solution. However, value of C_R other than 0.5 may also be chosen providing same optimal solution, but number of iterations for convergence may be different. If the trial vector yields a better fitness function value than the target vector, the trial vector replaces the target vectors in the following generation. This last operation is called “selection”. The selection scheme is as follows.

$$x_{ij}^{G+1} = \begin{cases} u_i^{G+1}, \ f(u_i^{G+1}) < f(x_i^G) \\ \\ x_i^G, \ f(u_i^{G+1}) \geq f(x_i^G) \end{cases} \tag{3.31}$$

In the successive iterations, if the objective function converges within less than 0.1%, the program terminates and the corresponding design variables are obtained. In most of the cases, convergence of this nonlinear problem is observed with the number of iterations of around 3500 or less. The design parameters obtained [66] for a 0.6 MJ SMES coil are summarised in Table 3.1.

Table 3.1: Design parameters of 0.6MJ SMES coil with cryostable NbTi conductor

Parameters	Values
Coil type	Solenoid
Operating current (A)	800
Operating temperature (K)	4.2-4.4
Inductance (H)	1.87
Stored energy (MJ)	0.6
Peak coil field (T)	6.6
Coil inner diameter (mm)	132.5
Coil outer diameter (mm)	416
Height (mm)	790
Number of winding layers	36
Number of turns/layer	154
Cable length (km)	~5.0
Number of splice joints	2

The critical current margin is kept at around 30% that corresponds to a temperature margin (T_{cs}-T_{op}) of 0.7 K for coil operating at maximum field of around 7 T. The temperature margin has been kept considering different operational scenarios such as flexibility of operating temperature from 4.2 to 4.4 K and any other small disturbances that might occur in the coil during operation.

3.6 Stress Distribution across the Winding Layers

After determining the initial optimized coil parameters considering the peak hoop stress at coil median plane (described in section 3.1.3), it is very important to find the winding tension such that the radial stress during excitation at the operating temperature is compressive or negative. Further, thickness of coil former needs to be determined from stress consideration.

The stress produced in the coil due to pre-stress, differential thermal contraction and magneto-mechanical force during excitation is complex in nature and considers composite elastic modulus in radial and azimuthal direction. In fact, the winding scheme and cooling mode of operation largely determines the stress distribution across the winding. For isotropic solenoid, numerous analytical approximations were suggested with much of them is based on the consideration of plane problem [67-72]. Analytical study of stress distribution for anisotropic winding is mostly restricted to the midplane of the solenoid.

The superconducting coil is considered to be pool-boiled mode of cooling with inter-layer spacing with fibreglass reinforced plastic G-10 for cooling channels. A mylar tape insulation is used at top and bottom surface of conductor to provide insulation between turns. The stress distribution in presence of cooling channels and insulation material at coil midplane is calculated from appropriate filling factor and equivalent elastic moduli in radial and circumferential direction of the winding. The equivalent elastic moduli (Y) in radial and tangential directions are obtained as

$$\frac{1}{Y_r}=\frac{1-\lambda_r}{Y_i}+\frac{\lambda_r}{Y_s\lambda_z+Y_i(1-\lambda_z)}$$

$$Y_t=Y_s\lambda_r\lambda_z+Y_i(1-\lambda_r\lambda_z) \tag{3.32}$$

Where, subscript *i* and *s* represents insulation and superconductor respectively. λ_r and λ_z are the filling factors in radial and axial direction respectively.

3.6.1 Stress due to Winding under Pretension

The stress develops in the coil former and winding while different layers are wound. When layers are wound under pretension (σ_{t0}), a differential pressure develops in the preceding layer. Considering the following boundary conditions, J Kokavec and L Cesnak [72] derived the expression of radial and circumferential stress in successive layers as follows. It is assumed that

i) Radial stress (σ_r) is zero at the internal radius of coil former.

ii) On the external radius of coil former and internal radius of winding the radial stress and tangential stress are equal.

iii) Pressure on the external radius of the coil is given in terms of relative radius of the cylinder, $\rho = r/r_i$ by

$$d\sigma_{re}=-\sigma_{to}\frac{d\rho}{\rho} \tag{3.33}$$

Considering the above boundary conditions, the radial and azimuthal stresses are found without excitation by the basic differential equation for σ_r as

$$r^2\frac{\partial^2\sigma_r}{\partial r^2}+3r\frac{\partial\sigma_r}{\partial r}-\sigma_r(\kappa^2-1)=0 \tag{3.34}$$

The expression of radial and azimuthal or circumferential stress are found [72] as

$$\sigma_{rw} = \sigma_{to} \frac{1}{\rho_w}(s\rho_w^k - \rho_w^{-k}) \int_{\rho_w}^{\alpha_w} \frac{d\rho}{\rho^{-k} - s\rho^k}$$

$$\sigma_{tw} = k\sigma_{to} \frac{1}{\rho_w}(s\rho_w^k + \rho_w^{-k}) \int_{\rho_w}^{\alpha_w} \frac{d\rho}{\rho^{-k} - s\rho^k} + \sigma_{to} \tag{3.35}$$

Where, $k_1 = Y_f/Y_t$, $\kappa = (Y_c/Y_r)^2$ and the auxiliary constant (s) is given by

$$s = \frac{(\alpha_f^2 + 1)(\alpha_f^2 - 1)^{-1} + (k_1\upsilon - \upsilon + k_1\kappa)}{(\alpha_f^2 + 1)(\alpha_f^2 - 1)^{-1} + (k_1\upsilon - \upsilon - k_1\kappa)} \tag{3.36}$$

Therefore, the stresses and deformations due to winding tension are computed as the summation of the results due to each preloaded layer.

3.6.2 Stress during Cooldown

The stress develops when the coil is cooled down to operating temperature at 4.2K due to unequal thermal contraction of different winding materials. Stresses developed in the coil stainless steel (SS-316L) former, winding layers may be evaluated considering the pressure developed by successive winding layers on each other and by winding to the coil former. Refer to J. Kokavec and L Cesnak [72], the pressure developed at junction of winding and coil former is given by

$$\sigma_{fw} = \frac{(\varepsilon_c - \varepsilon_f)Y_f}{(\alpha_f^2 + 1)(\alpha_f^2 - 1)^{-1} - \upsilon - k_1\kappa\left[(\alpha_w^{k_1} + \alpha_w^{-k_1})(\alpha_w^{-k_1} - \alpha_w^{k_1})^{-1} - \upsilon k_1\right]} \tag{3.37}$$

Where, ε_c and ε_f are thermal strain of coil former and winding respectively.

Following the design specification as in Table 3.1, a winding pretension of 13.6 MPa is chosen such that radial stress becomes compressive (negative) under all possible scenario as shown in Figure 3.5. The corresponding tensile or circumferential stress is shown in Figure 3.6.

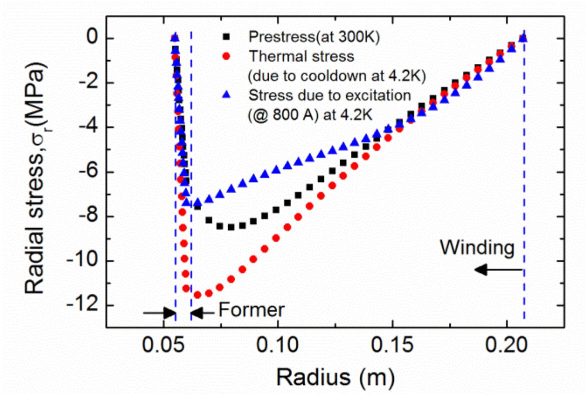

Figure 3.5: Radial stress distribution at the coil median plane.

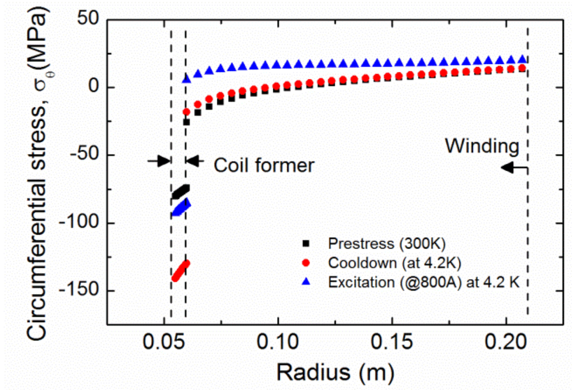

Figure 3.6: Circumferential stress distribution at the coil median plane.

3.7 Stray Magnetic Field Consideration

Since SMES system should be located near a demand site or in a substation, stray field of SMES might restrict its location of site. Stray magnetic field in a solenoid may be remarkably reduced by various methods such as active shielding by adding a second concentric solenoid to suppress the far field which generates a magnetic field in opposite direction of the main SMES coil, multiple concentric solenoids with current in opposition to the main SMES coil, passive shielding with a ferromagnetic shield outside the cryostat assembly, *etc.* as described in ch.1 of the thesis. A simple solution of using passive shielding with ferromagnetic material is considered for the 0.6 MJ SMES coil. The ferromagnetic shielding around the coil cryostat does not influence to the superconducting losses appreciably and the advantages of solenoid geometry are preserved. Stray field in presence of ferromagnetic shielding is simulated with finite element analysis (FEA) using commercial code ANSYS [73]. It is to be mentioned, however, that stray field reduction of a solenoid using ferromagnetic shielding reveals only weak dependence of the solenoid design. Various possibilities of ferromagnetic shielding are studied and reasonably acceptable solution is obtained with the constraints of the experimental hall, ease of operation, *etc.* as shown in Figure 3.7.

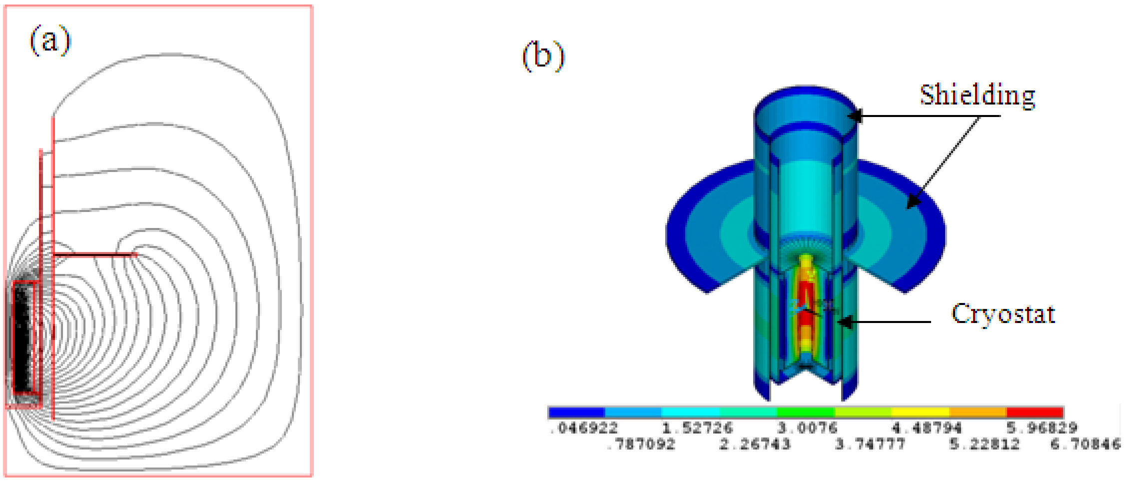

Figure 3.7: Shielding arrangement of 0.6 MJ SMES coil: (a) Magnetic flux with shielding; (b) Magnetic field (in T) with shielding arrangement.

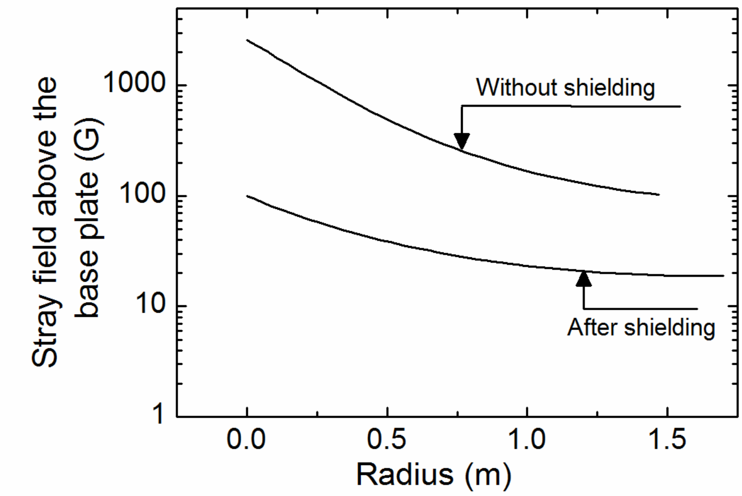

Figure 3.8: Stray field reduction after ferromagnetic shielding.

The stray field at a distance of 1.5 m away from the magnet axis reduces to around 20 G or less as shown in Figure 3.8 and is accepted for the present purpose of prototype developments. However, further reduction of stray magnetic field may be obtained to less than 5 G provided the space constraints on shielding do not have. Although eddy losses are developed in the shield during rapid charge and discharge of SMES, it does not have any contribution to the cryogenic load. The shielding arrangements needs to be structurally fixed against the magnetic force developed on the shield material since the coil cryostat and shield are in radially unstable equilibrium.

3.8 Quench Stability and Protection Study

In spite of taking safety margin in the design stage, there is every possibility that the coil will experience unexpected quench-like occurrence due to many reasons such as heat generation is larger than the minimum quench energy in a poorly cooled region. In the case of quench, stored energy of the magnet can cause a high temperature rise in the region where quench started originally, high voltage between the coil terminals, *etc.* Over the past few decades various approaches to model the quench propagation in superconducting magnets have been proposed [74-77]. The protection system controls the DC contactor that direct the current to the magnet coil through switch S1. Switch S2 controls the switching of the shunt contactor. During transient testing with power converter circuit, the Insulated Gate Bipolar Transistor (IGBT) Switch with its control algorithm is used as protection circuit as shown in Figure 3.9. Combination of S1 and S2 initiates the isolation of power supply and energy dump through dump resistor.

Quench Detection Circuit (QDC) is developed based on the differential resistive voltage across center tap of coil with the provision to adjust threshold voltage and validation time. Vapor-cooled current leads are also protected in other two channels of QDC comparing the voltage drop across each lead with the preset threshold voltage and validation period. The coil temperature measured with CERNOX sensor and operational failure of any IGBT in the DC-DC chopper is also used as redundant quench detection signal.

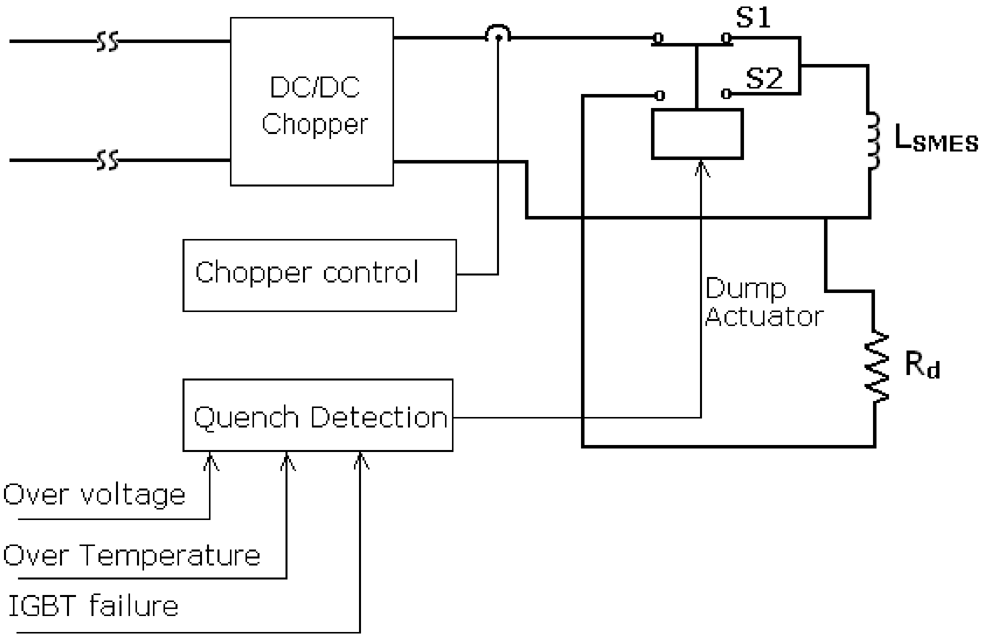

Figure 3.9: Quench protection scheme of the 0.6 MJ SMES coil in VECC, Kolkata.

The coil of 0.6 MJ SMES unit is designed to be cryostable in a pool boiling liquid helium bath at around 4.2 to 4.4 K. Quench behaviour of the magnet and quench protection issues as considered in Figure 3.9 are the focus of this investigation. The quench scenario is studied with one-dimensional heat diffusion equation and current decay equation as

$$C(T)A\frac{\partial T(x,t)}{\partial t}=\frac{\partial}{\partial x}\left(k(T)A\frac{\partial T}{\partial x}\right)+I(T)^2\rho(B,T)+q(x,t)-h(T)(T(x,t)-T_b) \qquad (3.39a)$$

$$L_{SMES}\frac{dI(t)}{dt}+I(t)\left(R_d+r(t)\right)=0 \qquad (3.39b)$$

Where L_{SMES} is the inductance of the coil, R_d is the dump resistance, *r(t)* is the normal zone resistance, *C(T)* is the volumetrically averaged specific heat of conductor, *t* is the time, *k(T)* the volumetrically averaged thermal conductivity, *A* the cross-sectional area, *h(T)* the heat transfer coefficient between conductor and liquid helium, *q(x,t)* the external perturbing heat pulse and T_b is the liquid helium bath temperature, and $\rho(B,T)$ the local average electrical resistivity represented as

$$\rho(T,B)=\begin{cases} 0 & ,T \le T_{cs} \\ \rho_{cu}(T,B).\dfrac{1}{r_{cu}}.\dfrac{T-T_{cs}}{T_c-T_{cs}}, & T_{cs}<T\le T_c \\ \rho_{cu}(T,B).\dfrac{1}{r_{cu}}, & T\le T_{cs} \end{cases} \tag{3.40}$$

Where, r_{cu} is the fraction of copper matrix in the unit cell cross-section of conductor, T_{cs} the local current sharing temperature, T_c the local critical temperature that depends on local temperature and magnetic field calculated by the following equations-

$$T_c(B)=9.2\left(1-\frac{B}{14.5}\right)^{0.59} \tag{3.41a}$$

$$\frac{T_{cs}(I,B)-4.2}{T_c(B)-4.2}=\frac{I-I_c(B,4.2)}{0-I_c(B,4.2)} \tag{3.41b}$$

Determination of heat transfer coefficient to the cryogen is quiet complex and difficult to calculate accurately. However, depending on winding details, approximate heat transfer coefficient in nucleate boiling situation may be determined.

3.8.1 Heat Transfer with Pool Boiling Liquid Helium-I

Boiling heat transfer plays an important role in stable operation of the superconducting magnet cooled by saturated liquid. Heat transfer with boiling normal liquid helium is controlled by natural convection mechanism: nucleate boiling for slight temperature differences and film boiling leading to large temperature difference. The turn over from nucleate to film boiling state depends on the characteristics value of peak nucleate boiling flux (PNBF) and minimum film boiling flux (MFBF). Depending on the geometry, orientation of heating surface, space for cooling channel, nature of surface, the temperature and pressure of helium bath, heat transfer behaviour changes. The restricted channels size in between winding layers reduces the PNBF. Following Wilson [78] effect of channel size on PNBF in vertical channels is given by the semiempirical correlation as

$$h_{PNBF} = \frac{1800}{z^{0.5}} \cdot \frac{s}{(s + 1.1\times10^{-3} + 3.7\times10^{-4} m)} \tag{3.42}$$

Where z is the channel height, s is the separation between the heated surfaces, m is a correlation parameter between 1 and 2 depending on one or both surfaces are heated. For the interlayer gap (s) of 1 mm, the PNBF for channel height of 280 mm becomes 1.4 kWm^{-2}, which is much smaller than open-pool PNBF of 6-10 kWm^{-2}. For the purpose of present simulation PNBF of 1 kWm^{-2} is conservatively chosen, though perhaps the greatest uncertainty in the simulation is the modelling of cooling effect.

3.8.2 Quench Simulation Algorithm

A transient heat transfer model has been implemented to find the temperature evolution during quench. The magnet is initialized with uniform temperature distribution of 4.2 K and the initial current of 800 A. An external thermal disturbance is imposed for small time (~1-10 ms) at the longitudinal midpoint of length 1000 m (this can be changed further to verify the convergence) in the form of Gaussian distribution. The minimum injected energy resulting quench propagation is the measure of minimum quench energy (MQE). The power supply is assumed to be turn off and the current begins flowing in the coil and protection circuit.

The thermal diffusion equation (3.39) is solved numerically using finite difference method. The spatial derivatives are discritized in order to obtain a system of ordinary differential equations (ODE). To begin, the conductor length is discretized into N number elements of length dx each. Within each element, the temperature is assumed to be a function of time only.

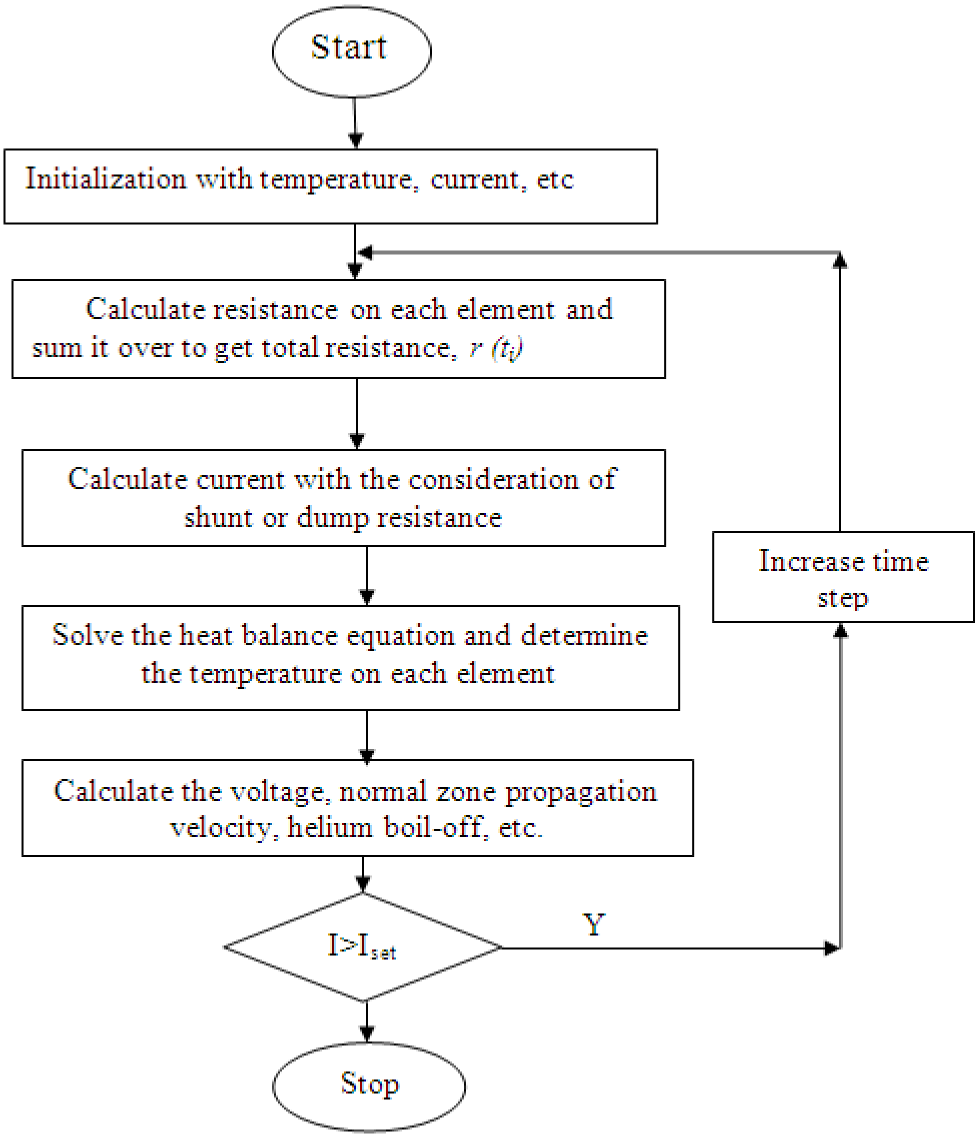

Figure 3.10: Flowchart of quench analysis study.

The temperature dependent material property is also constant at any instant in time. The electrical resistivity and thermal conductivity of composite material are considered both as a function of temperature and magnetic field during the process of time evolution in quench. By simultaneous solution of temperature in each element, a temperature profile *T(x,t)* for a given time instant is obtained. During iteration, the program uses a new temperature profile and updated the material property as well in each element. The basic algorithm of quench analysis is as shown in Figure 3.10.

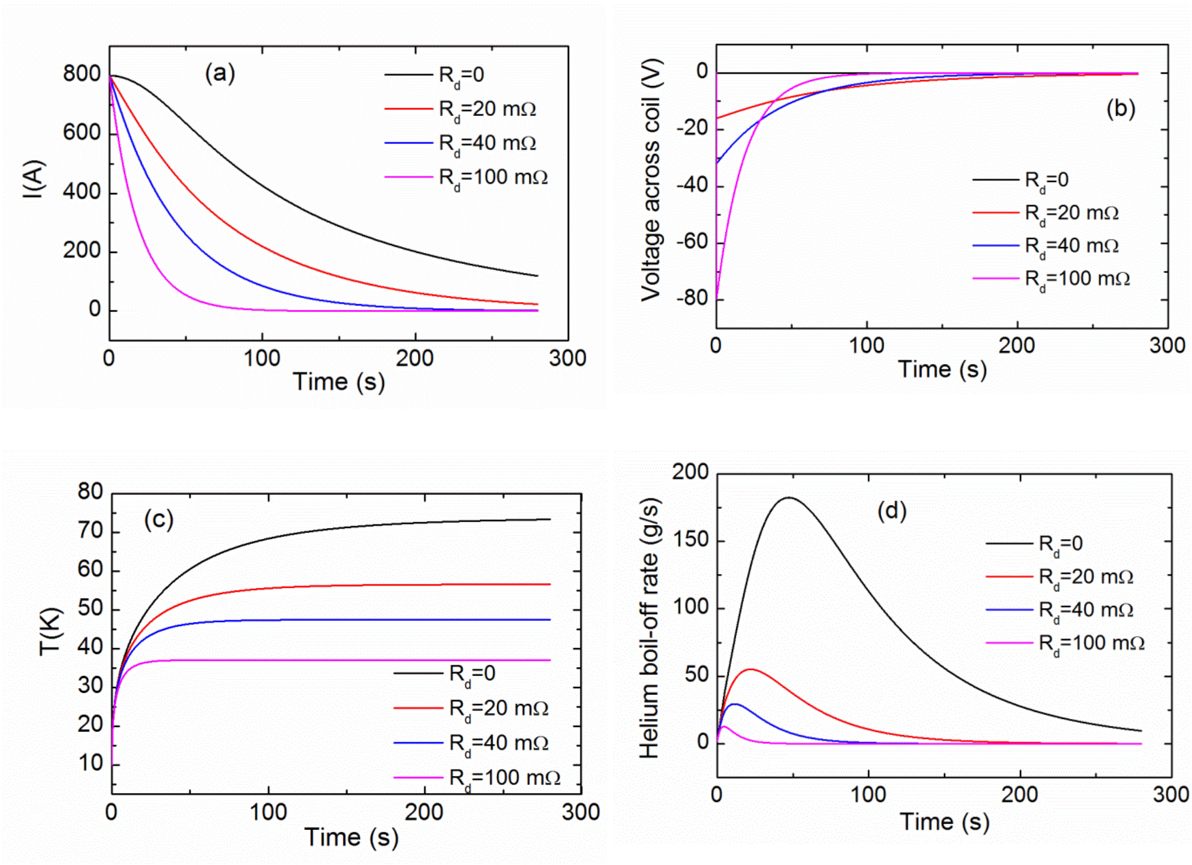

Figure 3.11: Quench study: (a) Current decay, (b) voltage across coil during quench, (c) hot spot temperature, (d) helium boil-off rate for various dump resistances.

The quench analysis end when the current drops below a predefined level. The simulation is repeated with different time steps and element length to check for numerical stability of the output data. For various dump resistors (R_d), the current decay in the coil, voltage drops across the coil, hot spot temperature, and the helium boil-off rates are shown in Figure 3.11.

The hot spot or the maximum temperature developed by propagating normal zones is related to protection method and dump or shunt resistor as well. It is observed that from the consideration of over voltage and over temperature, the coil is self-protected, i.e. R_d=0 Ω is also acceptable, however Figure 3.11 (d) shows that a considerable amount of liquid helium boil-off occurs in case of self-protection or no dump resistor outside. From the consideration of both helium boil-off and hence pressure built up, a dump resistance of 20 mΩ is chosen. Further, for the helium system the safety system is very important to design and implement. The relief valve is sized to protect cryogenic system in the event of loss of insulating vacuum to liquid helium.

3.8.3 Design of Dump Resistor

The dump resistor is used to absorb the stored energy from superconducting magnet. The design philosophy should be such that any correction of dump resistance value after fabrication can made easily. Therefore, modular design is imposed as shown in Figure 3.12. The material with high specific resistance such as stainless steel (SS-304) is desirable for developing the dump resistance. The dimension and number of the plates are determined with the commercially available thickness of the sheets such that the temperature rise is within 40 ^{0}C in still air cooling. The photograph of the dump resistor module is as shown in Figure 3.13.

The temperature rise up in the dump resistor is written as

$$m_d C(T)\frac{dT}{dt} = I^2(t) R_d(T) - h\frac{p}{A_s}(T - T_{amb}) \qquad (3.44)$$

$$R_d(T) = \rho_d(T)\frac{N_d\, l_d}{A_d} = R_d(0)\left(1 + \alpha_d (T - T_{amb})\right) \qquad (3.45)$$

Where *C(T)* is the specific heat of dump resistor material, *h* is the heat transfer coefficient from dump resistor surface to ambient atmosphere, α_d is the temperature coefficient of resistance, T_{amb} is the atmospheric temperature, N_d is the number of plates in series connection, l_d is the length of each modular plate. Suitably choosing the plate cross-sectional area for current flow and length (l_d), the required dump resistance specified is achieved.

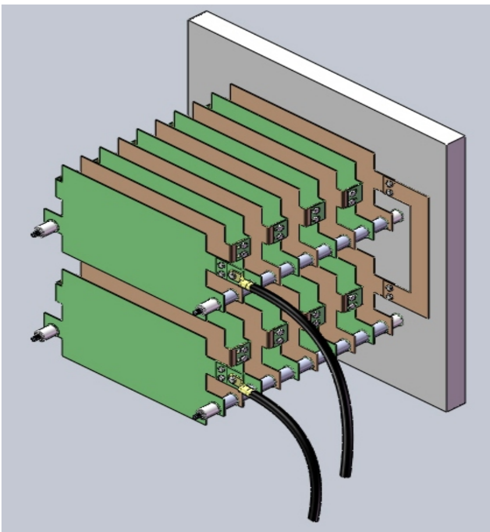

Figure 3.12: 3-D model of dump resistors made of SS-304L plate in modular form (400 × 250 × 2) mm.

Figure 3.13: Photograph of the dump resistor developed.

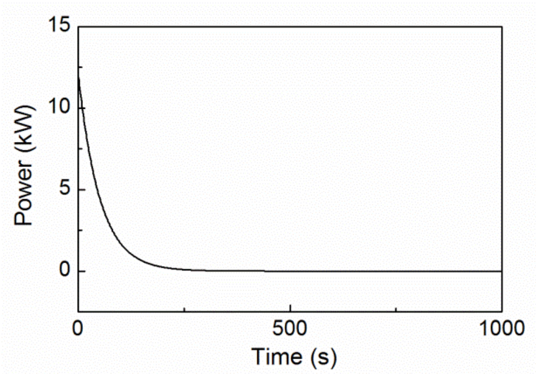

Figure 3.14 (a): Power dissipated across dump resistor during quench at 800 A.

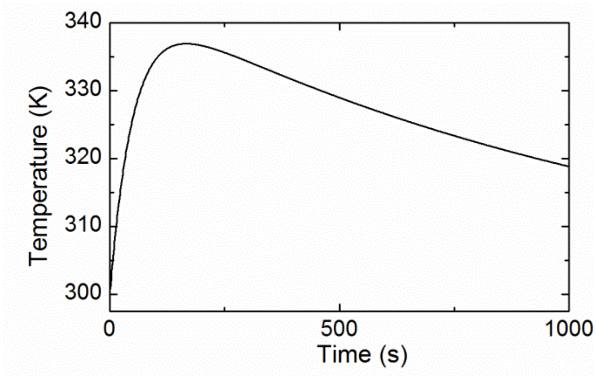

Figure 3.14 (b): Temperature rise up in the dump resistor during quench at 800 A.

For the purpose of present design, heat transfer coefficient in still air is conservatively assumed to be 5 $Wm^{-2}K^{-1}$. However, fluid flow modelling can be made and simulated to determine more accurate value of heat transfer coefficient, though it does not significantly affect the design. The power dissipated to the dump resistor and subsequently, the temperature rise up is estimated as shown in Figure 3.14.

3.9 Eddy Force on Helium Vessel during Field Transients

During fast magnetic field transient, eddy current develops on the thin-walled helium vessel that houses SMES coil. Electric field developed along a closed path is given by

$$\oint \vec{E}.\vec{d}l = -\frac{d\vec{B}}{dt};$$
$$or, \quad \vec{E}_\theta[y] = -\frac{1}{2\pi r}\dot{\vec{B}}_y[y] \tag{3.46}$$

Force per unit volume is

$$\frac{d\vec{F}}{dV} = \vec{J} \times \vec{B}_y, \text{ with } \vec{J} = \frac{\vec{E}}{\rho_s}$$

The pressure on the metal surface is given by,

$$p(z) = (\vec{J} \times \vec{B}_y)\delta = E_\theta[z]B_y[y]\,\delta / \rho_s \tag{3.47}$$

Where E_θ and B_y are azimuthal electric field and axial magnetic field calculated on the surface of helium vessel. Here, ρ_s is the resistivity of the helium vessel material at 4.2 K, δ is the thickness of helium vessel. Calculated inward (during charging of coil) or outward (during discharging of coil) pressure on helium vessel along the height of SMES coil is as shown in Figure 3.15. The critical collapsing or buckling pressure for cylindrical He-vessel of thickness to diameter ratio (δ / D) of 5×10^{-3} as in present case calculated is of three orders of magnitude higher with respect to the eddy pressure developed. Therefore, as per as induced force due to eddy current is concerned, helium vessel is safe from any buckling. There is also a vertical force on lateral faces of cryostat produced due to interaction of coil radial field with eddy current. This force can be estimated replacing B_y in equation (3.47) with radial component of field B_r.

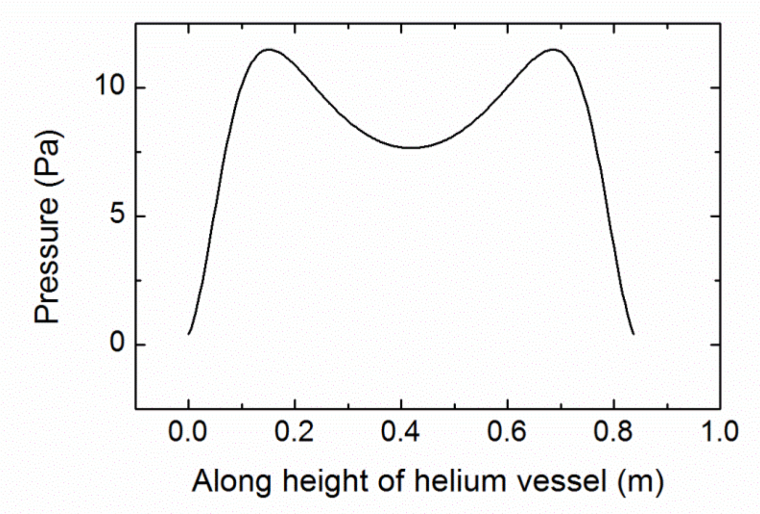

Figure 3.15: Radial pressure due to induced eddy current in helium vessel.

3.10 AC Loss/ Transient Loss

Evaluation of the AC loss is important for the SMES system in the sense that the loss determines the requirement of cooling capacity or in turn, transient cryogenic load. In general, the SMES system is operated as DC energy storage mode. But, during charging and discharging mode, high magnetic field transient occurs that introduces cryogenic loss (i.e. eddy current, hysteresis and coupling loss in superconducting coil and its structure) inside the cryostat.

3.10.1 Eddy Loss in Cu Stabilizer

Eddy loss in copper channel of conductor in presence of transient axial field using slab model can be written as,

$$p_{cu,y}(W/m) = \frac{f_y b a^3}{12\rho_{cu}} \dot{B}_y^{\,2} \tag{3.48}$$

Here, ρ_{cu} is the average electrical resistivity of copper at 4.2 K. The cross-sectional dimension ($a \times b$) of unit cell (conductor cross-section) is as shown in Figure 3.16.

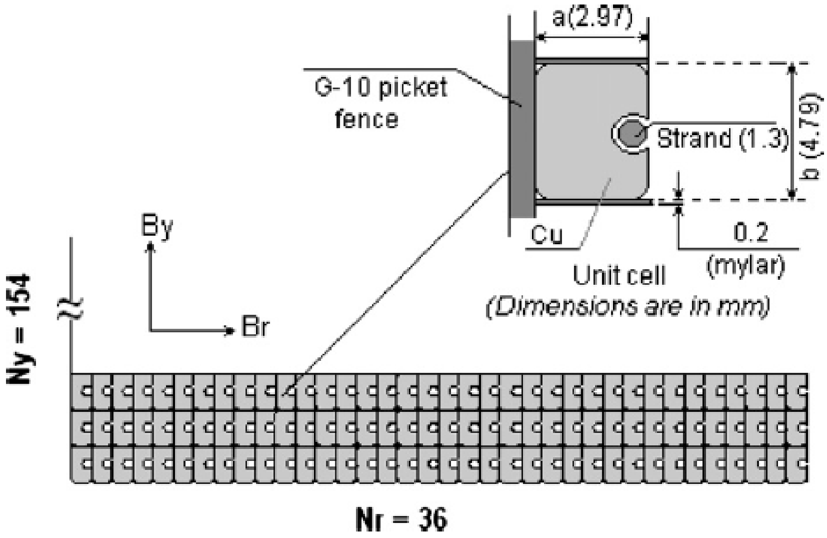

Figure 3.16: Winding cross-section with illustration of unit cell.

The geometric correction factor (f_y) for axial field due to the presence of circular channel is calculated for a unit cell by comparing the loss to the Finite Element Analysis (FEA) simulation result. The eddy current distribution for axial field transients of 1.2T/s at a time snap of 2 s is as shown in Figure 3.17 and the corresponding magnetic field is as shown in Figure 3.18.

Eddy loss due to radial field transient can be written as

$$p_{cu,r}(W/m) = \frac{f_r\, a\, b^3}{12\rho_{cu}} \dot{B_r}^2 \tag{3.49}$$

Here a = 2.97 mm, b = 4.79 mm. The geometric correction factor (f_r) is calculated in the same way as f_y. . Validating the transient loss on a unit cell with FEM analysis (ANSYS), we find $f_y=0.98$ & $f_r=0.62$. Considering the contribution from all unit cells, total eddy power is written as follows:

$$P_{cu}(W) = \sum_{i=1}^{n_r}\sum_{j=1}^{n_y}[p_{cu,y}^{i,j} + p_{cu,r}^{i,j}](2\pi\, r_{i,j}) \tag{3.50}$$

Here, $r_{i,j}$ is the radial position of each unit cell at i^{th} layer and j^{th} turn.

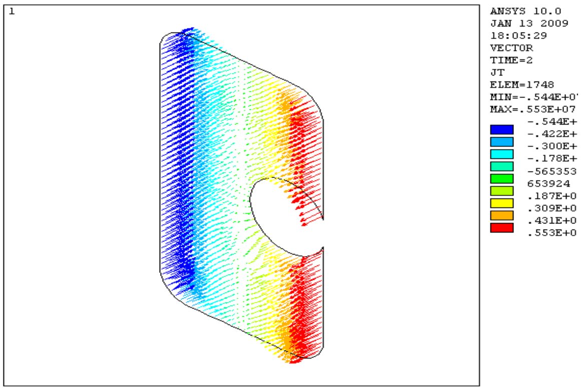

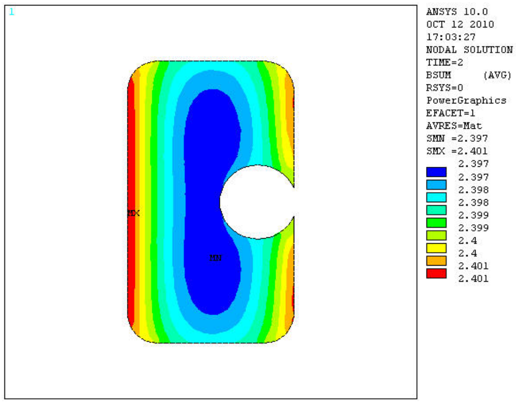

Figure 3.17: Eddy current distribution due to maximum axial field transient (1.2 T/s) at 2 s.

Figure3.18: Field distribution during maximum field transients (1.2T/s) at 2 s.

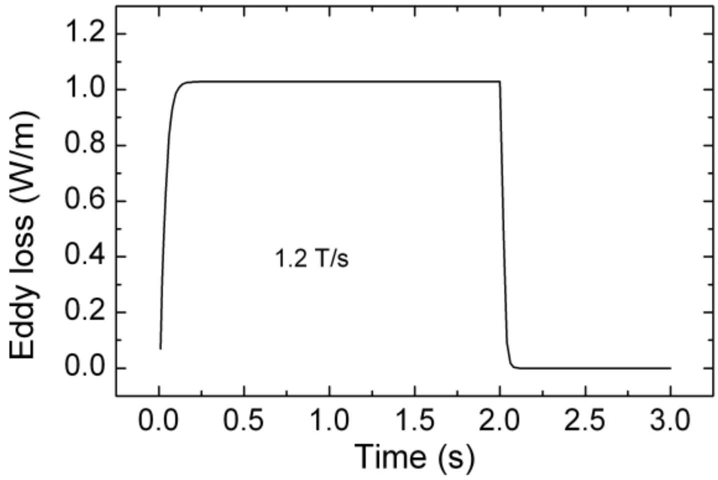

Figure 3.19: Time dependent eddy power due to field transient of 1.2 T/s.

The magnetic field enclosed by various turns and layers are considered in order to calculate the total eddy loss contributed by copper channel of the superconductor. The transient eddy loss in copper channel due to both axial field and radial field transients corresponding to 0.1 MW power discharge (~ 1.2 T/s) to the load is as shown in Figure 3.19.

3.10.2. Loss in Superconductor

In the single strand superconductor (as in our case), the primary losses are due to eddy current flowing between filaments (coupling loss) and hysteresis in the superconductor. The hysteresis loss in unit cell is

$$p_h^{i,j} = \frac{n_f}{\mu_0 T_m}\left(\int_{B_{i,j}^{initial}}^{B_{i,j}^{final}} M\, dB\right)(2\pi\, r_{i,j})A_f \tag{3.51}$$

Where A_f is the cross-sectional area of each filament, n_f is the number of filaments, T_m is the discharge period, and M is the magnetization given by

$$M = \frac{2}{3\pi}\mu_0 J_c d_f\left(1 - \frac{J}{J_c}\right) \tag{3.52}$$

Where d_f is the diameter of superconducting filament, *J(B)* is the current density at some instant of discharge, and $J_c(B)$ is the critical current density at the filament's field and operating temperature.

Considering each unit cell, total hysteresis loss is

$$P_h(W) = \sum_{j=1}^{n_y}\sum_{i=1}^{n_r}(p_{h,y}^{i,j} + p_{h,r}^{i,j}) \tag{3.53}$$

where $p_{h,y}$ and $p_{h,r}$ represents hysteresis loss part due to axial and radial field respectively. Coupling loss among filaments of a unit cell can be written as,

$$p_c^{i,j} = \frac{\dot{B}_{i,j}^2}{\rho_t}\left(\frac{l_p}{2\pi}\right)^2 \lambda\, A_{cell}(2\pi\, r_{i,j}) \tag{3.54}$$

where l_p is filament twist pitch, A_{cell} is unit cell cross-section, λ is the fraction of superconductor in unit cell, ρ_t is the effective transverse resistivity of the matrix.

Summing up contribution of each unit cell, coupling loss can be written as

$$P_c(W) = \sum_{j=1}^{n_y}\sum_{i=1}^{n_r}(p_{c,y}^{i,j} + p_{c,r}^{i,j}) \tag{3.55}$$

Where, $p_{c,y}$ & $p_{c,r}$ represents coupling loss due to axial and radial field respectively.

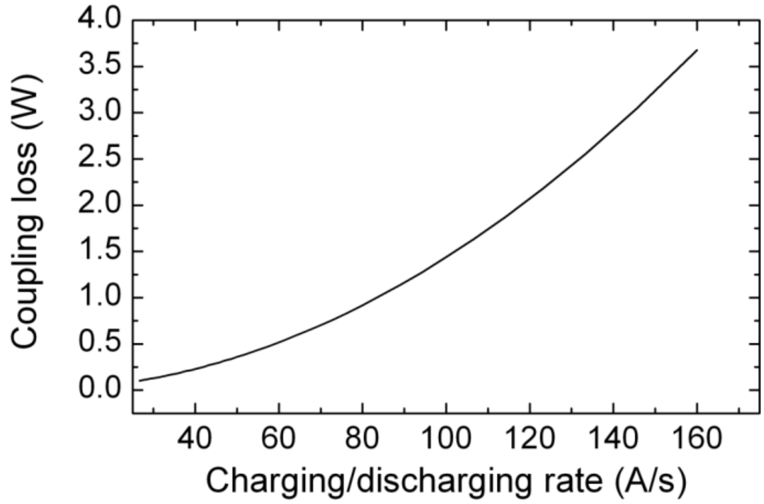

Figure 3.20: Coupling loss across the superconductor filaments in the winding for various discharge rates.

The coupling loss across the filaments in superconductor in winding for various discharging rates is as shown in Figure 3.20. The overall eddy loss contributed by Cu channels as well as coupling current in superconductor is estimated and compared to measured value in the next chapter.

3.11 Conclusions

The general purpose design optimisation methodology to minimize required conductor length for a given stored energy is developed for solenoid-type SMES and is implemented to develop a 0.6 MJ SMES system. The practical design constraints such as the critical behaviour of superconductor, mechanical stress on the winding, stability margin against quench-like scenario, *etc.* has been considered and differential evolution method has been implemented to find geometrical as well as operating parameters. Detailed stress analysis and quench protection scheme has also been presented in this chapter. Passive shielding is developed around the coil cryostat to reduce the stray magnetic field outside to an acceptable limit.

CHAPTER 4

REALIZATION OF 0.6 MJ SMES COIL AND FUNCTIONALITY TESTING

Coils winding with a given pre-tension and on-line joint development, *etc.* are major issues for the successful development of SMES coil. This chapter describes the coil winding scheme, instrumentation in the coil, quench detection methodology, integration of the coil with power converting system (PCS) to mitigate voltage dip, cold test and finally, demonstration of its functionality. Finally the coil is integrated with power conditioning system (PCS) and functionality is tested for voltage dip mitigation with various durations. The SMES coil is charged up by suitable duty cycle of DC link voltage in DC-DC chopper and freewheels in the chopper circuit at the normal operation mode. Intentional power interruption with different carry over period is made and stored energy of SMES magnet is discharged by the chopper that maintains constant DC link voltage so that three phase output voltage remains constant across the load.

4.1 Coil Winding and Integration with Magnet Dewar

In order to keep the operation stability and reliability, the SMES system is designed with cryostable multifilamentary NbTi/Cu superconducting wire embedded in Cu channel. Winding of the SMES coil is performed with custom-built winding machine with the required pretension. The basic structure of the coil consists of helical winding on a stainless steel former. A polyimide tape of 100 µm thickness is used to provide inter-turn insulation in a given layer. The coil consists of 36 layers and a gap was placed with 1 mm thick fiber reinforced plastic (FRP) spacer among successive layers for cooling channel and inter-layer insulation. Stainless steel coil former (SS-304L) is chosen due to similar thermal contraction of NbTi/Cu superconductor and SS-304L. Coil former thickness of 5 mm is chosen considering both hoop stress and structural load point of view.

Figure 4.1: Photograph of coil during assembly inside the cryostat.

A minimum winding pre-stress (~13.6 MPa) is determined from the stress analysis and applied while winding the coil that ensures the conductor remained compressed (i.e. radial stress is negative) against the bobbin when both cool-down and magnetic load are applied. Coil after fabrication is top mounted as shown in photo (Figure 4.1) on a standard magnet dewar (SMD) by three stainless steel (SS-316L) rods. The annular chamber surrounding the helium vessel with multilayer insulation is maintained with a vacuum level of better than 1E-06 mbar. Considering the worst possible scenario of magnet quench and vacuum insulation failure the safety devices like pressure relief valve and rupture disc is designed and implemented. The enthalpy of boiled off cold helium vapour is used for cooling the current leads (American Magnetics, USA make) on its way out of the cryostat. In addition, there is a liquid nitrogen cooled intermediate shield between helium reservoir and outer wall of the cryostat. The thermal load to the cryogenic system comes from thermal radiation, thermal conductance, and heating due to electrical joints in the superconducting wire, *etc.*

4.2 Instrumentation

Instrumentation is used to monitor cryogenics operation and to characterize quench propagation in the superconducting magnet. Temperature, pressure, helium mass flow, magnetic field, liquid helium level, etc are the primary important parameters to be measured to ensure the functionality of the magnet coil. Lakeshore Cryotronics makes Cernox sensor (negative temperature coefficient) and silicon diode (DT-470) is used for temperature measurement in the range 4-300 K.

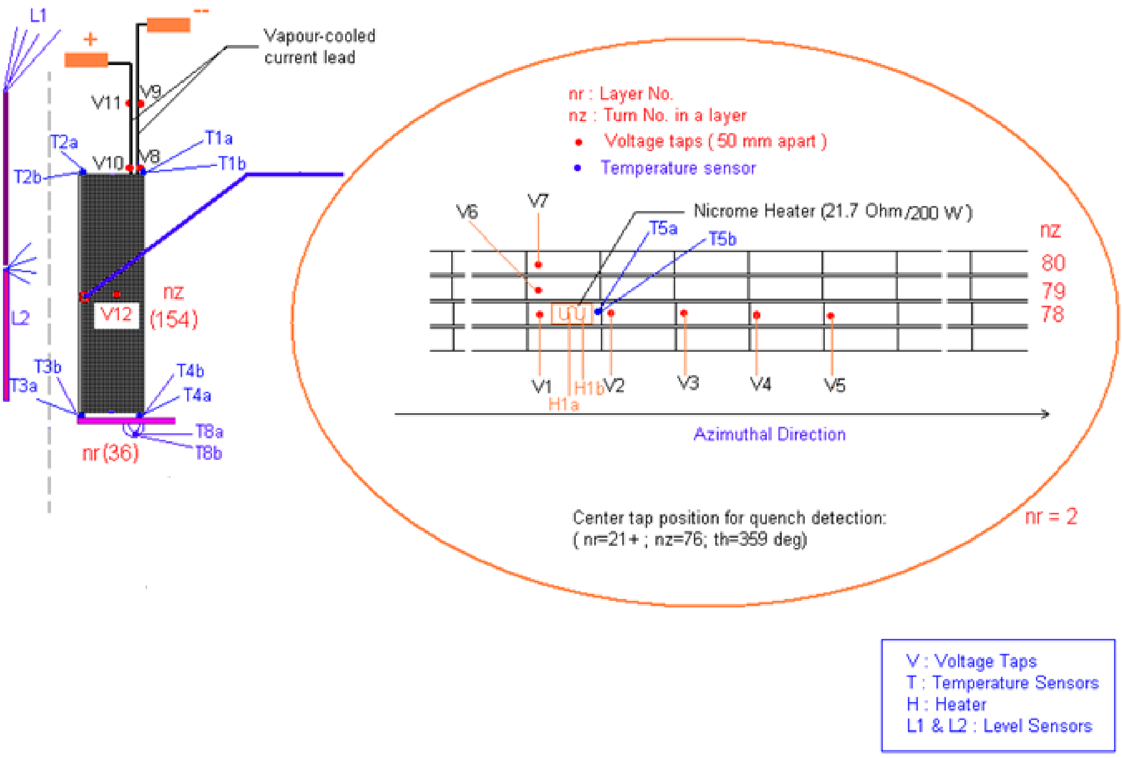

Figure 4.2: Details of coil instrumentation scheme: L1 & L2 are liquid helium level sensors, T's are temperature sensors, V's are voltage taps, H stands for heater to provoked quench.

The resistance of Cernox sensor is low at high temperature and increases exponentially when the temperature lowers to less than 50 K and therefore, its sensitivity increases at lower temperature.

Thermal conductivity measurement based mass flow meter (Alicat, USA) is used for flow measurement. The coil is also equipped with many voltage taps to study provoked quench scenario and also to detect threshold voltage for quench like occurrence. The voltages across the vapour-cooled current leads are also monitored and connected to the data acquisition system. The thermal sensors, voltage taps, liquid helium level sensors, coil current, volume and mass flow rate of boil-off helium gas, cryostat pressure, *etc.* are connected to the data acquisition system with a computer to record the data. Detail of the instrumentation scheme is as shown in Figure 4.2.

4.3 Cool-down to operating temperature

The annular space of the magnet dewar is kept under vacuum of the order 6.0 E-6 mbar by turbo-molecular pump backed with scroll pump. The 0.6 MJ SMES coil system with cold mass of 850 kg was initially pre-cooled with liquid nitrogen at 77 K. Prior to cool-down by liquid helium, liquid nitrogen was taken out of magnet dewar by over pressurization with pure helium gas followed by pure helium gas purging and evacuation of the magnet chamber to roughly 20 mbar absolute. Intermediate liquid nitrogen radiation shield vessel of magnet dewar was filled with liquid nitrogen. Helium gas purging and evacuation was carried out several times and it was ensured that magnet chamber did not have any trace of liquid nitrogen. Cooling with liquid helium is carried out quiet slowly (~12 K/hr) in order to utilize the sensible heat of cold helium gas. The photograph of magnet dewar with cryogenic system, instrumentation racks, *etc.* is as shown in Figure 4.3. The typical cool-down characteristics of the coil is as shown in Figure 4.4.

Figure 4.3: Photograph of instrumentation panel and cryogenic system of 0.6 MJ SMES coil.

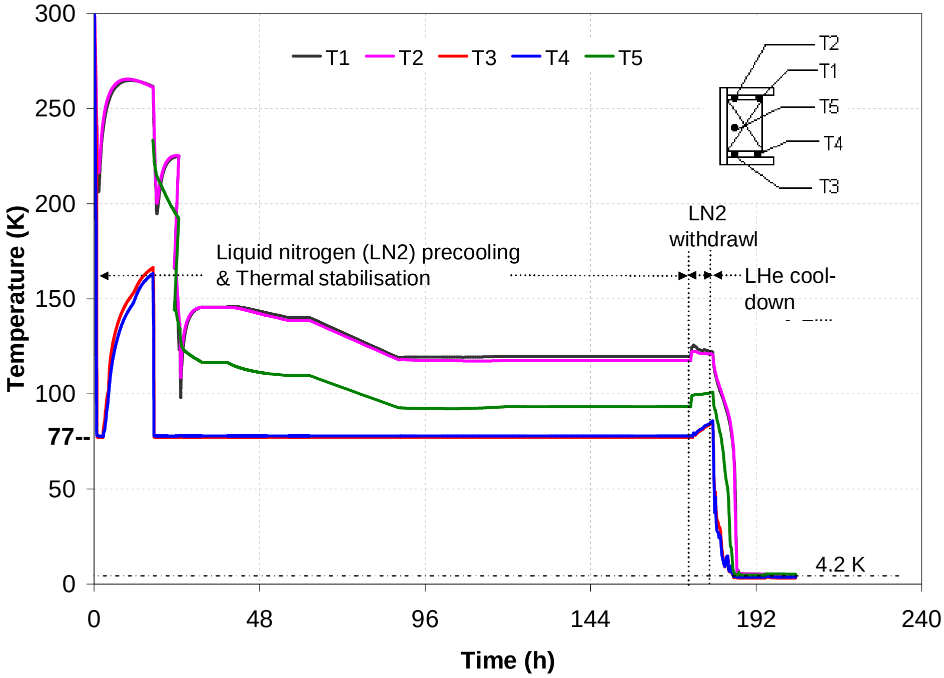

Figure 4.4: Typical cooldown characteristics of the coil.

4.4 Field Test and Quench Study

Prior to the integration with power conditioning system, the SMES coil is excited with DC current source (1500A, 20V). After cool-down and liquid helium filling above the top of the coil, magnet was energized up to 800 A. Magnetic field measured at the center of the coil for various excitations to find the load line is as shown in Fig. 4.5 and it conforms to design data with a fairly good accuracy. While ramping up the coil with various current ramp rates, dc inductance of the coil (L_{SMES}) is measured to be 1.89 ± 0.05 H that confirms the designed value of inductance.

It is observed that the temperature rise is limited due to large heat capacity of helium and high Cu to superconductor ratio and calculated to be around 55 K for a dump resistor of 20 mΩ, which is reasonably in good agreement with the experimental data of a provoke quench at full excitation of 800 A as shown in Figure 4.6.

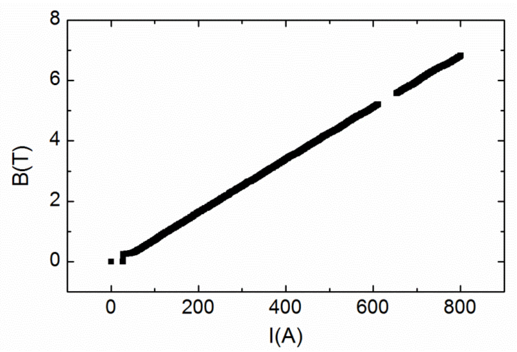

Figure 4.5: Measured load line of the coil.

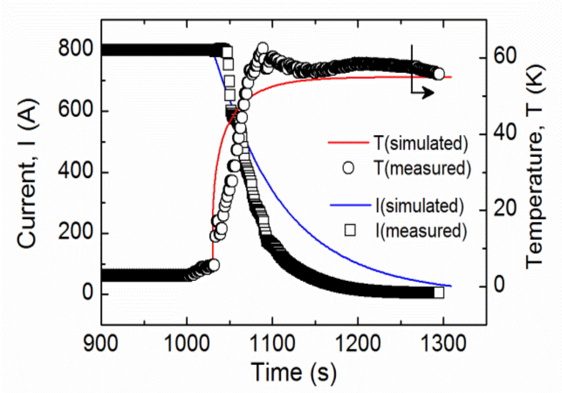

Figure 4.6: Current decay and temperature built-up during quench.

It is found that the time constant for current decay is more than simulated. This is may be due to complex heat transfer coefficient at the layer where hot spot occurs. However, the simulation provides a fairly reasonable agreement with experimental data. Voltages (V1 and V2 developed across center tap to upper half and center tap to lower half of the coil respectively) during a provoked quench (lowering liquid level to 90 % of coil height) is measured as shown in Figure 4.7. Since quench evolution started from the upper half of the coil due to lowering of liquid helium level, magnitude of V1 is higher than V2. The quench detection system activated when the voltage developed is more than preset threshold voltage of 200 mV for a validation period of 100 ms.

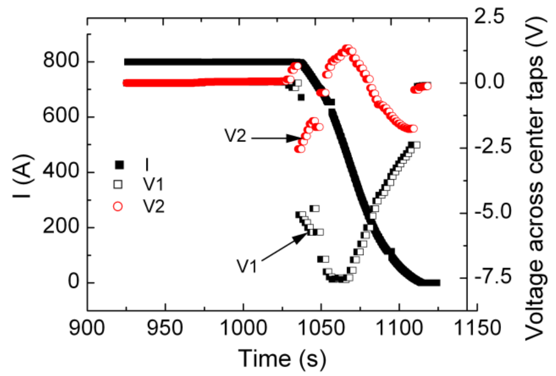

Figure 4.7: Voltage built-up across the coil during quench.

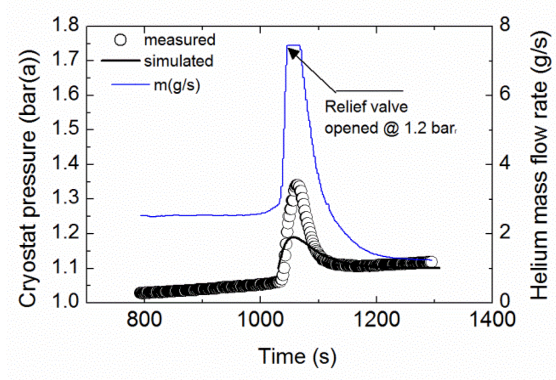

Figure 4.8: Mass flow and pressure built-up during quench.

The maximum pressure inside the cryostat during quench of entire coil is simulated to be 1.2 bar (a), which is somewhat less than the measured value as shown in Figure 4.8. This may be due to the fact that transient and other steady state loss not considered during quench simulation.

4.5 AC Loss Measurements

The SMES coil operates dynamically in power system either to absorb or release large power within some milliseconds to seconds. Therefore, performance of SMES coil should be stable than other common coils. Total loss as calculated from equations (3.49-3.55) is compared with calorimetrically measured loss during several discharge rates as in Figure 4.9. Precision helium mass flow meter (calibrated for helium gas with accuracy of ±1.0 % of full scale) has been used the measure the flow rate during ramp up/ down. Correction for temperature and pressure is incorporated to calculate the mass flow rate. Integrating the transient mass flow (g/s) during ramp up /down over time until steady state gives the total mass of helium evaporated. Care has been taken to exclude loss due to current leads.

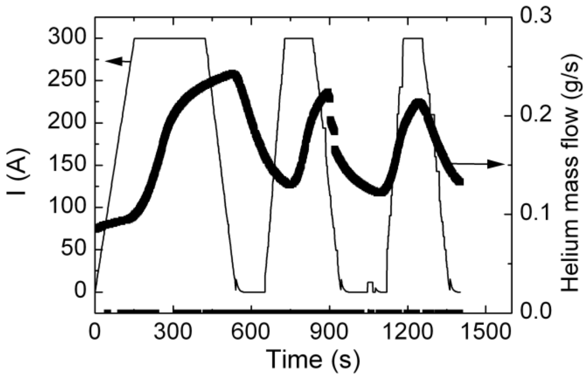

Figure 4.9: Evaporated helium gas with excitations at different ramp rates.

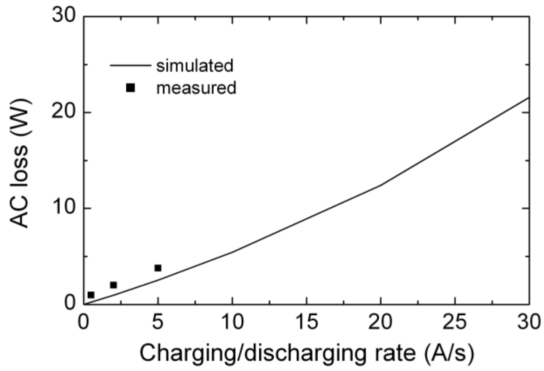

Figure 4.10: AC loss at various ramp rates of coil current.

The measured loss is somewhat higher than that calculated. This might be due to the contribution of other metallic components inside the cryostat such as Stainless Steel (SS-304L) former of the coil, Nb_3Sn sandwiched OFHC bus bar between vapour-cooled current leads and coil, stainless steel helium container, three stainless steel support rods (10 mm diameter) through which coil is suspended, *etc.* A simple calculation from Faraday's law gives the power dissipation due to eddy current for a metallic cylinder (axis parallel to field, B_y) of resistivity ρ_s, height H, radius r and thickness Δr as,

$$P_{eddy} = \frac{\pi \dot{B}_y^2 r^3 \Delta r H}{2\rho_s} \tag{4.1}$$

For example, SS former experiences field transient of 0.042 T/s corresponding to current discharge rate of 5A/s. Considering the resistivity of stainless steel $\rho_s(at\ 4.2\,K) = 5\times10^{-7}\,\Omega m$, eddy loss for the former becomes around 0.02 W. Similarly contribution from other components can be estimated. Due to limitation in DC power supply, it was not possible to measure the loss at further higher ramp rate, but it can be guessed to be little more than our estimated value. Boil-off helium gas with various ramping up and down rate has been measured as a function of current which gives an indication of AC loss in the coil is as shown in Figure 4.10. Form the plot, it is very evident to observe that one should allow sufficient hold period at higher excitation levels in order to accurately predict AC loss in calorimetric method since the helium evaporation, pressure build up in the magnet dewar, *etc.* are relatively slow process. The temperature increase of the conductor due to eddy current during charging/discharging of the magnet coil is found to be negligible because of appreciable heat transfer coefficient to liquid helium as well as heat capacity of the copper channel of the conductor.

4.6 Power Converter System (PCS)

The PCS system chosen for this SMES system incorporates voltage source inverter (VSI) placed in series between the source and load. The SMES system consists of injection transformer, rectifier or a voltage source converter (VSC) using IGBT, voltage source inverter (VSI) using IGBT, a DC link capacitor, a two quadrant DC-DC chopper using IGBT as shown in the following scheme as shown in Figure 4.11. The superconducting coil is charged or discharged by adjusting the average dc voltage (DC link voltage) across the coil to be positive or negative values by means of duty cycle (D) of DC-DC chopper. The coil is either charging or discharging when the duty cycle is made larger than 0.5 or less than 0.5 respectively. When the coil is on stand-by or free-wheeling mode, the duty cycle (D) is maintained to be at 0.5. Performance of the SMES system is largely determined by the suitable design and performance of controller and DC-DC chopper.

The advantage of using series configuration is that detection of voltage sag is less complicated with respect to a parallel configuration. When quench occurs, the protection circuit detects the resistive voltage of normal zone, activates the protection system by turning on the DC contactor switch.

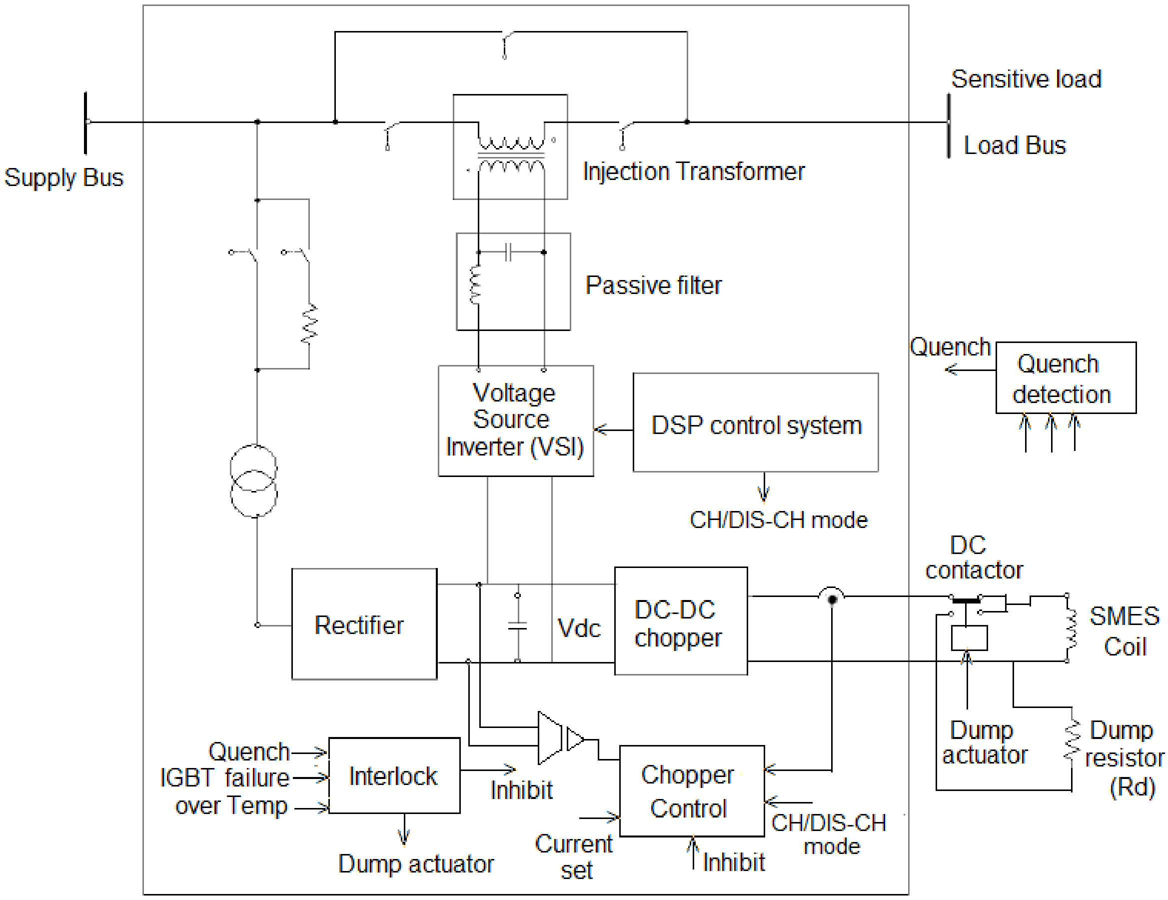

Figure 4.11: Layout of SMES system connected with power conditioning system (PCS).

4.6.1 Two-Quadrant DC-DC chopper

The chopper comprises of two-quadrant chopping circuit that is reversible in voltage. A DC-DC chopper is required for charging the superconducting coil to its rated current for energy storage and to discharge the stored energy to a constant DC-link capacitor. The Insulated Gate Bipolar Transistor (IGBT) based chopper with DC link voltage of ~80V as required by the VSI, components and its control algorithm is developed in the centre. The control algorithm implements logic for charging, free-wheeling and discharge mode of operation. The control algorithm of charging, free-wheeling and discharge mode of operation is as shown in Figure 4.12. In the charging mode, chopper acts as a rectifier to charge the SMES system. During charging mode, duty cycle (*D*) of IGBT switch S1 is controlled so that SMES coil charges to rated value. The coil current during charging is given as

$$I(t) = \int_0^t \frac{V(t)}{L_{SMES}} dt + I(0) \tag{4.2}$$

Here, *I(0)* is the initial current in the coil at charging start time, *t* is the time, *V(t)* voltage across the coil at time instant, *t*.

When the current reaches the rated value, the SMES will be switched into free-wheeling mode. In the freewheeling mode, the current circulates in a close loop as shown in Figure 4.12 (b).

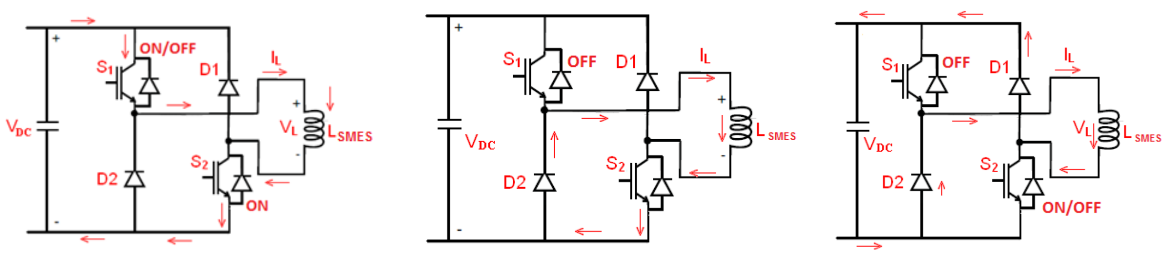

(a) **(b)** **(c)**

Figure 4.12: (a) DC-DC chopper in charging, (b) free-wheeling, (c) discharging mode of operation; S_1 & S_2 are IGBT switches; D1 & D2 are diodes; V_{DC} is the voltage across DC link capacitor bank; L_{SMES} is the inductance of SMES coil.

If a power interruption occurs, the stored energy in the SMES magnet is discharged by the chopper, which maintains constant DC link voltage so that VSI keeps controlling the three phase output voltages. In this mode, chopper uses voltage cycle control strategy and VSI operates as an inverter to release energy to the critical load. During discharge mode of operation, the coil current at any instant of time, t is given by

$$\frac{1}{2} L_{SMES}\, I(t)^2 = \frac{1}{2} L_{SMES}\, I(0)^2 - \frac{V_{coil}^2}{R_L} .t \quad ; \qquad 0 < t < t_{\max} \tag{4.3a}$$

$$V_{coil} = (1 - 2D) V_{DC} \tag{4.3b}$$

Where, R_L is the resistance of the load, D is the duty cycle of the chopper IGBT switch during discharge. The maximum carry over period, t_{max} is given as

$$t_{\max} = \frac{E_S}{P} \tag{4.4}$$

Where, P is the energy discharging rate or load power and E_0 is the stored energy.

4.6.2 Three-Phase Voltage Source Inverter with DSP based Control

The voltage source inverter (VSI) converts the fixed DC voltage from a device into a variable frequency AC supply. A 10 kVA 3- ϕ VSI was designed and developed that compensates for the voltage sag in the utility mains so as to keep the load voltage constant, deriving power from the chopper controlled constant DC bus. A multi-channel ADC based data acquisition system integrated to the control block senses the voltage sag and controls the IGBT bridge of the VSI to maintain the load voltage constant using digital signal processing (DSP) based control. Once the fault event is over, the control system works such that coil recharges from the mains. Electrical aspect of the design and development of the dynamic voltage restorer (DVR) of power conditioning system is carried out by De et al [79]. The block schematic of the control system of the PCS is shown in Figure 4.13.

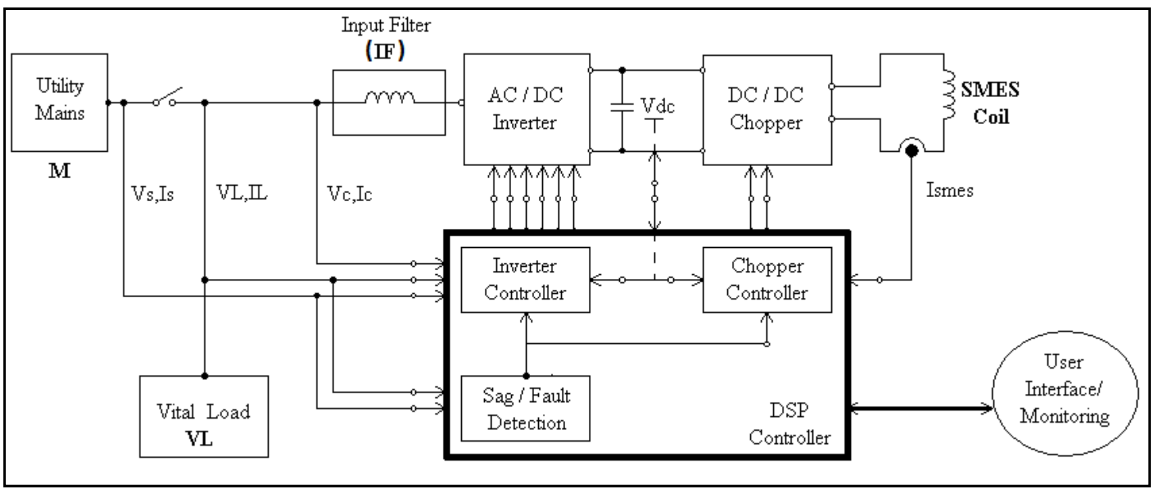

Figure 4.13: Block scheme of control system of PCS.

Space vector pulse width modulation (SVPWM) technique [79] is implemented due to its superiority over Sine PWM with regard to total harmonic distortion and easier implementation. Based on the SVPWM based control triggers the IGBT-based full wave bridge. The low pass filter attenuates the high frequency based signal and allows AC (50 Hz) that is stepped up by the injection transformer and add up to the mains to feed the load.

4.7 Functionality Test as SMES

The SMES system was tested under short time (up to 2-3 s) power dip to verify the functionality of the SMES system. A programmable power source (California Instruments, USA make 3-ϕ 300Vac, 16-819Hz, 45kVA power converter) or sag generator was utilized to function as the utility input mains in the test circuit as shown in Figure 4.14. The source was started with normal mains that conFigured the system to charging mode and energized the SMES coil. Figure 4.15 shows the current ramp profiles and the steady state conditions, controlled by the DC-DC chopper. Several voltage sags were generated by the source and is mitigated through discharge of SMES energy. Controller switching to discharge mode during sag and then reverting back to normal mode was recorded as were the locking and synchronizing of the DVR injection voltage with the mains.

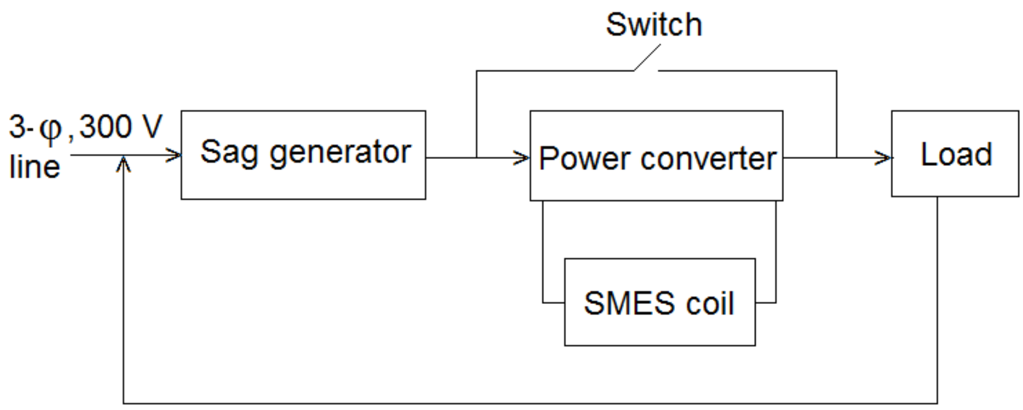

Figure 4.14: Functionality test circuit of the SMES system.

Though the SMES coil has been designed and tested in DC mode for 800A of current, its functionality is tested up to 400 A in the first phase with the power conditioning system with a delivered load of 4 kW due to restriction of limited available power rating of IGBT switches, *etc.*

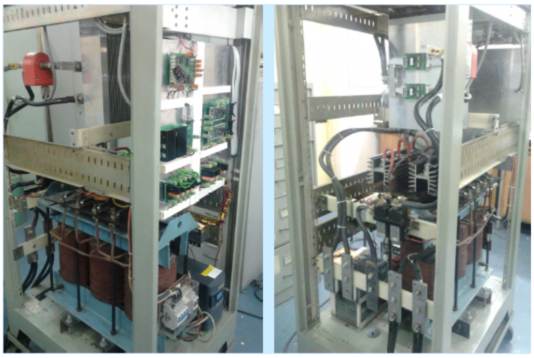

(a)

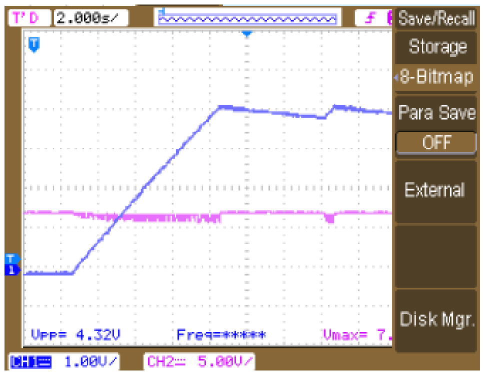

(b)

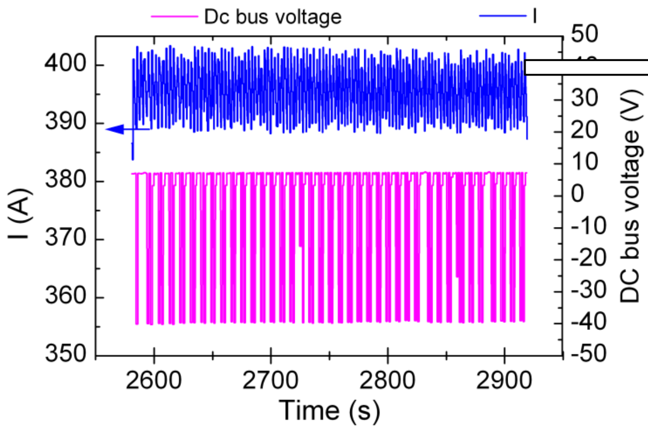

(c)

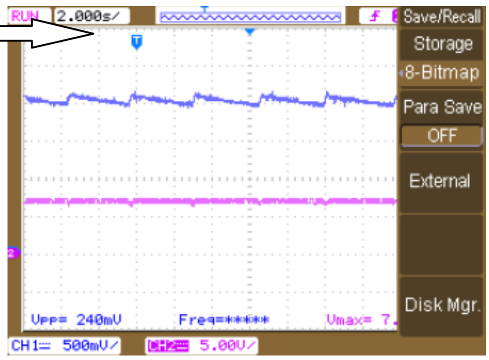

(d)

Figure 4.15: (a) Two quadrant DC-DC chopper module, (b) Waveform of current (blue) up-to 400 A during charging the SMES and associated and DC-link voltage (pink) in freewheeling mode, (c) Waveform of current (blue) up-to 400 A in SMES coil and DC-link voltage (pink) in freewheeling mode (d) Current (blue) and DC-link voltage (Pink) in zoomed time in freewheeling mode.

For different depth of voltage sags (10% to 90%), the waveform of DC bus voltage, coil current, and output voltage across sensitive load is measured with a representative plot as shown in Figure 4.16.

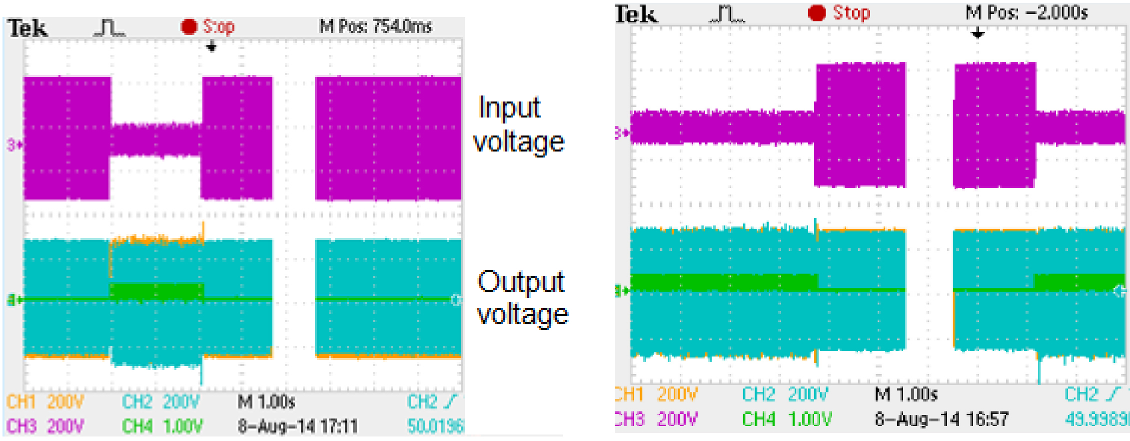

Figure 4.16: Mains input voltage (pink), load output voltages (blue, yellow), sag compensation actuating signal to VSI bridge (green) showing response when sag occurs (for two different sag periods).

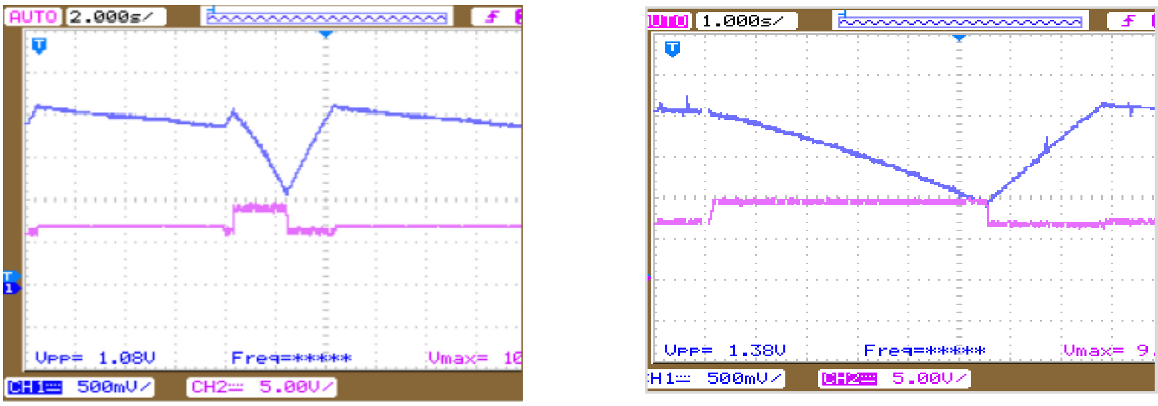

Figure 4.17: Coil current (Blue) and DC bus voltage (pink) during sag compensation of two different depths and durations.

During discharge mode, the coil current reduces linearly initially and more rapidly at the end of carry over period as shown in Figure 4.17 and begins to maintain the DC link voltage to the nominal supply voltage.

4.8 Summary and Discussion

A 0.6 MJ LTS SMES coil and cryogenic system has been built. The magnet was energized to the design current of 800 A without any quench and the operation of the magnet coil is successful. Quench simulation code developed is bench marked with the experimental data with a reasonable result. Transient cryogenic loss is also measured during charging and discharging and does not impose very significant load on the cryogenic system as the transient operation periods are in the order of few milliseconds to seconds. The SMES system was tested under short time power interruption and compensates power to the load. The chapter shows the physical layout of the power conditioning system. The control electronics enables the coil to discharge energy to a three phase ac load. Most of the specifications that were defined during the design are obtained and are in good agreement with what was expected.

CHAPTER 5

OPTIMISATION STUDY OF SOLENOID-TYPE COIL WITH RUTHERFORD-TYPE CABLE

After the commercial availability of 4 K cryo-refrigerator in recent years, it has been found that NbTi based low temperature superconductor (LTS) along with helium re-condensing technology is abetter choice for small scale SMES development as far as operational reliability and capital investment is concerned. A generalized optimization formulation has been developed for solenoid-type SMES coil with niobium titanium (NbTi) based Rutherford-type cable that minimizes the cryogenic refrigeration load into the cryostat, which in turn reduces the operating cost and opens up the possibility to adopt helium re-condensing system using cryo-refrigerator especially for small-scale SMES system. The corresponding optimal design of 5MJ class SMES coil using Rutherford-type cable is discussed as a case study. Effect of allowable hoop stress and maximum allowable voltage across the coil to the refrigeration load and coil parameters has also been investigated.

5.1 Mathematical Description

5.1.1 Stored Energy and its Dependence

The geometry of a solenoid (Refer to Figure 3.1) coil is defined by its inside radius (*a*), shape factor $\alpha = b/a$ and $\beta = l/a$, where 2 *l* is solenoid length and *b* the outside radius. The center magnetic field B_0 (α,β,a) and peak magnetic field B_m (α,β,a) on winding, stored energy $E(\alpha,\beta,a)$ for a thick solenoid coil of finite length may be written similar to as expressed in section 3.1.

5.1.2 Operating Current Density

In pool-boiling mode of operation, coil is immersed in a pool of liquid helium. The operating current of superconducting coil depends upon the critical characteristics of the superconducting cable, which is a strong function of peak magnetic field (B_m) inside winding and operating temperature. Considering the space or filling factor (λ) of the coil, the safety margin factor (ζ) over critical characteristics of the superconducting cable (i.e. J_C *vs* B), operating current density (J) of coil is determined in terms of coil peak field (B_m) as follows:

$$J(B_m) = J_C(B_m)\lambda(1-\zeta) \tag{5.1}$$

Safety margin factor ζ needs to be considered carefully depending on critical current degradation, minimum quench energy (MQE) of the cable, cooling and winding details, operating temperature margin, *etc.* However, for the present study we assume the operating current safety margin as 30 %. The safety margin factor ensures that the coil will not quench in normal operation. The winding packing fraction (λ) depends on winding details such as insulation thickness, inter-turn spacers, *etc.* Over the available type of conductor, Rutherford-type cable has been chosen for the present study since it offers relatively low AC loss and liquid helium bath cooling suitable for small-scale transportable SMES unit is feasible to adopt. For the present study, we assume the winding space factor (λ) as 0.85. However, depending on the winding scheme, insulation, *etc.* space factor needs to be determined appropriately. In order to relate the coil parameters with operating current density (J), J is fitted with peak magnetic field B_m in the following form as,

$$J(\alpha,\beta,a)=\frac{p}{q+\dfrac{B_m}{J(B_m)}} \tag{5.2}$$

Here, p and q are the parameters fitted from J vs. B_m/J plot. Substituting from eq. (5.2), operating current density can be expressed as,

$$J(B_m)=J(\alpha,\beta,a)=\frac{p}{q+\mu_0 a K_m(\alpha,\beta)} \tag{5.3}$$

For example, NbTi alloy based Rutherford-type cable as specified in Table 2.3 has measured critical characteristics as shown in Figure 5.1(a) and operating current density J at 4.2 K varies with B_m/J as shown in Figure 5.1(b). The fitted parameters are found as, p =7.6322 T and q = 1.42619×10^{-8} Tm^2/A for this particular cable.

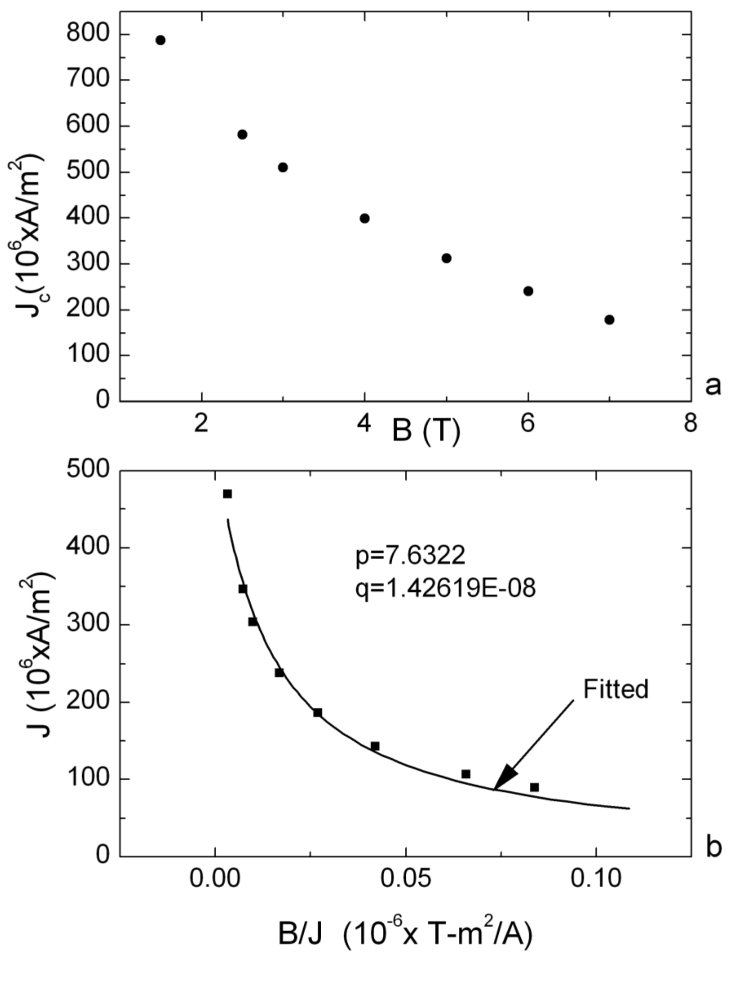

Figure 5.1: (a) Critical characteristics of the Rutherford-type superconducting cable, (b) Measured critical current is represented by, *J-B/J* fitting.

5.1.3 Magneto-structural Stress Consideration

The axial component of magnetic field (B_y) interacts with the conductor current density (J) in the coil and develops both circumferential stress (σ_θ) and radial stress (σ_r) components. However, the circumferential or hoop stress develops in the coil dominates over either radial or axial stress component on conductor. Further, it is hoop stress that is tensile in nature and limits the performance of the coil. Similar to section 3.3, maximum hoop stress developed at the median plane of inner layer of winding (i.e. at $r = a, y = 0$) of an isotropic solenoid-type winding with conductor Poisson's ratio of 1/3 is considered as a limiting constraints in design.

5.1.4 Peak voltage during discharge

During supply of constant power (P_0) by SMES coil to the critical load, energy stored in SMES coil at any instant of time *(t)* is

$$E(\alpha,\beta,a,t) = E_S(\alpha,\beta,a) - P_0 t \tag{5.4}$$

In designing a SMES coil of a given power rating, it is extremely important that the voltage developed across the coil is kept within safe value so that no electrical discharge, damage in insulation, *etc.* occurs. Initial voltage developed across the coil at time instant t=0 of discharge is written as,

$$V_i(\alpha,\beta,a) = \left.\frac{P_0}{J(\alpha,\beta,a)A_C}\right|_{t=0} \tag{5.5}$$

Where, A_C is cable cross-section of SMES coil. If $t=t_s$ is the carry over or discharge period and η the depth of discharge defined as fraction of stored energy discharged from the SMES coil, maximum voltage developed towards the end of discharge period in constant power output (P_0) mode of operation is expressed as,

$$V_m(\alpha,\beta,a)=\frac{V_i(\alpha,\beta,a)}{\sqrt{1-\eta\frac{P_0t_s}{E}}} \tag{5.6}$$

Here, η is the depth of discharge of SMES coil that defines the fraction of stored energy delivered to the load to maintain constant power P_0 over the discharge period of t_s. Similar to chapter 3, we consider η to be 0.7, i.e. 70% of the stored energy can be utilized during discharge operation for the present study. However, for voltage dip or sag compensation, η could be considered as low as 0.3-0.4. Depending upon insulation scheme of conductor, their vicinity, atmosphere, *etc.* maximum allowed discharge voltage, V_m is fixed to a safe value for a given stored energy E, maximum power rating of P_o and discharge period of t_s.

5.1.5 Average Magnetic Field Transient over Windings

If the coil current drops below a minimum value I_{min}, SMES cannot deliver constant power (P_0) to the load while discharge. During energy discharge at constant power rating P_0, coil current at time instant t is expressed as

$$I(t)=\frac{P_0}{V_m(\alpha,\beta,a)\sqrt{1-\eta}}\sqrt{1-\eta\frac{t}{t_S}} \tag{5.7}$$

Rate of change in current during discharge mode is

$$\frac{dI(t)}{dt}=-\frac{P_0\,\eta}{2\,V_m(\alpha,\beta,a)\sqrt{1-\eta}}\left(1-\eta\frac{t}{t_S}\right)^{-1/2} \tag{5.8}$$

Average rate of change in current during discharge over a period of t_S, the carry over period is

$$\left(\frac{dI}{dt}\right)_{avg}=\frac{1}{t_S}\int_0^{t_S}\frac{dI(t)}{dt}dt=-\frac{\eta P_0}{2\,V_m(\alpha,\beta,a)\sqrt{1-\eta}}\frac{1}{t_S} \tag{5.9}$$

Substituting Eq. (5.9), time average of magnetic field transient over magnet winding volume during discharge period of t_s as,

$$\dot{\overline{B}}(\alpha,\beta,a)=\frac{\overline{B}(\alpha,\beta,a)}{J(\alpha,\beta,a)\,A_C}\left(\frac{dI}{dt}\right)_{avg} \tag{5.10}$$

Since the magnetic field over the winding volume varies, average magnetic field $(\overline{B})$ over the winding is considered for loss calculation. Average of magnetic field $(\overline{B})$ over the winding is expressed as,

$$\overline{B}(\alpha,\beta,a)=\frac{1}{(b-a)l}\int_0^{\beta a}\int_a^{\alpha a}B(\alpha,\beta,a,r,y)dr\,dy \tag{5.11}$$

Axial field on the coil of finite thickness in any position ($a\le r\le b$, $-\beta a\le y\le\beta a$) is expressed [65] as

$$B(\alpha,\beta,a,r,y)=\frac{\mu_0 N(\alpha,\beta,a)J(\alpha,\beta,a)A_C\pi}{8\beta\,(\alpha-1)}\int_0^{\infty}J_0(k\,r)h(a,\beta,k,y)g(a,\alpha,k)dk \tag{5.12}$$

Where

$$h(a,\beta,k,y)=2-e^{-k(\beta a-y)}-e^{-ky},\quad -\beta a\le y\le\beta a \tag{5.13}$$

$$g(a,\alpha,k)=\frac{1}{ka}\left[-J_1\{ka)H_0(ka)+\alpha J_1(ka\alpha)+J_0(ka)H_1(ka)-\alpha J_0(ka\alpha)H_1(ka\alpha)\right] \tag{5.14}$$

J_0(x) and $J_1(x)$ are the Bessel function of first and second kind; $H_0(x)$ and $H_1(x)$ are the Struve functions. The functions are series expanded as shown in Appendix.

5.1.6 Refrigeration Load on Liquid Helium System at 4.2 K

The design goal in the present work is to minimize the refrigeration load into the cryostat. The refrigeration load includes the load into the liquid helium vessel at 4.2 K and the surrounding intermediate shield maintained at 60-80K. High magnetic field transient during charging and discharging operation of SMES coil leads to AC loss in terms of refrigeration load into the cryostat. Cryogenic refrigeration load at 4.2 K liquid helium vessel can broadly be categorised into two parts:

5.1.6.1 Dynamic Refrigeration Load at 4.2 K

Rutherford-type cable for solenoid-type coil winding of SMES use mainly experiences parallel or axial magnetic field to the cable broad surface since the radial field component in the winding space for the solenoid is very less with respect to axial magnetic field. Dynamic load originating from superconducting filaments and strands due to magnetic field transients primarily are:

It is caused by the induced persistent current in the filament. While the SMES unit is under discharge mode of operation for constant power output, the coil current drops decreasing the magnetic field and increasing the critical current. Hysteresis power dissipation (p_f) in filaments in presence of transport current density J and magnetic field transients during discharge operation is expressed as,

$$p_f(\alpha,\beta,a) = \lambda_{sc}\frac{2}{3\pi}J_c(B)\,d_f\,\dot{B}\left(1-\left(J/_{Jc}\right)^2\right)V(\alpha,\beta,a)$$

$$= \frac{(\lambda_{sc}/\lambda)}{(1-\varsigma)}.\frac{2d_f}{3\pi}J(\alpha,\beta,a)\,\dot{\bar{B}}(\alpha,\beta,a)\left(1-\lambda^2(1-\varsigma)^2\right)V(\alpha,\beta,a) \qquad (5.15a)$$

Where, d_f and λsc is filament diameter and volume fractions of superconductor respectively. It is important to note that magnetic field dependency of *Jc(B)* is indeed transformed into coil parameters.

Power dissipation (p_{cf}) originated by electromagnetic coupling among filaments in the strand through the matrix material is given by,

$$p_{cf}(\alpha,\beta,a) = \frac{\lambda_{wire}}{\rho_t}\left(\frac{l_p}{2\pi}\right)^2\dot{\bar{B}}(\alpha,\beta,a)^2 V(\alpha,\beta,a) \qquad (5.15b)$$

Where l_p is filament twist pitch, ρ_t is effective transverse resistivity across the matrix, which is considered to be constant (~9E-9 Ω-m) at operating temperature range at 4 K, and λ_{wire} is the volume fraction of filaments in a strand. In SMES like transient application, Cu-

0.5wt%Mn matrix material is preferred over copper matrix since it provides higher resistivity.

Power dissipation *(p_{cs})* due to coupling among strands in the Rutherford cable for magnetic field transients parallel to the broad surface (*2c*) of cable is written as,

$$p_{cs}(\alpha,\beta,a) = \frac{1}{8}\frac{\lambda_{cable} l_t}{R_a}\frac{d}{c}\dot{B}(\alpha,\beta,a)^2 V(\alpha,\beta,a) \qquad (5.15c)$$

Where, R_a is adjacent resistance per cross-over of strand, c and d are half width and half-thickness respectively of the cable; λ_{cable} is the fractions of superconducting strands in cable in the winding cross-sections; l_t is half the braid transposition length in the cable.

Total power dissipation due to dynamic loss would be:

$$f_{dy}(\alpha,\beta,a) = p_f(\alpha,\beta,a) + p_{cf}(\alpha,\beta,a) + p_{cs}(\alpha,\beta,a) \qquad (5.16)$$

5.1.6.2 Static Refrigeration Load at 4.2 K

It is very important to reduce the surface area of the SMES coil in order to reduce thermal radiation heat load into the cryostat. For ten layers (typically used) of multi-layer insulation (MLI) around the liquid helium chamber, heat load to liquid helium from 77 K intermediate thermal shield in a vacuum level of 10^{-6} mbar range is reported in literatures to be around, $q_r \sim 0.04\ W/m^2$ [80]. The helium vessel containing the cold mass at 4.2 K closely conform the coil structure. Static heat load to helium cryostat due to radiation and gas conduction in combination is proportional to the helium vessel surface area and is expressed as

$$f_R(\alpha,\beta,a) = q_r A_{He\_vessel} = q_r A_{coil}\,(1+\frac{x_1}{\beta a})(1+\frac{3x_1}{a(2\beta+\alpha)}) \qquad (5.17a)$$

$$A_{coil}(\alpha,\beta,a) = 2\pi a^2\{2\beta(\alpha+1)+(\alpha-1)\} \qquad (5.17b)$$

Where, A_{He_vessel} is the surface area of helium vessel containing cold mass, A_{coil} is the coil surface area, $x_1=x_{gap}+\Delta$ is the uniform distance of helium vessel outer wall from coil structure. x_{gap} is a uniform gap around the coil structure to helium vessel both in radial and axial direction neglecting details of buffer volume space, *etc*. The vessel thickness, Δ is assumed to be uniform. Typical value of x_{gap} is assumed to be 10 mm and thickness Δ to be 5 mm for the purpose of present analysis. However, the exact thickness of the helium vessel, *etc*. may be determined by detailed transient and static stress analysis.

Another significant static heat load comes from the current leads that depend on the operating current of the magnet, but independent of magnet size. Heat load for a pair of optimised vapour-cooled current leads where boil-off helium vapour is used for cooling of the leads is $q_{lead} = 0.002\ W/A$. Heat load from current leads may be written as:

$$f_{lead}(\alpha,\beta,a) = q_{lead} J(\alpha,\beta,a) A_C \tag{5.18}$$

Where, Ac is conductor cross-sectional area.

Therefore, total static heat dissipation neglecting the conduction heat load would be

$$f_{st}(\alpha,\beta,a) = f_R(\alpha,\beta,a) + f_{lead}(\alpha,\beta,a) \tag{5.19}$$

We have not considered the conduction heat load into the system, which is a strong function of coil weight and depends on many details of cryostat. However, in overall cryostat heat load budget, conduction heat load too needs to be considered.

5.2 The Objective Function

Total refrigeration load at liquid helium vessel at 4.2 K in the SMES cryostat is set as objective function since the refrigeration cost at 4.2 K is much higher than that of at 60-80K for intermediate shield. The problem, therefore, can be stated as follows [81]:

Minimize $f(\alpha,\beta,a) = f_{dy}(\alpha,\beta,a) + f_{st}(\alpha,\beta,a)$ (5.20)

Subject to constraints:

$$\begin{pmatrix} g_1(\alpha,\beta,a) = E(\alpha,\beta,a) - E_i = 0 \\ g_2(\alpha,\beta,a) = P(\alpha,\beta,a) - P_0 = 0 \\ g_3(\alpha,\beta,a) = \sigma_\theta(\alpha,\beta,a) - \sigma_m \le 0 \\ g_4(\alpha,\beta,a) = V_m(\alpha,\beta,a) - V_a = 0 \\ \alpha > 1.01 \\ \beta > 0.01 \\ a > 0.01 \end{pmatrix} \tag{5.21}$$

Here, E_i, P_0, σ_a and V_a are required stored energy, power rating, the allowable hoop stress in winding and allowable voltage across terminals respectively. We have intentionally use equality constraints for maximum allowed voltage across the coil since it will be connected in reality across a capacitor bank known as DC link of maximum rated voltage. Constraint on design parameters (*α, β, a)* are adopted to have a feasible solution space of design variables.

This is a multivariable nonlinear constrained global optimisation problem. In order to solve the problem successfully a simple and efficient global optimisation method i.e. the Differential Evolution (DE) method is employed to solve this problem. The algorithm of DE method is already discussed earlier in section 3.5. In most of the cases, convergence is observed with the number of iterations of around 3500 or less as shown in Figure 5.2.

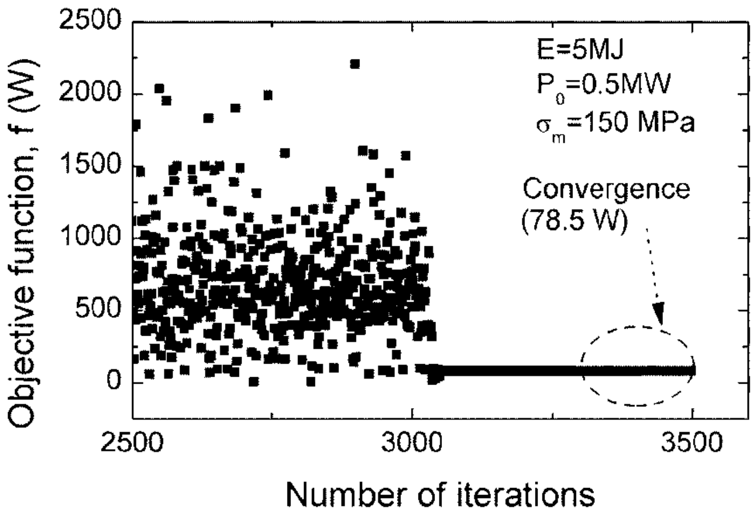

Figure 5.2: Convergence of objective function (*f*) with Differential Evolution (DE) algorithm.

5.3 Optimization Result

The design of SMES magnet in search of minimum static and dynamic heat load of superconducting wire/cable is a multi-variable non linear constrained optimization problem. Set of optimised result for 5 MJ SMES coil using liquid helium bath cooled Rutherford-type cable as case study is shown in Table 5.1.

Table 5.1: Design results of 5 MJ solenoid-type SMES coil using the NbTi based Rutherford-type cable for various peak power ratings.

Power (MW)	0.2	0.3	0.4	0.5	0.6
$f(W)$	51.5	70.5	114.5	148.3	169.2
$f_{dy}(W)$	50.6	69.2	112.7	146.0	166.4
$f_s(W)$	0.9	1.3	1.8	2.3	2.8
$a(m)$	0.292	0.254	0.211	0.192	0.184
α	1.27	1.17	1.135	1.107	1.082
β	1.58	3.2	6.844	11.33	16.4
$B_m(T)$	6.54	6.0	5.45	4.9	4.36
$B_{av}(T)$	2.98	2.58	2.52	2.34	2.11
$x(B_m/B_0)$	1.06	1.006	1.0	1.0	1.0
$I_{op}(A)$	374	561	748	935	1122
$\sigma_m(MPa)$	100	100	100	100	100
$V_m(kV)$	1.0	1.0	1.0	1.0	1.0
$t_{discharge}(s)$	17.8	11.9	8.9	7.0	5.9
$t_{charge}(s)$	31.1	20.7	15.5	12.4	10.4
$t_{cylcle}(s)$	48.9	32.6	24.4	19.4	16.3

The charging and discharging rate of superconducting coil is determined by the duty cycle of DC-DC chopper. The voltage against the SMES coil (V_{SMES}) and DC link (V_{DC}) is correlated with the duty cycle (D) of the chopper [82] as

$$V_{SMES} = (1-2D)\ V_{DC} \tag{5.22}$$

The duty cycle of the chopper circuit for the purpose of present design is such that in all cases 70% of the stored energy can be mitigated to the load at a given rated power. The dynamic and steady state refrigeration load for a given stored energy of SMES coil with practical design constraint is illustrated in Figure 5.3.

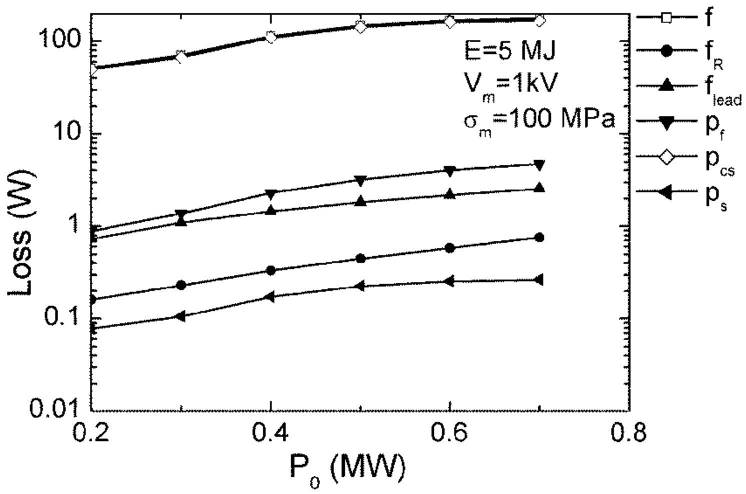

Figure 5.3: Variation of refrigeration loss with rated powers.

It is important to notice that the dynamic load is the dominating factor compared to steady state load. Coupling loss *(p_{cf})* across the filaments dominates over other dynamic loss components, which could be lowered by reducing filament twist pitch (l_p). The twist pitch of the filaments is considered to be 50 mm throughout the process of optimisation. However, if the twist pitch could be reduced to say, 30 mm, which may be realized and feasible, it is found that the dynamic load for 5MJ/0.5MW/1kV/100MPa system decreases considerably from 146 W to 55 W. Other sources of dynamic refrigeration load into the cryostat such as the metallic components like coil former, coil support, current lead bus bar, *etc.* will also contribute during transient operation and needs to be considered to have a fair account of dynamic loss. However, it is always desirable to adopt fibre-reinforced plastic (FRP) based coil former, support structure, *etc.* in order to minimize its eddy loss contribution.

However, cable specification should be made carefully in the design stage so that the dynamic load could be minimized to an acceptable value. Contribution of vapour cooled current leads is dominant in static load, which could be reduced further using HTS based current leads. Higher the power rating of SMES coil, it is important to note that apart from increase in dynamic loss, operating current of SMES increases and the conductor winding volume as well as inductance of coil reduces as shown in Figure 5.4.

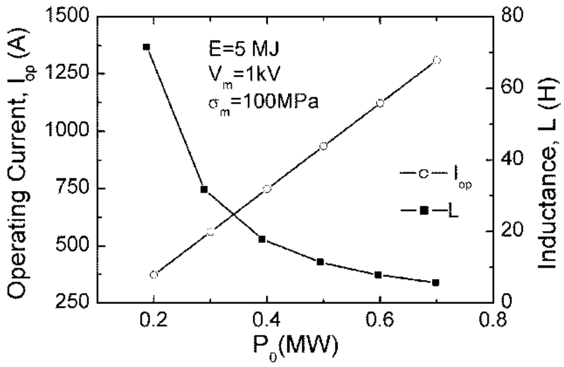

Figure 5.4: Variation of operating current with rated powers.

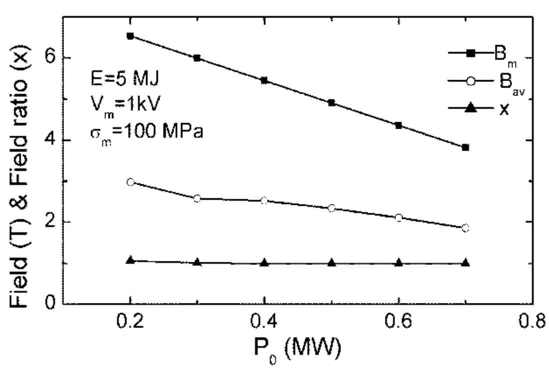

Figure 5.5: Magnetic field and peak field to center field ratio (*x*) with various rated powers.

It is interesting to note that the both the peak and average magnetic field in the coil decreases with increase of power rating of the coil as observed from Figure 5.5. This is for obvious reason that loss could be reduced if the field transient is also lowered, and therefore, both peak magnetic field and average magnetic field on coil reduces. Higher the allowable winding hoop stress is advantageous in the sense that it reduces the overall loss especially dynamic loss drastically and the required conductor volume as well, which is observed in Figure 5.6. Indeed, SMES coil of higher stored energy level and rating are made to operate at higher current and hoop stresses since these two criteria reduce the total loss as well as coil volume.

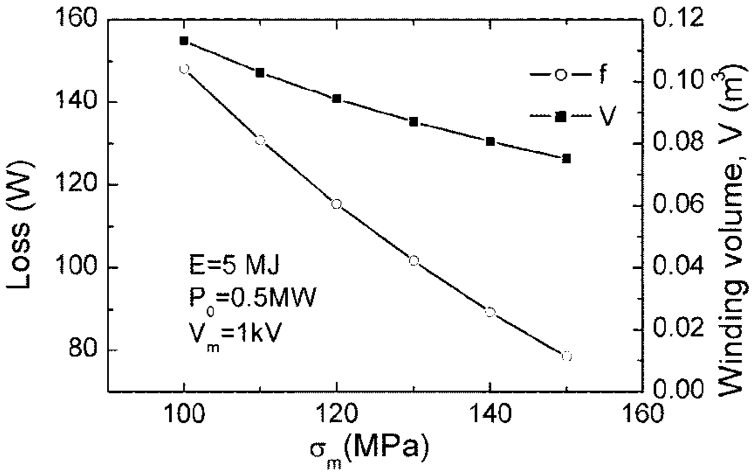

Figure 5.6: Effect of allowable hoop stress on refrigeration loss and winding volume.

Design results with different allowable hoop stress are as shown in Table 5.2.

Table 5.2: Design results of 5 MJ/0.5 MW solenoid-type SMES coil for various peak hoop stress in winding.

$\sigma_m(MPa)$	100	110	120	130	140	150
$f(W)$	148.3	130.8	115.4	101.7	89.3	78.5
$f_{dy}(W)$	146.0	128.5	113.3	99.6	87.1	76.4
$f_s(W)$	2.3	2.3	2.2	2.1	2.1	2.1
$a(m)$	0.192	0.214	0.237	0.26	0.285	0.312
α	1.107	1.1	1.087	1.08	1.074	1.07
β	11.33	8.3	6.2	4.7	3.58	2.75
$B_m(T)$	4.9	4.9	4.9	4.9	4.9	4.9
$B_{av}(T)$	2.34	2.30	2.26	2.2	2.14	2.08
x	1.0	1.0	1.0	1.0	1.0	1.0
$I_{op}(A)$	935	935	935	935	935	935
$V_m(kV)$	1.0	1.0	1.0	1.0	1.0	1.0

Coil parameters such as inner radius (a) increases gradually whereas coil height parameter (β) reduces with increase in allowable hoop stress. For a given stored energy and power rating of SMES coil, it is always advantageous to operate it at higher operating current level or in otherwise at lower allowable voltage (V_m) as shown in Figure 5.7 since the dynamic loss reduces considerably in this situation. However, higher operating current increases steady state load through the current leads.

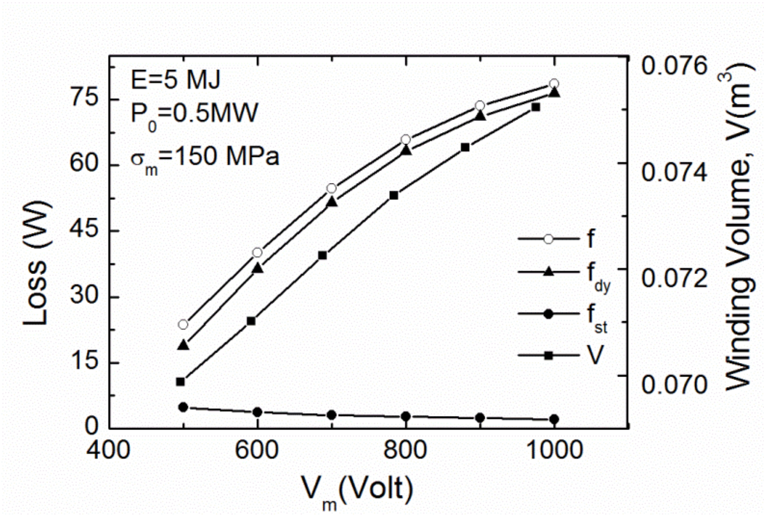

Figure 5.7: Variation of refrigeration loss and winding volume with allowable discharge voltages.

Though we have taken operating current safety margin (ζ) into consideration, however, detail quench protection scenario needs to be analysed and implemented so that the coil, cryostat, *etc.* becomes safe during any quench-like event or vacuum failure in cryostat annular wall, *etc.* In the process of optimization, loss due to axial field transients is only considered since radial field transient over the winding volume is significantly lower with respect to axial field transient. However, loss contribution due to radial field transients also should be considered for budgeting total heat load into the cryostat.

5.4 Refrigeration Load on Intermediate Thermal Shield (60–80 K)

The intermediate thermal shield around the helium vessel also experiences both dynamic and static heat load. The thermal shield is connected to the first stage of cryo-refrigerator and it should have a good thermal conductivity and mechanical rigidity to weight ratio. In general materials like copper or aluminum alloy are commonly used and needs to be cooled by the first stage of the 4 K cryo-refrigerator. Apart from steady state radiative load, rapid charge or discharge of SMES magnet causes induced eddy current in the thermal shield, and therefore, causes dynamic refrigeration load as well. An estimate of refrigeration load on the design of 5 MJ/0.5 MW/150 MPa SMES is worked out in the following section to observe the feasibly of using first stage of the commercially available two stage 4 K cryo-coolers.

5.4.1 Steady-State Load

The thermal shield covered with multilayer super-insulation blanket made of 30 layers (layer density of 15/cm typically) in a good vacuum (~10^{-5} mbar or better) experiences effective heat flux from the surface of vacuum vessel at 300 K, $q_{ths} \sim 1.0\ W\,m^{-2}$. Considering the thermal shield closely conforms to the helium vessel with a radial gap in between, static heat load, g_{sta} (in W) on intermediate thermal shield in terms of both radiative and gas conduction may be written as

$$g_{sta}(\alpha,\beta,a) = q_{ths}(2\pi\, r_{ths}\, l_{ths} + 2\pi\, r_{ths}^2) \tag{5.23}$$

$$\left.\begin{aligned} r_{ths}(\alpha,a) &= \alpha\, a + x_1 + x_2 \\ l_{ths}(\beta,a) &= 2\beta\, a + 2(x_1 + x_2) \end{aligned}\right\} \tag{5.24}$$

Where x_2 is assumed to be a uniform distance of thermal shield from helium vessel both in radial and axial direction of the SMES coil; r_{ths} and l_{ths} represents the radius and length respectively of the thermal shield. Typical values considered for the present analysis are x_1=0.015 m, and x_2=0.02 m. For example, in case of 5MJ/0.5 MW/150 MPa design, the surface heat input estimated on the thermal shield is around 5.0 W at 77 K.

5.4.2 Dynamic Load

Magnetic field transients during discharging and subsequent charging operation of SMES coil causes induced currents in thermal shields. The problem is particularly important since the thermal shield is fabricated from a material with high electrical conductivity (typically aluminum or copper).

5.4.2.1 Eddy loss on the flat faces of thermal shield

The flat surface of thermal shield may be considered as thin disk. From Faradays law, for a thin disk of radius r_{ths} and thickness δ (with $r_{ths} >> \delta$), one can have analytic form of eddy loss considering homogeneous, isotropic and time invariant media, $g_{dy,1}$ (W) due to uniform average axial magnetic field transients (during discharge of SMES coil) of $\dot{B}_{av}$ over the flat surfaces as

$$g_{dy,1}(\alpha,\beta,a,t) = \frac{r_{ths}^2}{8\rho_{ths}} \dot{B}_{av}^2(z)\Big|_{z=l_{ths}/2} (2\times\pi\, r_{ths}^2\, \delta)\left(1-e^{-t/\tau_m}\right)^2 \tag{5.25}$$

Where, ρ_{ths} (Ω m) is the resistivity of thermal shield at its maintained temperature. For example, considering the shield material to be made of copper, $\rho_{ths}(77K) \sim 2.9\times 10^{-9}\,\Omega m$. For the purpose of preliminary estimation, one can consider the shield thickness, δ=1.0 mm, though it should be determined through electromagnetic force and stress consideration. The time variation of average flux density, $\dot{B}_{av}$ (T/s) is calculated over the enclosed area of thermal shield. The time constant ($\tau_{m1} = \frac{\mu}{\rho_{ths}} r_{ths}\delta$) associated with the magnetic diffusion is ~80 ms for this particular geometric configuration, which is negligibly small with respect to the discharge or carry over period of 7s.

5.4.2.2 Eddy loss on curved surface

Following Faradays law again, if we consider an average axial magnetic field, $B_{av}(z)$ over the bore of thermal shield, eddy loss, $g_{dy,2}$ (in W) during discharge operation of SMES may be derived for the curved surface as

$$g_{dy,2}(\alpha,\beta,a,t)=\frac{\pi}{2\rho_{ths}}r_{ths}^{3}\delta\left(\int_{-l_{ths}/2}^{l_{ths}/2}\dot{B}_{av}^{2}(z)\,dz\right)\left(1-e^{-t/\tau_{m2}}\right)^{2} \tag{5.26}$$

The time constant (τ_{m2}) associated with the magnetic diffusion for the shell structure, which is of same order as τ_{m1}.

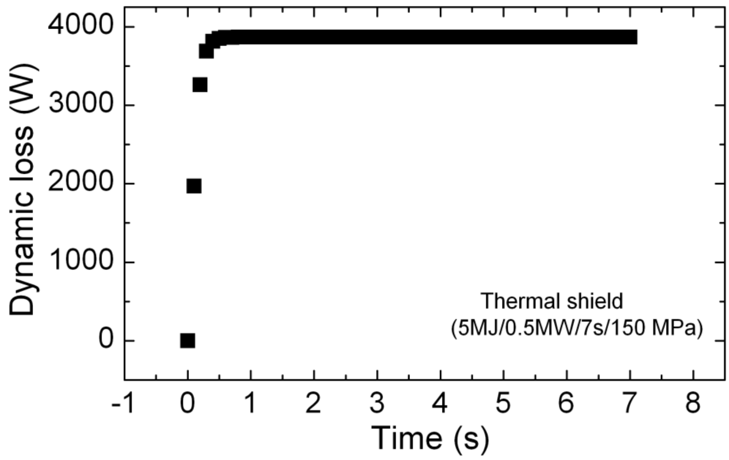

Figure 5.8: Dynamic load on intermediate thermal shield at 77K for 5 MJ/0.5 MW/150 MPa SMES coil.

The time dependent overall dynamic refrigeration load on the intermediate thermal shield of 5MJ/0.5MW/7s system is as shown in Figure 5.8. The overall dynamic load is found to be around 3.9 kW at 77 K. Though this value is quiet high, however the temperature rise of the shield over the discharge period is found to be insignificant (~ 3K) under adiabatic approximation. Further, planning of using four numbers of two-stage commercially available cryo-refrigerators typically provide 240 W at 77 K in its first stage without disturbing the performance of second stage at 4.2 K. Therefore, within two minutes of operation, temperature stabilizes again to the base operational temperature of 77K.

5.5 Summary and Discussion

A comprehensive design optimization formulation of solenoid-type SMES coil has been developed that minimizes overall refrigeration cost in terms of static and dynamic heat load into the magnet cryostat. For any given superconducting cable with known critical characteristics (*J-B)* and design constraints, geometrical parameters as well as operating point of the SMES coil may be determined considering the in-built safety margin using our optimisation approach. The uniqueness of the design optimisation is that loss and all other operating parameters are represented in terms of coil geometric parameters analytically and may in general be used for developing SMES coil with any arbitrary energy storage capacity and power rating. Conductor design for SMES application plays a vital role in reducing transient load into the cryostat.

CHAPTER 6

PARETO-OPTIMAL DESIGN OF SECTOR TOROIDAL SMES COIL WITH RUTHERFORD-TYPE CABLE

A multiobjective optimization design approach for sectored toroidal superconducting magnetic energy storage coil has been developed considering the practical engineering constraints. The objectives include the minimization of necessary superconductor length and overall torus size, which determines a significant part of cost towards realization of SMES. The best trade-off between the necessary conductor length for winding and magnet overall size is achieved in the Pareto-optimal solutions. The final choice among Pareto optimal configurations can be done in relation to other issues such as AC loss during transient operation, stray magnetic field at outside the coil assembly, available discharge period, *etc.*, which is not considered in the optimization process.

6.1 Design Formulation

The sectored toroidal proposed SMES unit is composed of a finite number of sectors or elemental solenoid coils arranged in a toroidal fashion as shown in Figure 6.1 and are series-interconnected. Geometry of the sectored toroidal magnet is completely described by three design variables namely, major radius, r_0, geometry dependent parameters, α, and β for a given inter-sector coil spacing, d. For the purpose of present study, the sector coil have been thought of solenoid-type because of manufacturing easiness though the best optimized shape would be Shafranov or D type coil [61] as far as minimal conductor length for a given stored energy is concerned. In optimization process, the finite element analysis (FEA) is generally used as a magnetic field and electromagnetic stress analysis method. However, while the optimization design is based on FEA for 3D problem, the long computation time due to many design variables, and iterative calculations are extremely troublesome. Therefore, the problem is described analytically to understand and develop the initial design with a reasonably acceptable accuracy.

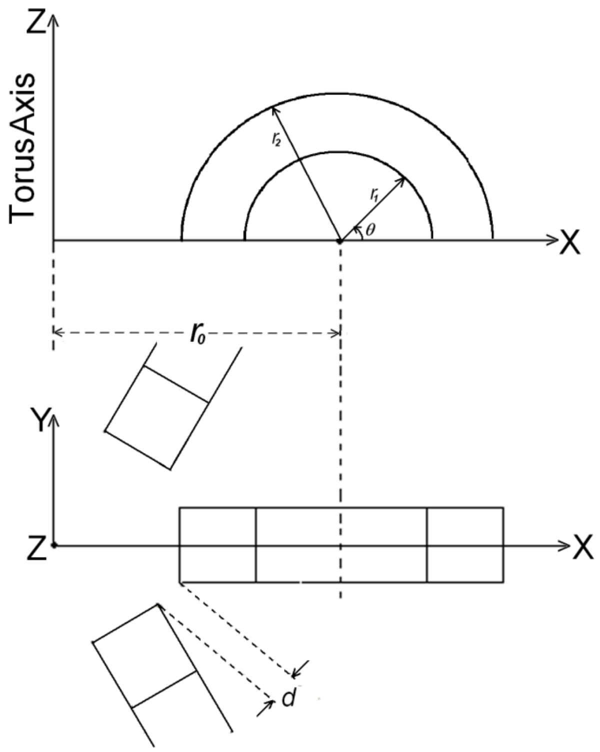

Figure 6.1: Schematic of toroidal coil arrangement.

6.1.1 The Peak Magnetic Field and Stored Energy

The central magnetic field, B_0 (at r_0) for N_s numbers of solenoid-type sector coils arranged in a toroidal fashion may be written as,

$$B_0(r_0,\alpha,\beta) = \frac{\mu_0 N_s n_t \, J_{op} A_C}{2\pi \, r_0} \tag{6.1}$$

where, $\mu_0 = 4\pi \times 10^{-7} V s A^{-1} m^{-1}$ is the permeability of free space. Considering the field variation across the winding is inversely proportional to the torus radius, the peak magnetic flux density, B_m, at the inner turn of sector coil in the region inside the toroidal magnet, which determines the operating point of the conductor and temperature margin as well, may be expressed as

$$B_m(r_0, \alpha, \beta) = B_0 \frac{r_0}{r_0 - r_c(r_{0,}\alpha, \beta)} \tag{6.2}$$

Where, total number of turns, $n_t(r_0, \alpha, \beta) = n_r(r_0, \alpha, \beta).n_y(r_0, \beta)$ depends on the radial thickness and coil height of each sector coil and may be written as

$$\begin{aligned} n_r &= \lambda_r (r_2 - r_1)/a \\ n_y &= \lambda_y \; h/b \end{aligned} \tag{6.3}$$

The length of each sector coil is given by

$$h = h(r_0, \beta) = \frac{2\pi\, r_0 (1-\beta)}{N_s} - d \tag{6.4}$$

The stored energy, *E*, of a toroidal magnet array can be expressed in a form which depends on B_m, r_0, α and β as [83],

$$E(r_0, \alpha, \beta) = 1.05 \times 1.57 \times 10^8 B_m^2(r_0, \alpha, \beta)\; r_0^3 \;\; f_E(r_0, \alpha, \beta) \tag{6.5}$$

where, $f_E(r_0, \alpha, \beta) = ((A(r_0, \alpha, \beta) - 1)/A(r_0, \alpha, \beta))^2.(1 - \sqrt{1 - (1/A(r_0, \alpha, \beta))^2})$

The coil aspect ratio is given as, $A(r_0, \alpha, \beta) = \dfrac{r_c(r_0, \alpha, \beta)}{r_0}$

6.1.2 Magnetic Field Dependence on Operating Current Density

Because of the requirement of low loss operation of the coil, cost of material, *etc.*, problem considered in this study assumes to use niobium-titanium alloy based Rutherford-type cable, which is considered to be suitable for medium size SMES system. The use of

Rutherford cable provides high current density while maintaining performance redundancy with more number of strands. The cable also needs to be adequately insulated to ensure that no voltage breakdown occurs during normal charging/discharging operation of SMES coil or during quench. The coil is assumed to be epoxy impregnated and liquid helium bath cooled at 4.2 K. The operating current density (J_{op}) is determined in terms of coil peak magnetic field (B_m) from the critical characteristics (Fig. 6.2) of the superconducting cable (i.e. $I_C - B$) as follows:

$$J_{op}(B_m) = J_C(B_m)\, \lambda_r \lambda_y \; (1-\zeta) \tag{6.6}$$

For the purpose of present study, the space or filling factor is assumed to be 0.9 in both radial and axial direction, i.e. $\lambda_r = \lambda_y$ =0.9. However, in general depending on the cooling and winding scheme, insulation, *etc.* filling factors need to be determined appropriately. The operational or safety margin factor (ζ) is assumed to be 0.3 along the load line in the present study. A 30% margin of operating current corresponds to a temperature margin of 0.55 K over the operating temperature of 4.4 K. The operational margin ensures that the superconductor will not quench during normal operation.

The variation of critical characteristics of the cable may be written in the following form

$$J_{op}(r_0, \alpha, \beta) = J_{op}(B_m) = \frac{p}{q + \dfrac{B_m}{J_{op}(B_m)}} \tag{6.7}$$

Here, the parameter p and q depend on the real characteristics of the superconductor and is fitted from J_{op} against B_m/J_{op} plot as shown in Figure 6.3. Substituting from eq. (6.2), the operating or transport current density may be expressed as,

$$J_{op}(r_0, \alpha, \beta) = \frac{p}{q + \dfrac{k_1 n_t(r_0, \alpha, \beta)}{r_0(1-\alpha)} . f_m} \tag{6.8}$$

where, $k_1 = \frac{\mu_0}{2\pi} N_S A_C$. The fitted parameters are p =9.0078 T and q = 1.319×10^{-8} TA^{-1}m^{-2} for the superconducting cable considered as in Table 6.1.

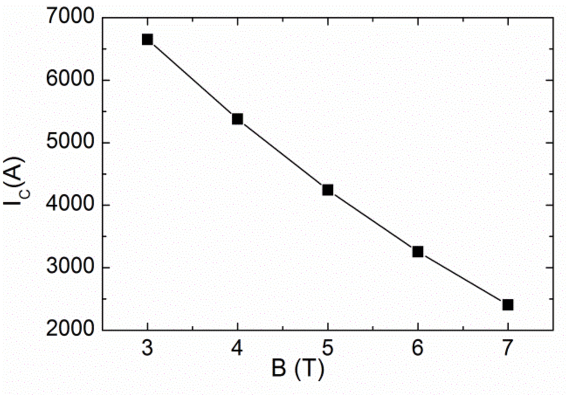

Figure 6.2: Critical characteristics of the Rutherford cable.

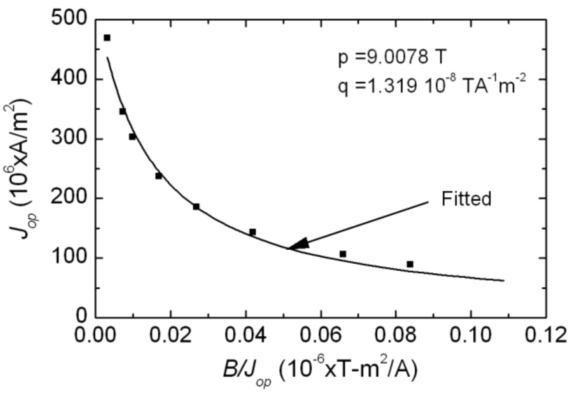

Figure 6.3: Operating current density fitted with B/J for sectored toroidal SMES.

6.1.3 Structural Considerations

An important design criteria is the maximum mechanical stress produced by the Lorentz forces, which has to be below the critical stress value that can be sustained by the materials composing of coil windings. The interaction of toroidal magnetic field and coil current results in a large radial forces acting in the plane of each sector coil, similar to a ring with internal pressure. Since the toroidal magnetic field is approximately inversely proportional to the radial distance from magnet axis, in normal operating condition, the magnetic field on the sector coils is non-uniform and asymmetric with respect to coil azimuth, θ. This results a net attractive force on the sector coil towards the centre of the torus and must be compensated by suitable support structure. Evaluation of stress in a sectored toroidal magnet winding with detailed and elaborate scheme of support structure is complex in nature requiring three-dimensional finite element analysis (FEA). However, with the assumption of a uniform field distribution around the sector coil azimuth, one can have a first approximation of stress, before proceeding to accurate and more detailed calculation with FEA. With the context of present optimization study, circumferential or hoop stress due to electromagnetic force is considered since it primarily dictates the effective or von-Mises stress at the winding. The stress is maximum at the inner part of the winding at $r=r_0-r_1$, where the bending moment and associated shear stress also have the maximum value. If any failure occurs, it could be in this region of the coil. Considering the coils are isotropic and homogenous with equivalent elastic modulus of constituent materials, the expression for maximum hoop stress (σ_c) at the winding of sector coil for the first approximation may be written [84]

$$\sigma_c = \frac{p_i r_1}{r_2 - r_1} . \frac{\ln(r_2 / r_1)}{r_2 / r_1 - 1} = p_i \frac{\alpha}{\beta - \alpha} . \frac{\ln(\beta / \alpha)}{\beta / \alpha - 1} \tag{6.9}$$

The radial force in terms of coil peak field exerted for unit area of sector coil is essentially same as the equivalent internal pressure, p_i. The equivalent internal pressure at the mid-plane of sector coil is written as

$$p_i = i_{op} B_m = \frac{n_r n_y J_{op} A_C}{h} B_m \tag{6.10}$$

Where, i_{op} is the total current in the unit axial length of the sector coil. In this paper, the cryogenic design regarding thermal stresses is not taken into account to simplify the design. However, thermal stress, winding pretension, *etc.* in presence of detailed support structure should be considered with FEA for the more advanced design.

6.2 Multiobjective Optimization Approach

The multi-objective optimization approach deals with finding optimal solution of a set of several objectives. The objectives often conflicts each other so that improving one objective will deteriorate other objective function or vice versa. Different researchers used different approaches of multi-objective evolution algorithm, each one having its own merits and demerits. We chose to use the classical weighted-sum approach for multi-objective solution, which is to assign a weighting coefficient w_i, to each objective function and summed so that the problem maps to a single scalar objective function (*OF*). The merit of this method is that it is very effective and easy to implement. The goal of optimal design is to find the Pareto solutions corresponding to the objective function of necessary conductor length (L) and magnet size in terms of major radius (r_0) of the torus. The objective functions, in turn, determine a major part of overall cost of the sectored toroidal magnet system. The length of superconducting cable required for winding is given by

$$L = N_s.\pi\, r_0(\beta+\alpha)\, n_t(r_0,\alpha,\beta) \tag{6.11}$$

The optimization problem based on weighted-sum method can be mathematically represented as follows:

$$\text{Minimize } OF = w_1 r_0 + w_2\, L(r_0,\alpha,\beta) \tag{6.12a}$$

Subjects to the constraints

$$\begin{pmatrix} E(r_0,\alpha,\beta) = E_i \pm \delta E_i \\ \sigma_c(r_0,\alpha,\beta) \le \sigma_a \\ d = d_0 \\ N = N_S \\ 0.05 \le \alpha < \beta \le 0.95 \\ 0.1 \le r_0 \le 2.0 \end{pmatrix} \tag{6.12b}$$

Where the weighting coefficients, $\sum_i w_i = 1$ and it ran over the interval 0-1 with a specific step size. Considering the electromagnetic and mechanical characteristics of the SMES, the design parameters and their bounds are given in (6.12b). Evolution algorithms are a natural choice for solving multi-objective type optimization problems because of their population based nature. Different set of weight parameters (w_i) are used to find set of multiple compromise or trade off solutions popularly known as Pareto optimal solutions [85]. The set of all feasible Pareto optimal objective vectors is referred to as Pareto optimal front, *PF*.

The specifications of the magnet are set as follows:

i) The required stored energy, (E_i = 4.5 MJ) with acceptable tolerance, δE_i (0.1% considered).

ii) Circumferential stress in sectored coil to be within a maximum allowable limit, σ_a.

iii) Numbers of elemental coils (N_s) to be chosen in such a way that stray magnetic field outside the coil assembly follows the safety guidelines of 0.5 mT or lower.

iv) Number of winding turns (n_r) and layers (n_y) are considered to be integer.

v) There must be small inter-sector gap (d) for implementation of suitable support structure, access to the useful volume and ease of manufacture. In the present study, d=50 mm is assumed from practical consideration. The support structure keeps the sector coil in position under strong electro-magnetic force.

6.3 Design Results and Discussions

6.3.1 Dependence of Magnet Size and Conductor Length

The typical Pareto optimal fronts for N_s= 6, 8, 10 and 12 sectored toroidal system are demonstrated in Figure 6.4. The result shows that the required conductor length depends strongly on magnet size in terms of r_0. Further, for a given size (r_0) of magnet, higher the number of sectors increases necessary conductor length only marginally. It is important to observe that for the given set of design constraints there exists a minimum r_0 below which feasible solution does not exist.

Higher the allowable stress in the winding, however, reduces the conductor requirement considerably as shown in Figure 6.5. This is due to the fact that increasing allowable hoop stress in the winding corresponds to increased operating current density too and therefore requiring reduced number of winding turns.

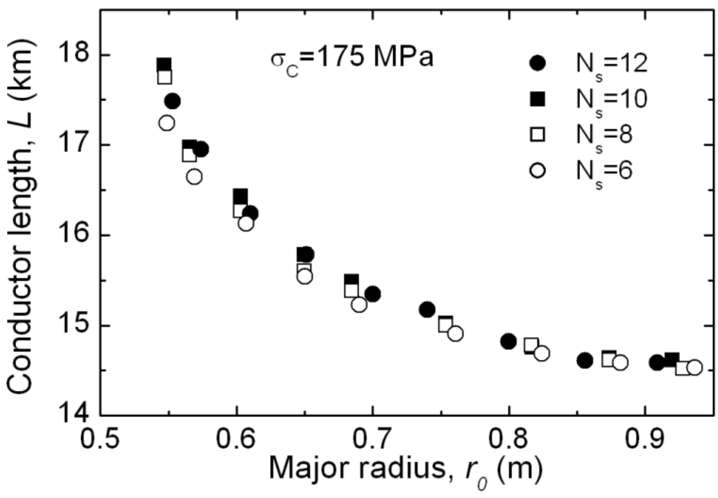

Figure 6.4: Pareto optimal front of two objectives with σ_c=175 MPa for 4.5 MJ sectored toroidal SMES coil.

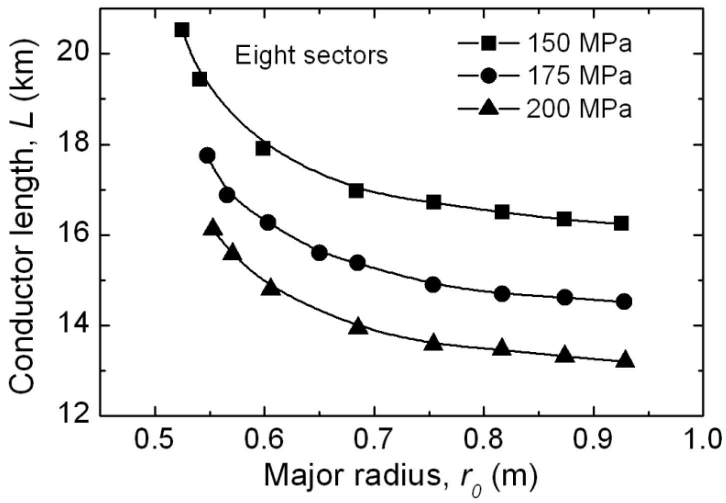

Figure 6.5: Pareto-optimal front for eight-sector toroidal system of 4.5 MJ SMES with different peak circumferential stress, $\sigma_{c.}$

The compact design of SMES coil also implies more stored energy density, and therefore more peak magnetic field too as observed in Figure 6.6. However, higher peak magnetic field reduces the temperature margin during operation. In addition, higher peak magnetic field at the conductor reduces the operating current density too maintaining the required stability margin (ζ) over critical current density. Therefore, the necessary conductor length increases when the peak magnetic field at the conductor is increased or in turn, for the compact magnet size. It is also important to observe that lower the toroid major radius, coil parameters α and β both increases as shown in Figure 6.7.

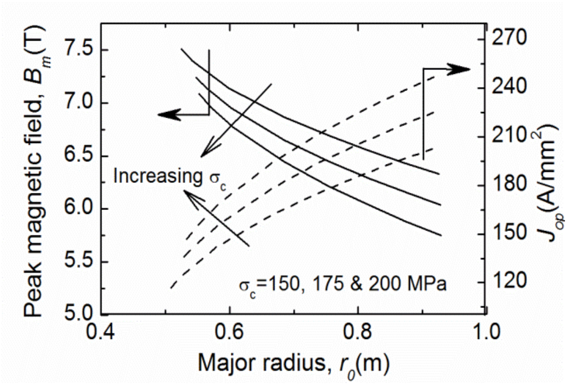

Figure 6.6: The operating current and peak magnetic field of eight-sector system with different major radii.

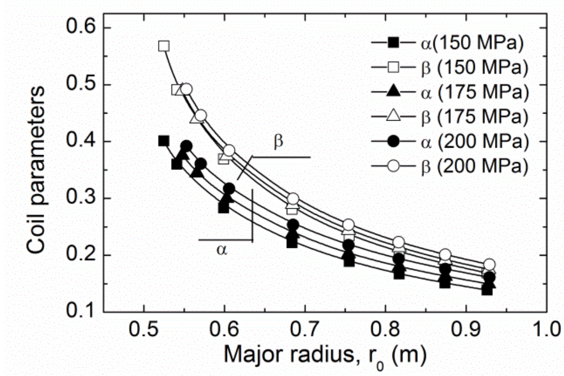

Figure 6.7: Coil parameters in Pareto-optimal solutions of eight-sector system for different peak hoop stress.

The representative Pareto-optimal set for the eight-sector assembly at σ_c=175 MPa is shown in Table 6.1.

Table 6.1: Representative Pareto solutions for eight sector 4.5 MJ/1MW SMES coil (Ns=8 and σ_c=175 MPa).

No. of scenarios	1	2	3	4	5	6	7
$r_0(m)$	0.874	0.754	0.685	0.65	0.603	0.566	0.548
α	0.163	0.203	0.238	0.26	0.3	0.345	0.376
β	0.192	0.244	0.289	0.32	0.375	0.44	0.489
Iop(A)	1463.8	1313	1208	1148	1055	965	907.6
Winding turns, n_t	1870	1785	1691	1638	1584	1508	1485
B_m(T)	6.16	6.4	6.6	6.77	6.9	7.1	7.24
L (km)	14.62	14.89	15.38	15.54	16.27	16.88	17.75
5G line from torus center(m)	2.17	2.0	1.91	1.89	1.8	1.78	1.77
E(MJ)	4.48	4.51	4.47	4.51	4.49	4.49	4.51

The torus surface area which primarily determines the sizing of liquid helium vessel and therefore, the radiative steady state heat in-leak into the liquid helium system at 4.2 K shows minimum value for Pareto solutions corresponding to r_0 =0.62-0.67 m as shown in Figure 6.8. The inter-sector gap (d) has a weak dependence on the optimal parameters. Higher the inter-sector spacing, stray magnetic field outside increases marginally.

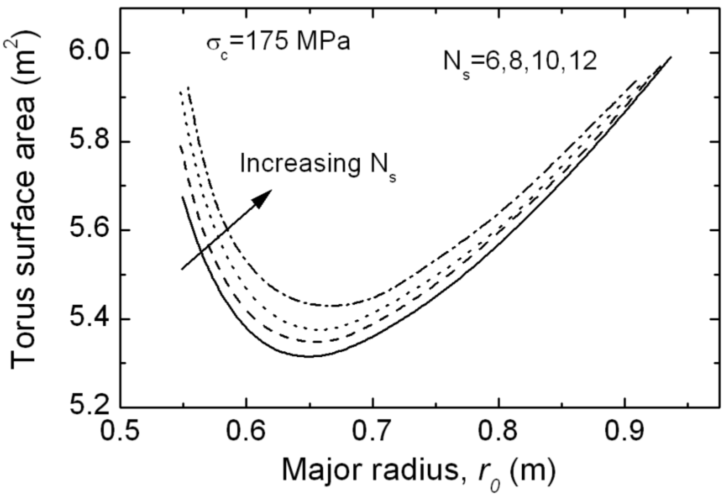

Figure 6.8: Variation of torus or cold mass surface area with major radius.

6.3.2 Stray Field Consideration

A further objective of the design is to shield the stray magnetic field within a specified region outside the coils down to 0.5 mT level, which is approximately the average earth field. Suitable numbers of sector coils may be chosen from the allowable stray magnetic field criteria outside the magnet system.

The iso-gauss contour line corresponding to 0.5 mT at equatorial plane (i.e. Z=0 plane) outside the cryostat is computed for the set of Pareto solutions using commercially available general purpose multi-physics finite element analysis (FEA) code ANSYS and compared in Figure 6.9. It is observed that higher the number of sectors, stray field outside the cryostat reduces further as expected. However, higher number of sectors requires more numbers of inter-sector superconducting joints as well. Therefore, too many sectors may be avoided without much additional gain. Further, operating current must be increased with increase of the sector coils because the inductance of the magnet decreases with the increase of sector numbers.

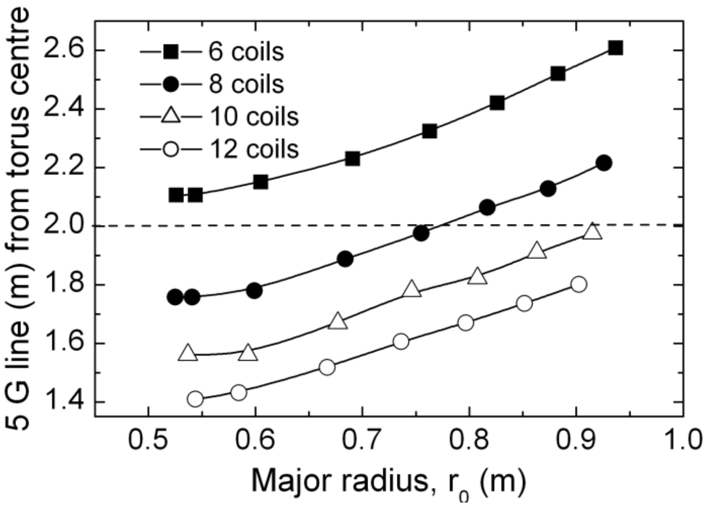

Figure 6.9: Maximum distance of 5 G contour line from torus center at equatorial plane (Z=0) for different Pareto solutions.

The 0.5 mT contour for the optimal solution corresponding to eight-sectors and at r_0=0.65 m is as shown in Figure 6.10.

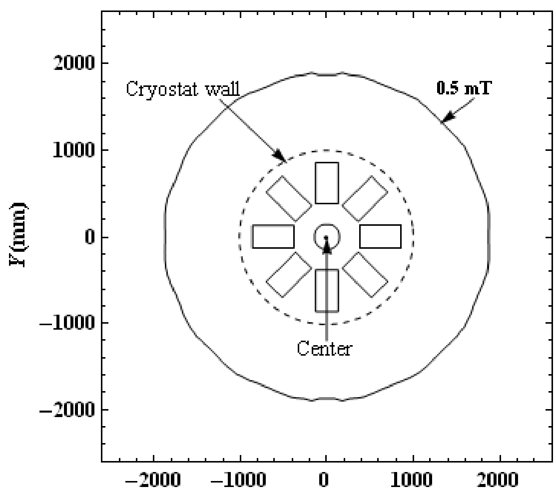

Figure 6.10: 0.5 mT contour at the equatorial plane (Z=0) for the Pareto solution corresponding to r_0=0.65 m and N_s=8.

The Pareto-solution corresponding to r_0=0.65 m and σ_c=175 MPa for different number of sectors is given in Table 6.2. The Pareto-optimal coil configuration corresponding to N_s=8 and 10 are shown in Figure 6.11 (a) and Figure 6.11 (b) respectively.

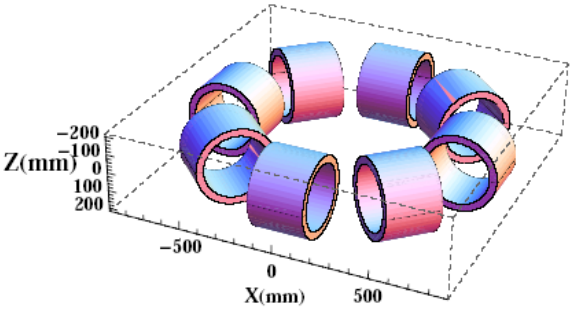

Figure 6.11(a): Configuration of eight-sector coil at r_0=0.65 m and σ_c=175 MPa.

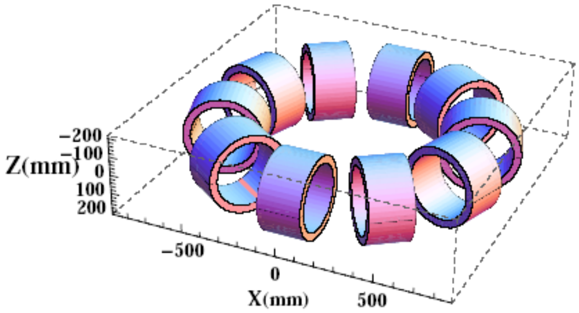

Figure 6.11(b): Configuration of ten-sector coil at r_0=0.65 m and σ_c=175 MPa.

Table 6.2: Pareto solutions of 4.5 MJ/1MW SMES coil corresponding to r_0 = 0.65 m and σ_c=175 MPa.

Nos. of sectors(N_S)	6	8	10	12
r_0 (*m*)	0.65	0.65	0.65	0.65
α	0.26	0.26	0.26	0.26
β	0.318	0.32	0.321	0.324
h (*m*)	0.415	0.289	0.222	0.178
Iop(A)	1142	1148	1156.4	1164.5
Winding turns, n_t	2184	1638	1320	1104
B_m(T)	6.78	6.77	6.75	6.74
L (km)	15.5	15.54	15.68	15.79
5G line from torus center (m)	2.22	1.87	1.65	1.51
E(MJ)	4.51	4.51	4.46	4.48

6.3.3 AC Loss Consideration

We would further investigate the dynamic or AC losses for the proposed conductor for various Pareto solutions corresponding to eight-sector coil as case study since the SMES coil operates dynamically in the power system. Assuming a peak power P_0 to the load over a discharge period of t_s, the stored energy in the coil is

$$E(t) = E_i - P_0 t \qquad \text{(for } t < t_s\text{)} \tag{6.11}$$

The coil current $I(t)$ at any instant of time (t) during discharge become

$$I(t) = I_{op}(0)\sqrt{1-\eta\frac{t}{t_s}} = \frac{P_0}{V_i}\sqrt{1-\eta\frac{t}{t_s}} \tag{6.12}$$

Where, $\eta = P_0 t_s / E_i$ is known as depth of discharge, V_i is the voltage across SMES coil during initiation of discharge at t=0. The average discharge rate of current while mitigating the peak power P_0 to the load is written as,

$$(dI/dt)_{avg} = \frac{1}{t_s}\int_0^{t_s} I(t)dt \tag{6.13}$$

During discharge the peak magnetic field decreases allowing critical current density to increase. The power conditioning system (PCS) that consists of a DC-DC chopper and a three phase voltage source converter (VSC) is the interface between SMES coil and power system. The desired charge and discharge requirement is achieved controlling the duty cycle (D) of chopper circuit. The voltage relationship across SMES coil (V_{SMES}) and voltage across DC link capacitor (V_{DC}) of chopper circuit is related by

$$V_{SMES} = (1-2D)V_{DC} \tag{6.14}$$

The available maximum discharge or carry over period may be written in terms of DC link voltage of chopper as

$$t_s = \frac{E_i}{P_0}\left(1-\left(\frac{V_i}{V_{DC}}\right)^2\right) \tag{6.15}$$

The available discharge period for the Pareto solutions of eight sector coil with a realistic assumed DC link voltage of 1.5 kV is as shown in Figure 6.12. It is observed that compact the magnet size (solutions with lower r_0) available energy from SMES or in turn, discharge period reduces too.

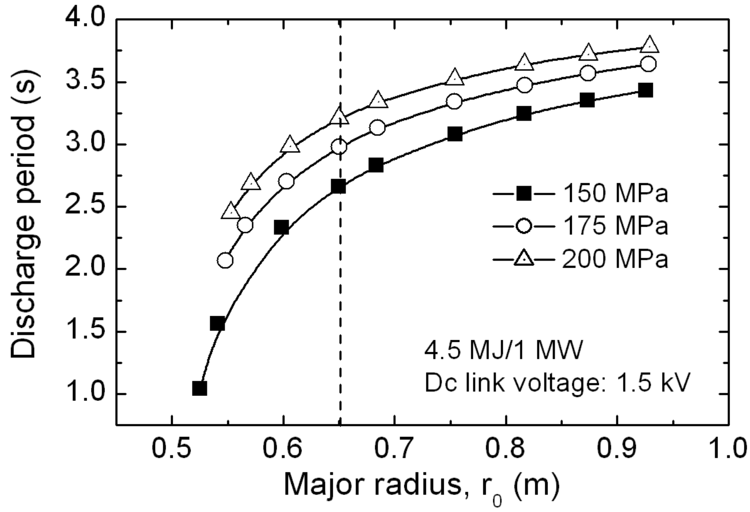

Figure 6.12: Maximum available discharge period for N_s=8 for 4.5 MJ/1MW/2s system.

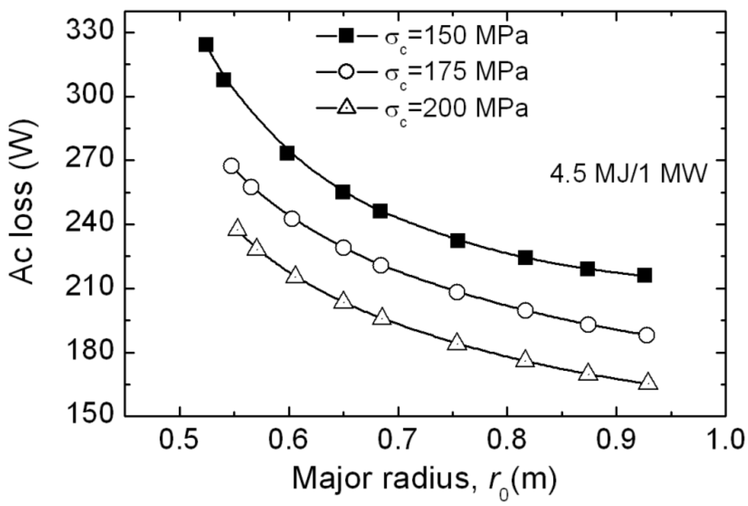

Figure 6.13: Average AC loss estimated during discharge operation for N_s=8.

When SMES is discharged at a constant power output, the magnet current drops decreasing the magnetic field in winding and increasing the critical current density. The changing current produces losses in superconductor primarily composed of eddy current flowing among strands or inter-strand losses and hysteresis loss in the filaments. Each winding turn in sector coil is divided into number of small sections and the magnetic field of each section is calculated. Summing over the contribution from different layers and turns of winding volume with the consideration of local magnetic field distribution, AC loss from superconductor winding volume during the discharge operation is evaluated.

Table 6.3: Pareto solutions for 4.5 MJ/1MW SMES with eight sector coil system and of major radius of 0.65 m.

Allowable hoop stress (MPa)	σ_c=150	σ_c=175	σ_c=200
α	0.243	0.26	0.28
β	0.31	0.32	0.333
h(m)	0.296	0.289	0.289
Iop(A)	1045	1148	1247
Winding turns, n_t	1920	1638	1435
B_m(T)	6.97	6.77	6.58
L (km)	17.37	15.54	14.3
5G line from torus center (m)	1.85	1.87	1.88
AC loss, q_{loss} *(W)*	255	229	203
**Duty cycle (%) over discharge period*	0.18-0.0	0.21-0.0	0.23-0.0
Discharge period, t_s *(s)*	2.6	2.9	3.2
E(MJ)	4.47	4.51	4.52

**DC link voltage of* V_{dc}*= 1.5 kV is considered.*

Since both the required conductor length and peak magnetic field reduces with higher the major radius, AC loss follows the same trend. Further, higher the allowable stress in winding, the AC loss also reduces because of both reduced magnetic field in the winding as well as lower conductor length required as shown in Figure 6.13.

Summarizing the design aspects such as available discharge period, stray magnetic field extension outside coil system, and torus surface area, it seems to be reasonable to select Pareto solutions corresponding to r_0 ~ 0.62-0.67 for the 4.5 MJ/1MW system. The eight-sector based feasible Pareto solution of the 4.5MJ/ 1MW system corresponding to r_0 = 0.65 m is as shown in Table 6.3.

6.4 Results Validation

To check the validity of the optimal scenarios illustrated by Pareto front for different sectors, electromagnetic simulation to evaluate magnetic field, stored energy and hoop stress is carried out using ANSYS.

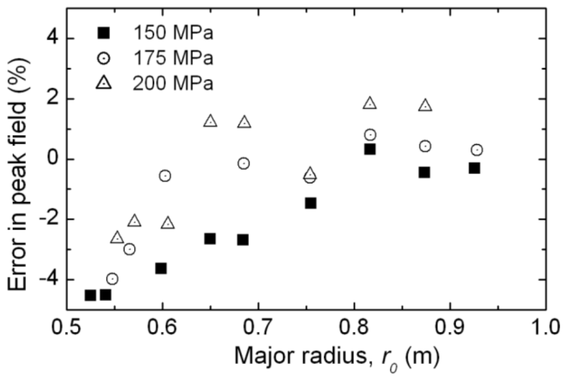

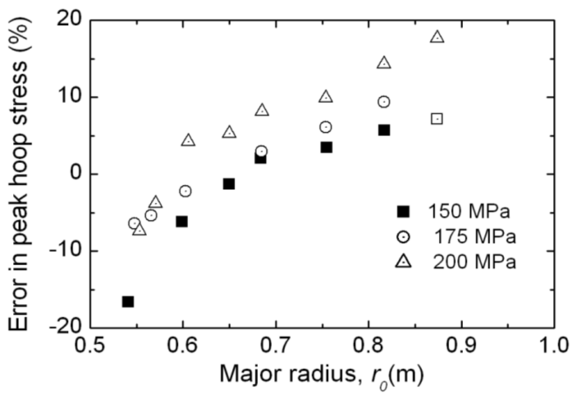

Figure 6.14(a): Error on peak magnetic field for Pareto solutions corresponding to N_s=8.

Figure 6.14(b): Error on peak hoop stress for Pareto solutions corresponding to N_s=8.

For different Pareto solutions, the peak magnetic field observed in the winding has a maximum error compared to the value simulated with FEA by 5% as shown in Figure 6.14 (a). The FEA analysis allows a detailed quantitative evaluation of the stresses under electro-magnetic forces. The error in peak hoop stress in winding obtained from Pareto optimal results with respect to FEA calculation is found to be within 20% as shown in Figure 6.14(b). The inaccuracy of hoop stress estimation from the simple analytical calculation during the process of optimization may be well-accepted to carry out initial design of the system. The FEA analysis also reveals that the peak von-Mises stress in the winding, which determines the structural integrity of ductile materials, is at most 15% more than the peak hoop stress over the Pareto-front. Therefore, sufficient margin over allowable hoop stress needs to be kept so that the peak von-Misses stress is well within the allowable limit. Finally, the error estimation on stored energy from Pareto-solutions with respect to FEA is found to be within 3% as illustrated in Figure 6.14(c).

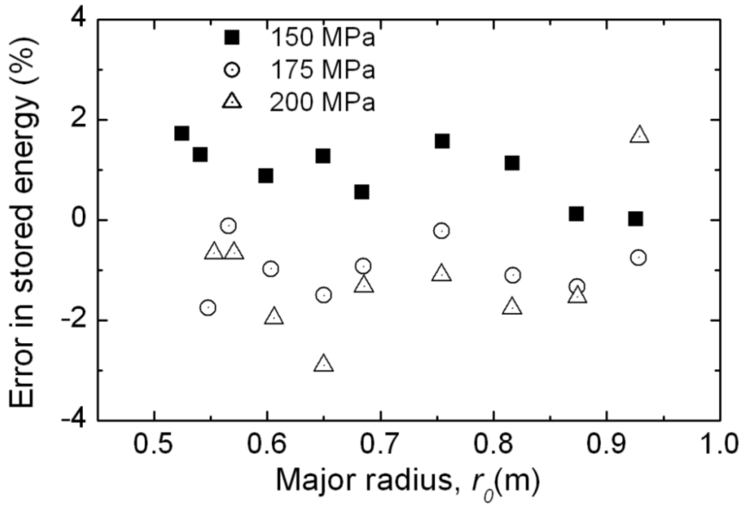

Figure 6.14 (c): Error on stored energy evaluation for Pareto solutions corresponding to N_s=8.

6.5 Conclusions

Pareto-optimal design for a sectored toroidal superconducting magnet for energy storage application has been investigated from the point of two conflicting objectives (superconducting cable length and magnet overall size) with the constraints of energy requirement, allowable hoop stress, and quench condition in terms of stability margin. The scheme is applicable to the design of toroidal-type SMES composed of circular coils with low temperature superconductor. The resulting trade-off solutions have revealed that the necessary length of superconducting cable is more for compact or reduced magnet overall size with increased peak magnetic field in the winding. AC loss developed during field transient to cater a peak rated power to the load also increases with compact magnet size. Furthermore, higher allowable hoop stress in the winding is desirable with regard to reduced necessary conductor length, AC loss, and magnet overall size. It is also observed that more the number of sectors, both the coil transport current and required conductor length, increases only marginally, but the stray magnetic field outside coil assembly reduces considerably.

CHAPTER 7

DESIGN STUDY OF SECTOR TOROIDAL MAGNET SYSTEM USING FEA

This chapter describes a design concept of the cryostat and coil assembly of sector-toroidal SMES system. Since the strong electromagnetic force distributed to the coil is asymmetric and non-uniform in nature, a precise 3-D finite element analysis (FEA) has been carried out to design a mechanically stable coil and support structure under various operational scenarios. The results reveal that maximum stress developed on coil and its support structure is below allowable stress limit. Extensive transient analysis has also been carried out to evaluate transient loss and assess the feasibility of using helium re-condensation technology with commercially available cryo-refrigerators. Finally, quench protection scenario has also been discussed suitable for this toroidal-type SMES system.

7.1 Coil Winding and Cryostat Design Concept

Because of the necessity of low loss operation for SMES coils, Rutherford type superconducting (SC) cable with inter-filamentary matrix Cu-0.5% Mn is specified in chapter 2 is considered for the design. Good electrical contact to neighbouring strands in the cable is ensured with stabrite (Sn-5%Ag) coating and heat treatment over the cable. The cable is wrapped with polyimide tape (~20 µm thick) with 50% overlap for turn to turn insulation.

Based on the design optimization as in chapter 6, the sectored toroidal SMES unit is composed of a finite number of sectors or elemental solenoid coils arranged in a toroidal fashion and are series-interconnected. The coils are thought to be liquid helium bath cooled at 4.2 K. In order to obtain good heat transfer between superconducting strands and liquid helium, the sector coil is considered to be manufactured with permeable windings. The permeable winding structure can be formed by laying glass-fiber reinforced plastic G-10 strips with equal interval between adjacent layers as shown in Figure 7.1(a). The whole toroidal coil system is supported through glass-fiber reinforced plastic (FRP) composite structure so that conduction heat load to the cryostat is reduced. In the present design, we considered that each sector coil will have a separate helium container conforming closely to coil geometry to minimize the liquid helium inventory. The entire toroidal-type coil assembly system is enclosed by thermal shield made of copper. The thermal shield is maintained at around 60-70 K using a single-stage cryo-refrigerator (~ 240 W at 60 K). The structural concept of the magnet is shown in Figure 7.1(b). There is a common buffer liquid helium reservoir at some higher elevation for continuously supplying liquid helium to the sector helium vessel.

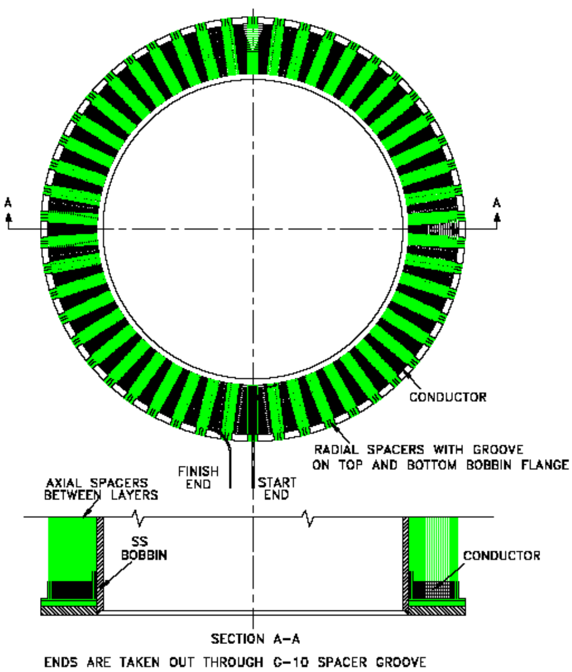

Figure 7.1(a): Coil winding scheme of the sector coil.

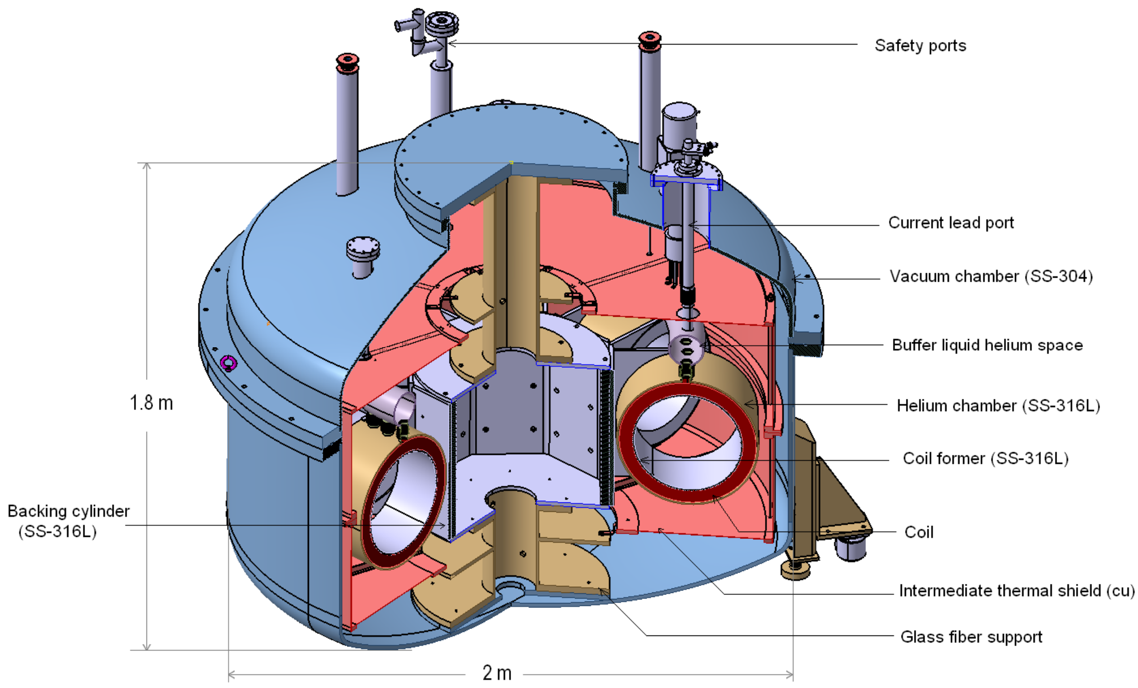

Figure 7.1(b): Design concept (3D-CAD model) of the SMES system with coil structure, intermediate shield, *etc.*

The magnetic field distribution around coils is asymmetric as shown in Figure 7.2 with the maximum magnetic field is 6.6 T at coil inner radius (Point B) in mid-plane (y=0 & z=0). The 0.5 mT contour line at the equatorial plane of torus (Z=0) is found to be at a distance of 2.0 m away from torus center.

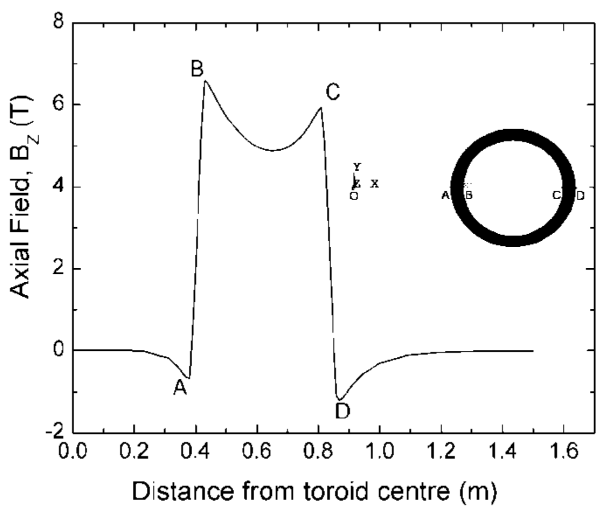

Figure 7.2: Axial magnetic field component on sector coil mid-plane (Y=0 & Z=0) measured from the center of the torus.

7.2 Magneto-structural Analysis

A magneto-structural analysis deals with the interaction between the structural and magnetic fields. Two different methods of coupled magneto-structural analysis exist: direct method [86] for strong coupling and sequential method [87] for weak coupling. The coupling matrix equations are expressed as

Direct coupling:
$$\begin{bmatrix} [K_{11}] & [K_{12}] \\ [K_{21}] & [K_{22}] \end{bmatrix} \begin{Bmatrix} U_1 \\ U_2 \end{Bmatrix} = \begin{Bmatrix} F_1 \\ F_2 \end{Bmatrix} \tag{7.1}$$

Sequential coupling:
$$\begin{bmatrix} [K_{11}] & [0] \\ [0] & [K_{22}] \end{bmatrix} \begin{Bmatrix} U_1 \\ U_2 \end{Bmatrix} = \begin{Bmatrix} F_1 \\ F_2 \end{Bmatrix} \tag{7.2}$$

The element matrices contains terms of both fields. Here $[K_{11}]$ and $[K_{22}]$ are element matrices of each field, U_1 and U_2 are two types of degree of freedom (DOF) matrices, and $[F_1]$ and $[F_2]$ are the excitation matrices. In direct coupling used mostly for highly non-linear coupled-field systems, the structural and magnetic systems of equations are coupled to form a single system of equations. In sequential coupling (or weak coupling method), the fields are solved in sequence and the results of first analysis is given as input to subsequent analysis. The analysis steps are as follows:

(i) The magnetostatic analysis is carried out with scalar potential formulation using weak coupling method.

(ii) The magnetic force distribution on the current carrying conductor is calculated from magnetostatic analysis.

(iii) The nodal magnetic force distribution is used as the structural load vector and structural analysis is carried out to find the mechanical displacement vector, U.

The structural matrix equations for FEA are derived from the fundamental equation of elasticity and principle of virtual work [88]. The strain energy and virtual work due to nodal displacements is made equal to find out the relation between elemental stiffness matrix and nodal force for single element.

The structural magnetic load vector R_m^s can be formulated either from Lorentz forces in non-magnetic current carrying conductor or distributed surface interactions on ferromagnetic structures [89]. The body force on a current carrying region is

$$F = \int_{\Omega} (J \times B)\, d\Omega \tag{7.3}$$

Here, Ω represents the conductor volume. The structural load vector R^s is comprised of different components including structural, thermal and magnetic loads. In finite element formulation, the structural magnetic load vector $R^s{}_m$ on a current carrying conductor is written as

$$R_m^s = \int_v N^T (J \times B) dV \tag{7.4}$$

Where N is the element shape function vector, J is current density in the coil, B is the magnetic field. For a ferromagnetic structure, total body force is expressed with Maxwell stress tensor T as

$$F = \frac{1}{\mu_0} \int_S \vec{T}.\hat{n}\, dS \tag{7.5}$$

Where n is the unit normal to the objective surface. The corresponding FEA load vector is

$$R_m^s = \int_s N^T (\vec{T}.\hat{n}) dS \tag{7.6}$$

Combining magnetic and structural equations, the matrix equation for each element is written as

$$\begin{bmatrix} K_i^m & 0 \\ 0 & K_i^s \end{bmatrix} \begin{bmatrix} \Delta\Phi \\ \Delta U \end{bmatrix} = \begin{bmatrix} R^m \\ R^s \end{bmatrix} - \begin{bmatrix} F_l^m \\ F_l^s \end{bmatrix} \tag{7.7}$$

The equations corresponding to each element are assembled and solved iteratively. The coupled field element includes several degrees of freedom (DOF) and associated coupling between them.

7.2.1 Cool Down and Steady State Operation

Superconducting magnet for energy storage application experiences mechanical stress and deformation during thermal cool-down to operating temperature and magneto-structural stress during frequent charging/discharging mode of operation. Since the magnet will experience cyclic load during charging/discharging operation, acceptable stress limit in all constituent material of support structure and coil are kept below endurance limit of constituent materials to discard any fatigue failure. Further, mechanical disturbances like conductor motion, *etc.* causes degradation and premature quench of the magnet. One-eighth ($1/8^{th}$) symmetry of sectored toroidal-type coil with support structure is modeled in 3-D with appropriate winding packing fraction in coil. The mechanical properties of the coil have been considered as orthotropic and homogenous with equivalent elastic modulus as summarized in Table 7.1.

The coil movement is arrested by suitable mechanical or support structure, which is primarily composed of three parts: coil former or bobbin with end flange, a central backing cylinder, and support plate as shown in Fig.7.3. In order to avoid any risk factor like brittle failure *etc.*, structural material mostly made of stainless steel (SS-316L) is considered, though glass-fiber based support structure is most suitable as per as transient loss is concerned. The finite element analysis (FEA) using commercially available multi-physics code ANSYS allows a detailed quantitative evaluation of stresses subject to more severe working conditions. One important feature of this ANSYS model is that coil is in sliding contact with coil former (SS-316L) using surface to surface contact element (CONTA172-TARGE169).

Table 7.1: Material Properties (at 4.2 K) of NbTi Rutherford-type coil and support structure material

	Coil (Equivalent properties)	Support Structure (SS-316 L)
Young's Modulus		
$Y_r(GPa)$	46.5	207
$Y_\theta(GPa)$	55	
$Y_z(GPa)$	55	
Shear Modulus		
$G_{r,\theta}(GPa)$	17.9	
$G_{\theta,z}(GPa)$	21.1	-
$G_{r,z}(GPa)$	21.1	
Poisson's ratio	0.3	0.3
Integrated thermal expansion(300-4.2K)	-2.59E-03	-2.98E-03

The friction coefficient between stainless steel former and coil is considered to be 0.35 [90]. Different radial turns in winding and support structure undergoes differential thermal contraction during cool-down to operating temperature of 4.2 K and exerts a radial inward force. Therefore, it is important to analyze thermal stress in combination with magneto-structural stress.

In the process of evaluating magneto-structural analysis, magnetic field and Lorentz force distribution on coils during excitation are computed first using coupled field element SOLID5. Electromagnetic force distribution on various nodes of the coils due to interaction of coil current density *J* and magnetic field *B* are asymmetric and non-uniform as shown in Figure 7.4.

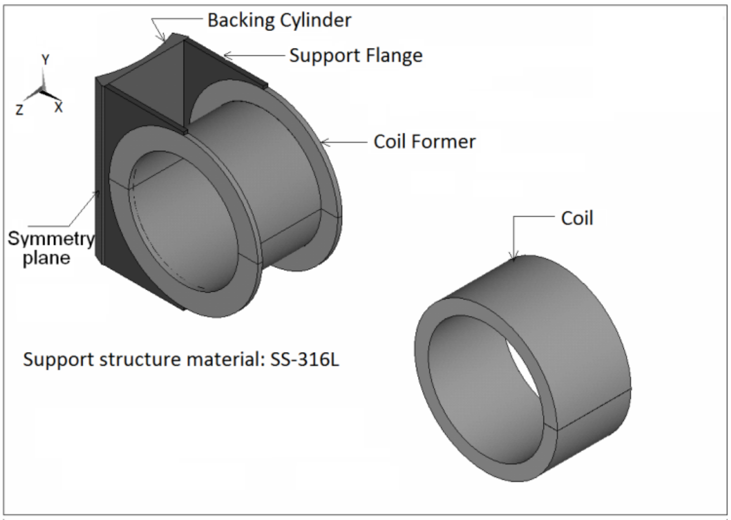

Figure 7.3: Exploded view of support structure (1/8th symmetry) comprising of backing cylinder, coil former and coil.

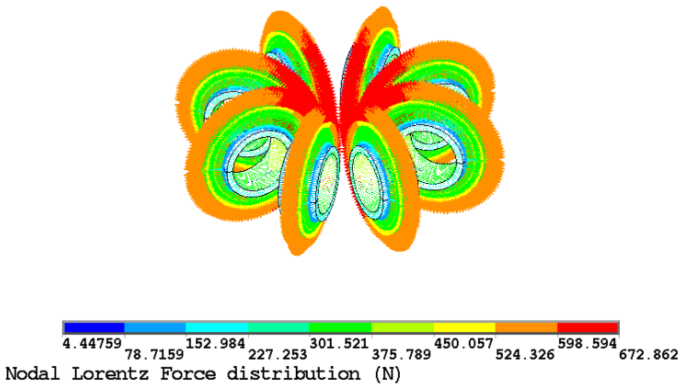

Figure 7.4: Lorentz force distribution of the sector coils at operating current of 1200 A.

The net force directed radially inward on each sector coil at maximum operating current is found to be 470 kN as obtained from Maxwell stress tensor formalism. This force transfers to backing cylinder through coil former and support flanges. Therefore, stress and deformation develops in both coil and support structure. The net forces on Y and Z directions are cancelled out when all coils are symmetrically placed.

The circumferential or hoop stress (σ_c) due to electromagnetic and thermal loading is found to be tensile and asymmetric with respect to angular position (θ) as observed in

Figure 7.5. Tensile stress at inner and outer radius of the sector coil mid-plane is found to be almost mirror symmetric, with mean radius r_c behaves as neutral radius.

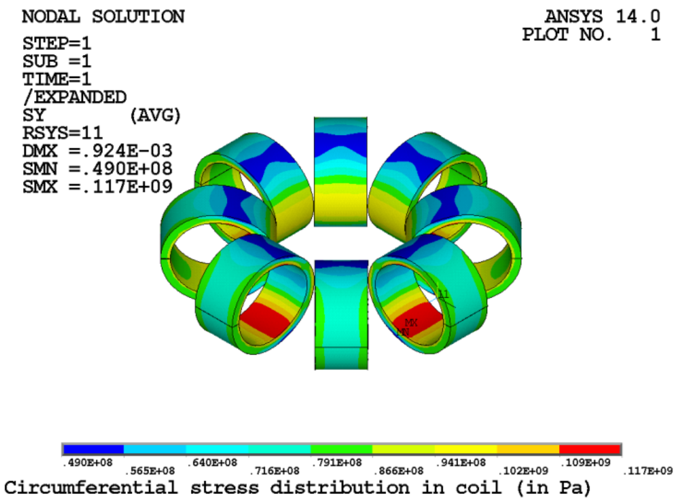

Figure 7.5: Circumferential stress (Pa) on coil due to excitation to 1200 A at 4.2 K.

The angle (θ) is measured from the horizontal axis passing through the equatorial plane (Z=0) of the coil. It is interesting to note that both the circumferential and von-Mises stress becomes maximum at a particular angular position (108-110 degree) as shown in Figure 7.6 though the peak magnetic field develops at $\theta=\pi$. This occurs due to the reaction force from the support structure.

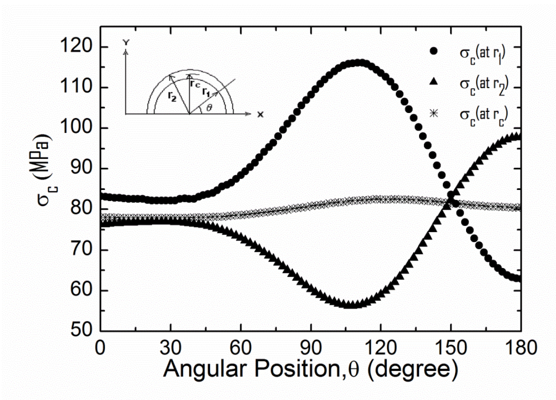

Figure 7.6: Circumferential stress (Pa) distribution (at mid-plane) with angular position (θ) in sector coil at 1200 A.

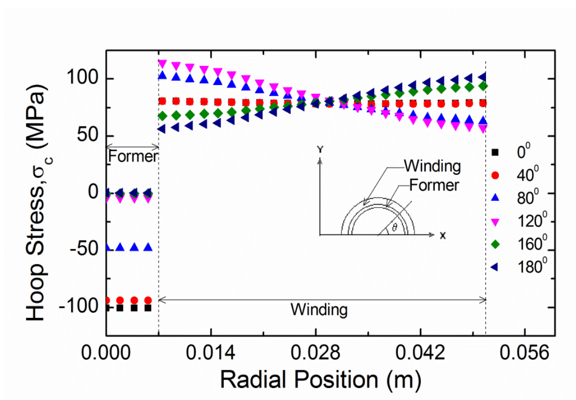

Figure 7.7: Circumferential stress (Pa) on coil former and coil at 1200 A at sector-coil mid-plane in torus equator (Z=0).

Variation of hoop stress with radial position for various coil azimuths θ, (in sector coil center at torus equatorial plane) is as shown in Figure 7.7.

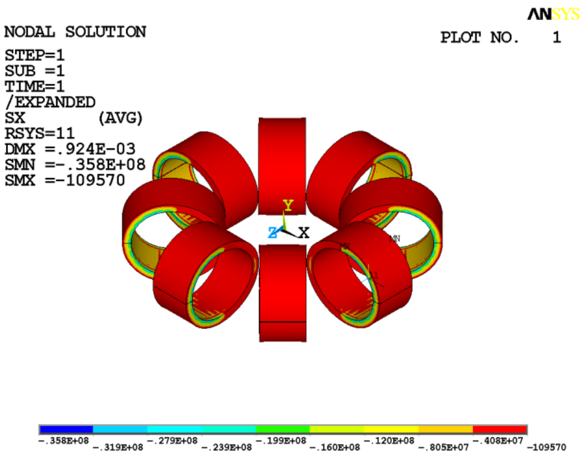

Figure 7.8: Radial stress (Pa) contours on coil at operating current of 1200 A at 4.2 K.

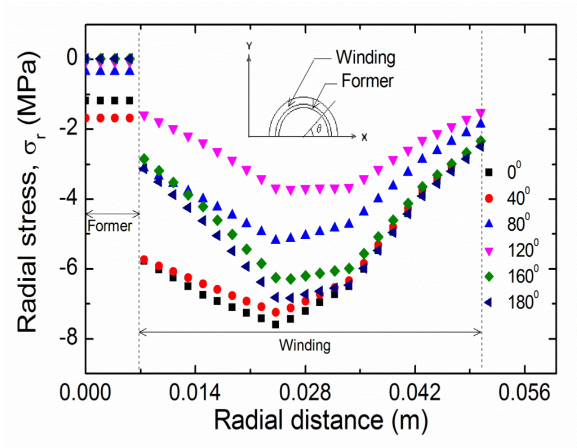

Figure 7.9: Radial stress on coil at excitation of 1200 A (at 4.2 K) at coil mid-plane (Z=0).

It is important to note that the radial stress developed in the coils is compressive (negative σ_r) in nature as shown in Figure 7.8 and Figure 7.9.

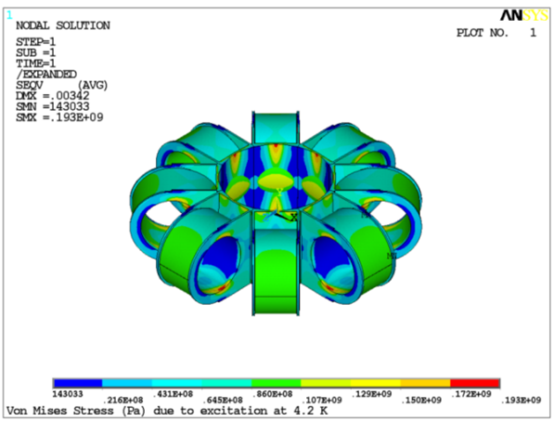

Figure 7.10: Von-Mises stress (Pa) on the coil assembly comprising of backing cylinder, coil former, coil, *etc.* at nominal operating current of 1200 A.

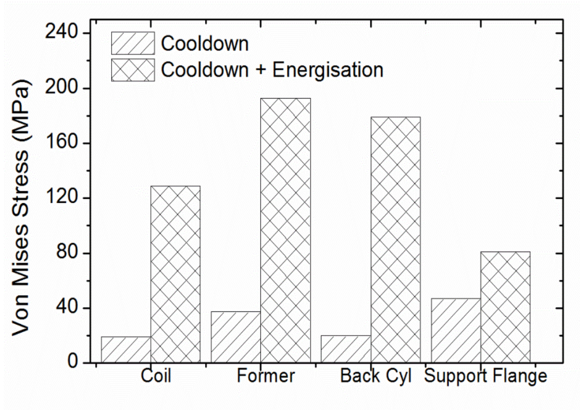

Figure 7.11: Maximum Von-Mises stress summary due to thermal cool-down to 4.2 K and excitation at 1200 A.

However, pretension of 12 kgf during coil winding will be provided to introduce little more compressive radial stress (~ 2.5 MPa at inner layer) on the winding so that it works reliably under all working conditions. The maximum axial compressive stress (σ_y) developed at coil innermost layer and $\theta = \pi$ were calculated to be 29 MPa and varies with axial, radial and azimuthal directions. The von-Mises stress distribution on assembly when coil is in full excitation at 4.2 K is shown in Figure 7.10. Maximum effective or von-Mises stress develops on stainless steel (SS-316L) coil former to be around 193 MPa, which is sufficiently below the allowable value (~ 550 MPa at 4.2 K).

The von-Mises Stress developed in different parts of the coil assembly is as summarized in Figure 7.11. Thermal stress due to cool-down has quite less contribution as a whole on assembly with respect to stress due to excitation.

7.2.2 Fatigue Analysis

The net Lorentz force acting on the coil is directed towards the centre of the torus. The support structure of the coil is designed to prevent this force from causing failure. During its life SMES coil will be subjected to cycles of charging and discharging. Thus the structural assessment of coil central support structure and the liquid helium jacket, which comprises of the stress analysis and the fatigue life assessment, is a critical part of the design. M. Verrecchia et al. [91] and N. Mitchell [92] have performed the fatigue life evaluation of the superconducting coils using Linear Elastic Fracture Mechanics (LEFM). The various approaches to fatigue assessment are: Stress life, Strain life and fracture mechanics. Stress life is based on the S-N (Stress vs Number of Cycles to failure) curve and is suitable for high cycle fatigue. Strain life approach is particularly suitable for low cycle fatigue, and is typically concerned with crack initiation. Fracture mechanics starts with an assumed flaw and determines the crack growth. For the purpose of present analysis, the strain life approach is used to determine the number of cycles before a crack is formed. After the stress distribution from the static stress analysis, the fatigue life is obtained using strain-life equation and equation for cyclic stress strain curve. Strain life equation which is valid for the entire life range of fatigue lives is given as [93]

$$\frac{\Delta\varepsilon}{2} = \frac{\sigma'_f}{Y}(2N)^{b'} + \varepsilon'_f(2N)^{c'} \tag{7.8}$$

where, $\Delta\varepsilon/2$ is the strain amplitude, σ'_f and ε'_f are respectively fatigue strength coefficient and fatigue ductility coefficient, b' and c' are respectively fatigue strength exponent and fatigue ductility exponent and $2N$ number of load reversals (N= number of cycles to failure). The equation for cyclic stress-strain curve is given as [94]

$$\frac{\Delta\varepsilon}{2} = \frac{\Delta\sigma}{2Y} + \frac{1}{2}\left(\frac{\Delta\sigma}{K'}\right)^{1/n'} \tag{7.9}$$

where, K' is the cyclic strength coefficient and n' is the strain hardening exponent.

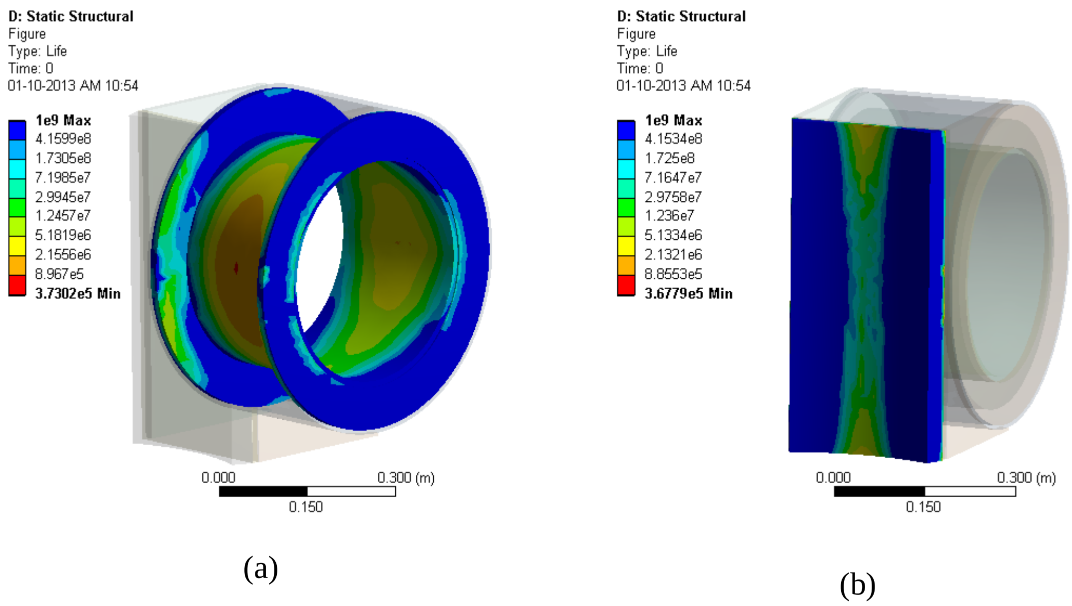

Figure 7.12: Fatigue life (cycles) for fully reversed loading (a) Coil former, (b) Backing cylinder.

Correlating equation (7.8) and equation (7.9) strain life parameters can be obtained. In the present analysis, the fatigue life for fully reversed loading (Stress ratio = -1) and for zero based loading (Stress ratio = 0) is evaluated. The values of minimum life for the two cases are found to be 3.7×10^5 cycles and 7.5×10^7 cycles respectively. The fatigue life for fully reversed and zero based load cases is shown in Figure 7.12 and Figure 7.13 respectively.

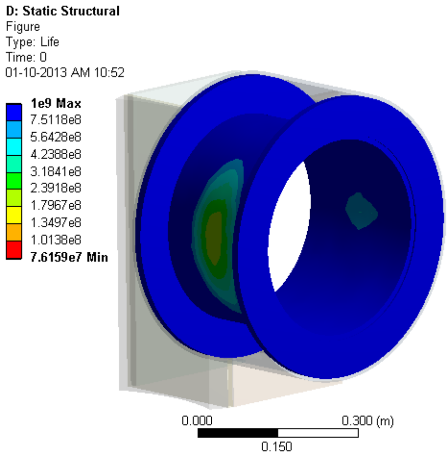

(a)

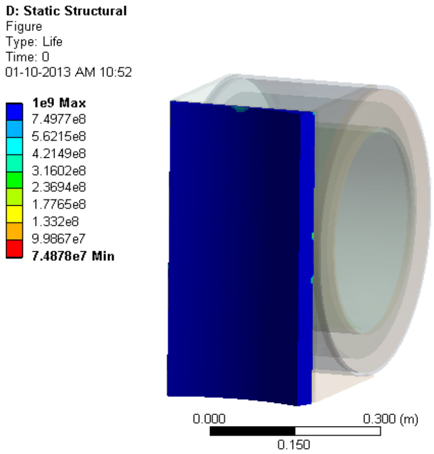

(b)

Figure 7.13: Fatigue life (cycles) for zero based loading (a) Coil former, (b) Backing cylinder.

7.3 Transient/ AC loss

7.3.1 Liquid Helium System

AC losses in liquid helium system are primarily contributed by hysteresis loss in superconducting filaments, coupling loss among multi-filamentary superconducting filaments and strands, induced eddy current in coil former, support structure and other metallic components. Loss from superconducting cable is calculated with local magnetic field distribution in winding layers and turns numerically. The AC loss contributions during discharge operations are [96]:

7.3.1.1 Superconducting Winding

The Hysteresis loss in filaments is given by

$$p_h = q_h \frac{\lambda V}{t_c} \tag{7.10}$$

Where, λ is the volume fraction of superconductor, V is the conductor volume, t_c is the carry over period, and q_h is given by

$$q_h = \frac{1}{\mu_0} \int_{B_i}^{B_f} M dB \tag{7.11}$$

Where, the initial and final magnetic fields are B_i and B_f respectively on the conductor. The filament magnetization M in presence of transport current in discharge mode is expressed by

$$M = \frac{2}{3\pi} \mu_0 J_c(B) d_f \left(1 - \frac{J}{J_c(B)}\right) \tag{7.12}$$

Where d_f is filament diameter, J is current density at some time instant of discharge, and J_c is the critical current density.

The coupling loss among filaments of twist pitch l_p is given by

$$p_{cf} = \frac{\lambda}{\rho_t} \left(\frac{l_p}{2\pi}\right)^2 \dot{B}^2 V \tag{7.13}$$

Where, ρ_t is the transverse resistivity of matrix material (Cu-0.5% Mn).

The inter-strand coupling loss via cross-over resistance (R_c) in transverse field is given by

$$p_{tc} = \frac{1}{120 R_c} \dot{B}_t^2 \frac{c}{b} N(N-1) l_t V \tag{7.14}$$

Where, l_t is cable twist pitch, B_t is the field transverse to the broad face of the cable, N is the number of strands, c is the half width of the cable and b is its half thickness.

The inter-strand coupling via adjacent resistance *(R_a)* in transverse field

$$p_{ta} = \frac{1}{24 R_a} \dot{B}_t^2 (N-1) l_p V \tag{7.15}$$

The inter-strand resistance via adjacent resistance *(R_a)* in parallel field is

$$p_{pa} = \frac{1}{32R_a}\dot{B}_p^2(N-1)\frac{b^2}{c^2}l_p V \tag{7.16}$$

where, $\dot{B}_p$ is the rate of change of field parallel to the broad face of the cable.

Unlike a single solenoid coil of cylindrical symmetric magnetic field distribution, magnetic field in a sectored-toroidal coil changes with coil azimuth (θ) in any given layer (n_r) and turn (n_z) of winding volume. Therefore, variation of both parallel and transverse field has been averaged over azimuth for each layer and turn of the winding volume as

$$\overline{B}_{p,n_r,n_z} = \frac{1}{\pi}\int_0^{\pi} B_{p,n_r,n_z}(\theta)\,d\theta \tag{7.17}$$

$$\overline{B}_{t,n_r,n_z} = \frac{1}{\pi}\int_0^{\pi} B_{t,n_r,n_z}(\theta)\,d\theta \tag{7.18}$$

Summing over the contribution from each layer and turn of winding volume with the consideration of local magnetic field distribution, AC loss from superconductor winding is evaluated and is shown in Figure 7.14. The temperature rise in the coil during discharge operation under adiabatic approximation is found to be around 0.15 K. Therefore, quench possibility during transient operation will not occur.

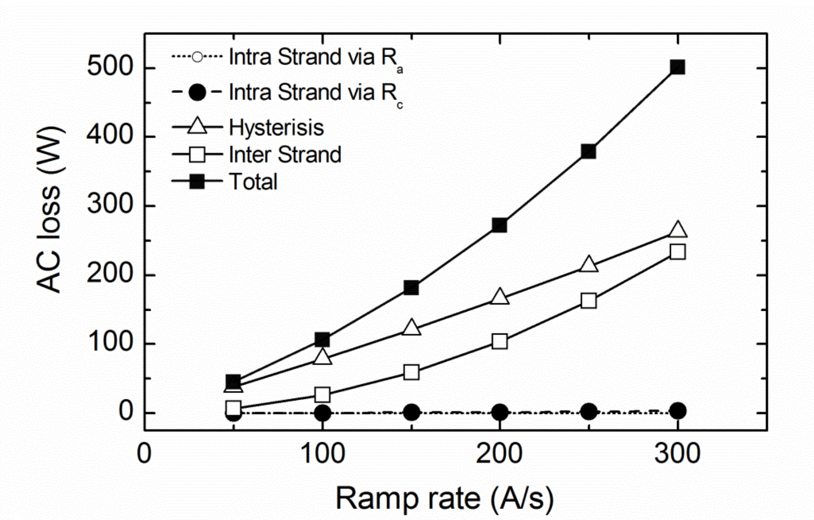

Figure 7.14: AC loss in the winding of the torus.

7.3.1.2 Coil Former and other Metallic Parts

In a homogeneous, isotropic and time invariant media, electric field induced by a changing magnetic field is given by

$$\nabla \times \vec{E} = -\dot{\vec{B}} \tag{7.19}$$

Induced electric field develops eddy current in the metallic arts inside cryostat. Coil former experiences maximum field transients out of all metallic parts present in the cryostat. It is desirable to have non-metallic coil former such as glass fiber reinforced plastic (FRP), *etc.* as per as eddy current is concerned. In our design, coil former is used as part of the helium vessel to minimize helium inventory, and FRP is not a good choice for coil former as per as structural reliability and fabrication of closed annular vessel is concerned. Eddy current in coil former during discharging can be readily estimated by the following differential equation:

$$L_2 \frac{dI_2}{dt} + M \frac{dI_1}{dt} + R_2 I_2 = 0 \tag{7.20}$$

where, $M = k\sqrt{L_1 L_2}$ is the mutual inductance between coil and coil-former. Here L_1 is self inductance of coil and L_2 is self inductance of former, M is mutual inductance between coil and former, I_1 is the coil current and I_2 is the induced current in former. Since the coil is closely made around the former, the coupling coefficient, $k \approx 1$. Simplifying eq. (7.20), induced current in former I_2 can be deduced with the initial condition: $I_2=0$ at $t=0$ as

$$I_2 = \frac{M}{R_2} . \frac{dI_1}{dt} \left[1 - \exp(-\frac{R_2}{L_2} t) \right] \tag{7.21}$$

Here, R_2 and L_2 can be determined considering former as a single turn secondary winding. Maximum field transient during operation is calculated to be 1.2 T/s (or equivalently, 200 A/s). The induced eddy current on the coil former dies out with a time constant (τ_s) can be written as

$$\tau_s = \frac{\mu_0 t_s r_s}{2\rho_s} \tag{7.22}$$

Here, μ_0 is free space permeability, t_s and r_s are thickness and inner radius of coil former respectively, ρ_s is the resistivity of stainless steel former. Considering t_s=0.007 m, r_s=0.19 m, and ρ_s(at 4.2 K for SS-316L)=4.96×10^{-7} Ω-m, typical value of time constant becomes τ_s~2 ms, which is much lower than the normal charging or discharging period. The thickness of coil former is minimized so that eddy loss could be reduced, but without compromising the mechanical stability and integrity of the coil assembly.

A detailed examination of the spatial dependence of eddy current density and loss using ANSYS code reveals that analytical result of eddy loss for coil former provides reasonably good estimate of eddy loss (8% deviation). Eddy current density developed on the coil former and support structure obtained using finite element code is as shown in Figure 7.15. Summing up the contribution from elements, induced eddy loss in the coil former and support structure together is as shown in Figure 7.16.

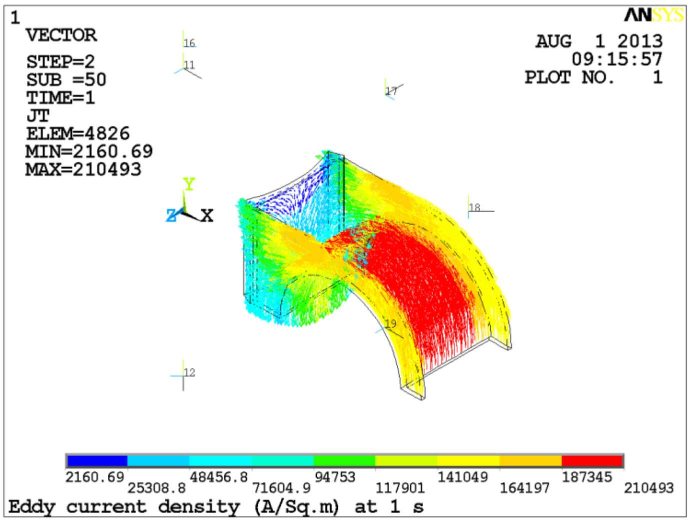

Figure 7.15: Distribution of eddy current density (Am^{-2}) vectors at coil former and support structure (at discharging rate of 200 A/s).

There are several kapton insulating layers around the coil former and epoxy based G-10 picket fences of 1 mm thickness around thereafter so that this heat flux from coil former is not directly transferred to superconducting sector coil, but boils off liquid helium. The top and bottom stainless steel flange of the coil former may be kept also thermally isolated using G-10 picket fences.

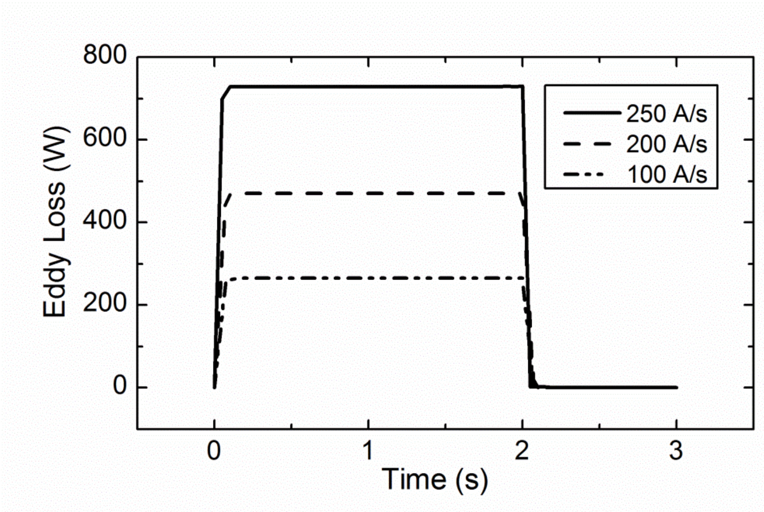

Figure 7.16: Total eddy loss in coil former and support structure at 4.2 K.

The total transient loss comprising from both AC loss from superconductor and eddy loss from coil former with support structure would be around 1000 J at 4.2 K (considering about 25 % contingency) and must be handled by cryogenics system. This energy is equivalent to boil-off of 0.4 liter of liquid helium. If the discharge occurs eight times a day, this provides an additional heat load of 2% to the steady state heat load. The steady state load to the helium chamber is calculated to be around 2.0 W at 4.2 K. It is proposed to have four numbers of two-stage Gifford-McMahon (GM) type cryo-refrigerator (1.5 W at 4.2 K each) to mitigate both transient and steady state load.

7.3.2 Intermediate Thermal Shield

Since the stray magnetic field outside is significantly low due to toroidal-type configuration, induced eddy current on thermal shield around the coils is not of major concern. Induced eddy current density in thermal shield simulated with FEA is as shown in Figure 7.17. The thermal shield around liquid helium vessel has more time constant since it is made of copper with resistivity (at 60 K) two orders of magnitude less than that of stainless steel. Eddy loss developed on thermal shield is shown in Figure 7.18. The total heat load combining both steady state and transient load is around 180 W at 60 K, which is well within the capacity of a standard commercially available single-stage cryo-refrigerator.

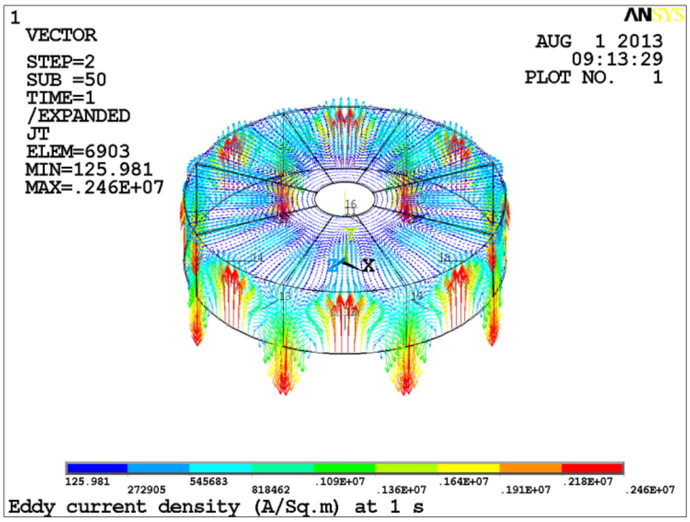

Figure 7.17: Eddy current density (A/m^2) at intermediate shield (upper half) for 200A/s.

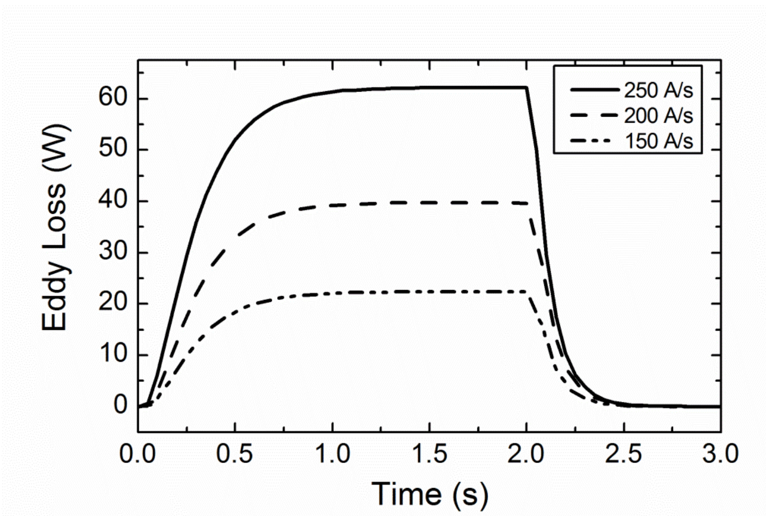

Figure 7.18: Eddy loss in intermediate thermal shield at 60 K.

In adiabatic situation, the maximum temperature rise of thermal shield during transient of 200A/s (1.2 T/s) is found to be less than 0.3 K. The mechanical von-Mises stress developed on the intermediate shield due to interaction of induced current density and magnetic field for maximum field transients is found to be around 6.2 MPa, which suggest that the thermal shield would be safe from any structural deformation during field transient. The primary design specification of the 4.5 MJ/1MW/2s sector toroidal SMES system is as summarized in Table 7.3.

Table 7.2: Design summary of 4.5 MJ/1MW sector-toroidal SMES system

Coil arrangement	Toroidal-type
Number of sectors	8
Total conductor length (km)	15.2
Conductor	NbTi based Rutherford-type cable
Operating current, *Iop*(A)	1200
Number of	
inter-sector joints	7
superconductor-magnet lead joints	2
Maximum von-Mises stress (MPa)	
on coil/coil former at 1200 A	117/193
Liquid helium chamber at 4.2 K	
Steady state load(W)	2.0
Dynamic load (W) during discharge (200 A/s)	1000.0
Intermediate shield at 60K	
Steady state load (W)	120.0
Dynamic load (W) during discharge (200 A/s)	60.0
Number of cryo-refrigerators	
Two-stage (1.5 W at 4.2 K)	3
Single stage (240 W at 60 K)	1

7.4 Quench Protection Scheme

Sector coils are series interconnected electrically. In case of quench like fault in one coil, magnet safety requires that temperature and voltage developed during a quench remains below certain level. The stored energy either is to be extracted or distributed uniformly in coils at the onset of quench by suitable quench protection scheme. One important requirement in the circuit arrangement is to maintain electromagnetic forces balanced azimuthally and vertically during a quench. Quench simulation of SMES consisting of several superconducting coils in a toroidal configurations are discussed by many authors [96-101]. Kaerner [99] used a scheme suitable for multiple SMES coils where upon quench detection, the weak coil is shunted by the cold IGBT switch.

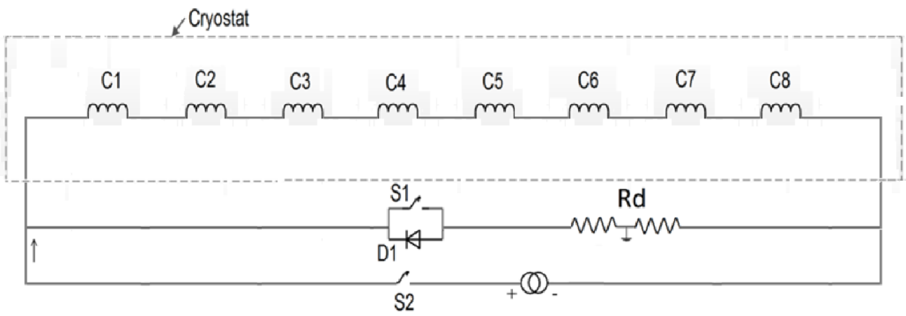

Figure 7.19 (a): Quench protection circuit with a single dump resistor across the coil assembly.

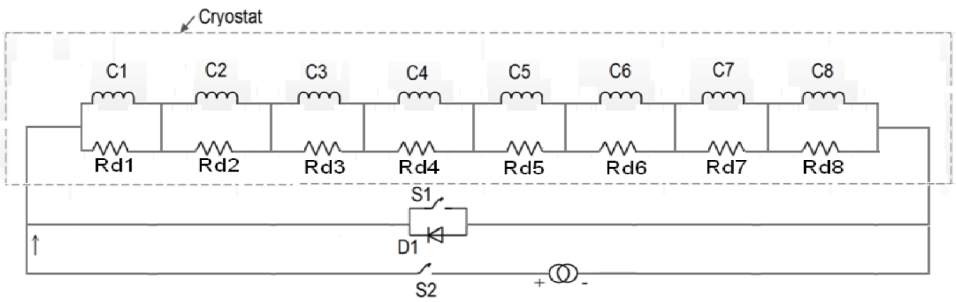

Figure 7.19 (b): Quench protection circuit with dump resistors across each sector coil.

The weak coil is rapidly dumped by quench heater and thereafter, rests of the coils are ramped down. However, following this scheme issues like non-availability of high current

IGBT switch working at cryogenic temperature, unbalanced force among sectors and stray magnetic field develops with this scheme during quench like scenario needs to be addressed.

A viable electrical connection scheme for quench protection is shown in Figure 7.19(a). The other alternative is to adopt external dump resistors parallel to each sector coil as in Figure 7.19(b), which is suitable for achieving reduced peak voltage across the quenched coil. The second approach will, however, increase the complexity in cryostat and moreover, the force balance between neighboring coils is disturbed in this situation due to unequal current in the coils. The third option could be to use quench protection heater along with series connected dump resistors. The self and mutual inductance matrix among the sector coils is computed calculating internal energy and interaction energy of neighboring coils respectively.

The self and mutual inductance matrix among the sector coils is computed calculating internal energy and interaction energy of neighboring coils respectively. The coupled nonlinear transient thermal and electromagnetic models circuit models are solved with commercial FEA-based software "Vector Fields Opera-Quench" [102] to understand and finalize the quench protection scheme. The transient heat balance equations is

$$\nabla . k(T)\,\nabla T + Q + Q_{ext} = C(T)\frac{\partial T}{\partial t} \qquad (7.23)$$

Here *T, k(T),* Q_{ext}, and *C(T)* represents the coil temperature, the thermal conductivity, the external heat generation for provoking quench and volumetric specific heat respectively. The ohmic heat source density (*Q*) is given by

$$Q = \frac{|N_m|}{A}\left(\frac{1}{f_m \sigma_m(B,T) + (1 - f_m)\sigma_{sc}(B,T)}\right) I_{op}^2 \qquad (7.24)$$

where N_m is a vector turn density [103] defined as current density to operating current ratio, f_m is non-superconductor (matrix) to superconductor ratio, A is the cable cross-sectional area, $\sigma_m(B,T)$ is the matrix electrical conductivity, and $\sigma_{sc}(B,T)$ is the electrical conductivity of superconductor. The Quench code closely couples the nonlinear transient thermal, electromagnetic and circuit models. The transient thermal and electromagnetic field simulations were implemented using an adaptive Galerkin time stepping method in the Quench code. The whole magnet is initialized to the original temperature of 4.2 K and initial current of 1200 A. The heat transfer coefficient to the liquid helium coolant is considered to be negligible during the process of quench. A point pulsed heat flux continuing about 10 ms is added at the middle turn of coil mid plane, which is good enough to raise the temperature of superconductor to its current sharing temperature.

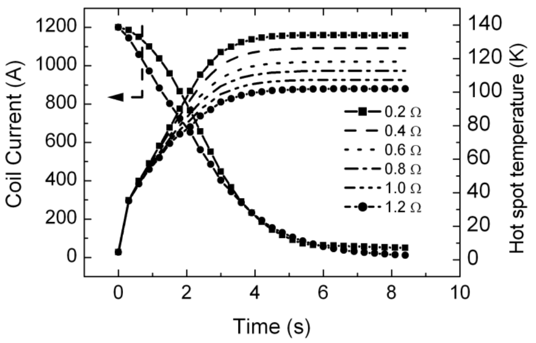

Figure 7.20(a): Transition of coil current and hot spot temperature with different dump resistors.

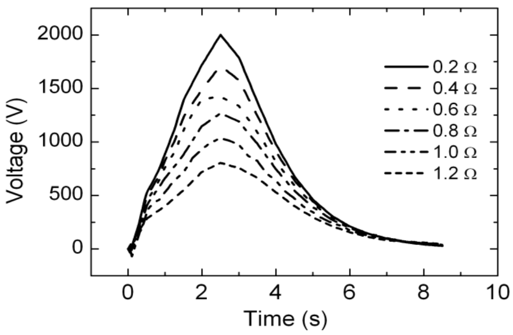

Figure 7.20 (b): Transition of voltage across coil with different dump resistors during quench.

In the model, the switch S1 is assumed to be closed and S2 opened up as soon as the quench is detected. The diode D1 parallel to the switch S1 provides redundancy of the protection mechanism. Quench onset starts in the simulation when the differential voltage among any two coils is more than 100 mV with validation period of 100 ms. For different dump resistors with no active protection by quench heater, the coil current and hot spot temperature is as shown in Figure 7.20(a). The voltage evolution across the quenched coil is shown in Figure 7.20(b). It is observed that more than 1.0 Ω dump resistor is required to keep the coil maximum voltage below 1 kV limit. The other option is to use lower value of dump resistor with active protection by quench heater. It is found that quench heater of 1 inch width around the coil outer mid-plane with heat flux of 2 W/cm^2 (for 25-50 ms) along with dump resistor of 0.1 Ω is also feasible and may be a better option to keep both the maximum temperature below 100 K and most importantly terminal voltage across each coil below 1 kV limit. In the present simulation we have taken up a realistic heater delay time of 100 ms upon quench detection based on our experience of developed capacitive heater power supply.

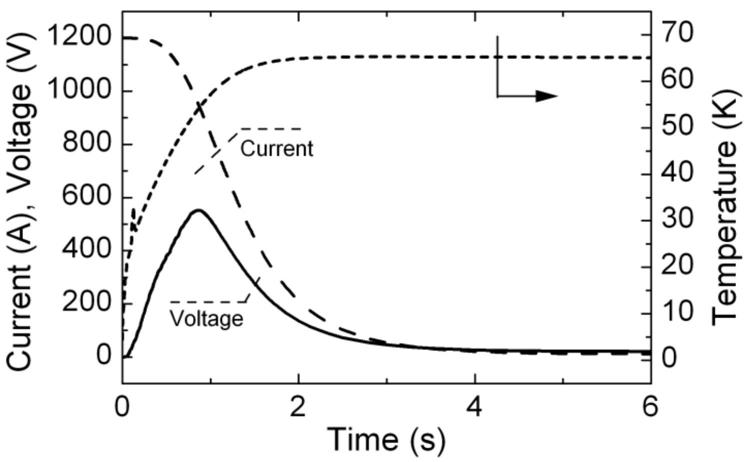

Figure 7.21: Transition of coil current, voltage across quenched coil and coil hot spot temperature with quench heater and R_d=0.1 Ω.

If all eight coils are heater fired upon detection of quench, the peak voltage across the quenched coil reduces to 550 V with the hot spot temperature of 65 K as shown in Figure7.21. The maximum terminal voltage across the current leads is found to be 250 V, which is less than the voltage across quenched coil. This is due to the fact that the resistive voltage and induced inductive voltages during current decay are of opposite direction. It is observed that if at least three coils are heater-fired upon detection of quench, peak voltage across the quenched coil becomes less than 1 kV limit. The center of the dump resistor may be earthed with the cryostat body so that the coil terminal voltage with respect to cryostat is reduced to half.

7.5 Conclusions

A small-scale 4.5MJ/ 1 MW/2 s toroidal-type superconducting magnet for SMES system is designed. The mechanical behavior of the magnet with the support structure is studied by commercial code ANSYS. All parts of coil remain under compression (or negative radial stress) at full excitation with the inner most layer maintain compressive contact with coil former. Effect of thermal stress on whole assembly has been found to be less with respect to electromagnetic (EM) stress. The maximum von-Mises stress in coil and coil former support assembly is found to be within allowable limiting value. The analysis allows a detailed quantitative evaluation of the stresses in the coil and support structure subject to all possible working conditions. Transient loss including AC loss in superconductor and eddy current loss in coil support structure and former has been evaluated. Heater induced active quench protection in fail-safe mode is found to be better option for quench protection ensuring no magnet damage.

CHAPTER 8

SUMMARY AND CONCLUSIONS

The work presented in the thesis deals with the design and optimisation of superconducting magnet system for energy storage application for voltage dip/sag mitigation. Two different types of superconductors are considered: NbTi based cryostable conductor and NbTi based Rutherford type cable.

In this work, both the types of superconductors are extensively characterised in terms of their electrical and mechanical properties that are necessary for the design and development of the SMES coil. Superconducting joints with cryostable conductors are also developed and standardised with an acceptable joint resistance less than 20 nΩ. An analytical method has been developed for the design oprtimisation of SMES coil. This optimisation minimizes the conductor volume and has been used for the development of 0.6 MJ/0.25 MW SMES coil. The coil parameters and operating points are determined in the optimisation algorithm using differential evolution method.

The work presented in this thesis may be summarised as:

- For design and development of SMES coil, the necessary electrical and mechanical performance tests of the conductors (NbTi based cryostable conductor and Rutherford type cable) have been carried out.
- Based on analytical approach a design optimisation formulation has been developed using differential evolution algorithm and applied to design and develop a 0.6 MJ solenoid-type SMES coil.

- Detailed magneto-structural stress analysis has been carried out to determine the required winding tension so that radial stress is compressive under all possible scenarios.
- One dimensional quench simulation code has been developed to study the quench phenomena and protection scenarios of 0.6 MJ SMES coil.
- Air cooled modular-type dump resistor has been designed, developed and implemented with the protection circuit of the SMES coil.
- Finite element modelling is done to determine the transient loss during operation of the SMES coil and thereby, the cryogenic loss.
- Coil is integrated with the cryogenic system and field test was carried out with DC power supply. Transient loss in the cryostat was measured for several charge/discharge cycles using calorimetric method and compared with calculated value.
- During field test, provoked quench was carried out at maximum operating current of 800 A and the quench parameters are studied. The quench simulation results agree well with experimental performance.
- Finally, the Power Conditioning System (PCS) with a resistive load are integrated with SMES coil and voltage dip/sag has been mitigated for different carry over period of up to 2 s to carry out its functionality test.

The thesis also includes design study of a 4.5 MJ/1 MW SMES system with NbTi based Rutherford-type cable. Design aspects of two different coil configurations, solenoid-type and sector-toroidal type, have been explored. A generalised design optimisation with the objective function of overall refrigeration load (both AC loss and steady-state heat load) in to the cryogenic system of a solenoid-type SMES coil using Rutherford-type NbTi cable has been carried out. Effect of various constraint parameters such as coil peak circumferential stress, peak voltage across the coil during discharge, *etc.*, on the design parameters has been investigated. Further, a Pareto-optimal design algorithm of sectored-toroidal SMES coil comprising of solenoid coils has been developed. The design results have been bechmarked with finite element analysis of a 3D model of the same. The design study may be summarised as follows:

- A new approach for the design of superconducting magnet for energy storage purpose has been developed. Despite the non-linearity of the problem, in most of the cases the optimisation converges to feasible solutions within a reasonable number of iterations.
- A novel design concept of solenoid-type SMES coil with Rutherford-type cable has been proposed that minimizes cryogenic refrigeration load into the magnet cryostat.
- Pareto-optimal design for a 4.5 MJ/1MW sector-toroidal type SMES coil has been developed using Rutherford-type cable.
- Detailed finite element analysis has been carried out to understand the magneto-structural stress development in the winding and support structure. Magnet cryostat assembly has been conceptualized and designed accordingly.
- Detailed fatigue analysis on coil and support structure has also been carried out using finite element analysis to understand the magnet charge/discharge effect.
- Transient analysis in sectored-toroidal system to estimate AC loss in the winding and eddy loss in support structure, intermediate thermal shield, *etc.* has also been carried out. Conductor stability has also been investigated during charge/discharge operation of the SMES coil.
- Finally, detailed quench study is done using finite element analysis (FEA) code OPERA to investigate the suitable protection scheme. An active protection scheme

using both quench heater and dump resistor is recommended for safe and reliable operation.

- The works presented in this thesis have generated a number of scientific publications in peer-reviewed journals.

Scope for Further Research

Further research is envisaged for the development of cryo-cooler assisted 4.5 MJ/ 1.0 MW SMES system. These are:

- The research of magnet transients with the power electronics may be carried out under various operational scenarios to understand the behaviour of the coil during load levelling, voltage mitigations, *etc.*
- The numerical modelling of Rutherford-type cable may be performed to determine the minimum quench energy (MQE) of the particular cable and its stability performances under various types of disturbances.
- Detail quench-back scenario needs to be investigated to understand its effect on active coil protection system of sector toroidal system.
- Liquid helium recondensation technology with 4.2 K cryo-refrigerator may be incorporated to develop a small scale SMES system to make it commercially viable. Detailed design study related to recondenser technology may be taken up, which is relevant for superconducting magnets used in other applications too.

APPENDIX

A) The Struve function

The Struve function for integer order, denoted as $H_n(x)$ is given by

$$H_n(x) = \left(\frac{1}{2}x\right)^{n+1} \sum_{k=0}^{\infty} \frac{(-1)^k \left(\frac{1}{2}x\right)^{2k}}{\Gamma\left(k+\frac{3}{2}\right)\Gamma\left(k+n+\frac{3}{2}\right)} \tag{A.1}$$

$$\begin{aligned} H_0(x) &= \frac{2}{\pi} \sum_{k=0}^{\infty} \frac{(-1)^k}{[(2k+1)!!]^2}.x^{2k+1} \\ &= \frac{2}{\pi}\left(x - \frac{1}{9}.x^3 + \frac{1}{225}.x^5 - \frac{1}{11025}.x^7 + \frac{1}{893025}.x^9 - \cdots\right) \end{aligned} \tag{A.2}$$

$$\begin{aligned} H_1(x) &= \frac{2}{\pi} \sum_{k=1}^{\infty} \frac{(-1)^{k+1}}{(2k-1)!!(2k+1)!!}.x^{2k} \\ &= \frac{2}{\pi}\left(\frac{1}{3}.x^2 - \frac{1}{45}.x^4 + \frac{1}{1575}.x^6 - \frac{1}{99225}.x^8 + \cdots\right) \end{aligned} \tag{A.3}$$

B) The Bessel function of first kind

The Bessel function of first kind is given by

$$J_n(x) = \sum_{k=0}^{\infty} \frac{(-1)^k \left(\frac{1}{2}x\right)^{n+2k}}{k!\,\Gamma(k+n+1)} \tag{A.4}$$

The expansion of the function provides

$$J_0(x) = 1 - \frac{x^2}{2^2} + \frac{x^4}{2^4(2!)^2} - \frac{x^6}{2^6(3!)^2} + \cdots \tag{A.5}$$

$$J_1(x) = \frac{x}{2} - \frac{x^3}{2^3(2!)} + \frac{x^5}{2^5(2!)(3!)} - \frac{x^7}{2^7(3!)(4!)} + \cdots \tag{A.6}$$

BIBLIOGRAPHY

[1] A. T. Almeida, "Power Quality Problems and New Solutions", *International Conference on Renewable Power and Power Quality*, Spain, (2003).

[2] Y. Tatsuta, S. Koso, K. Terazono, S. Taniguchi, S. Nagaya, H. Ohsaki, "Cost Reduction Measures for SMES", *Journal of the Cryogenic Society of Japan*, **40** (2005) 141-149.

[3] P. Tixador, "Superconducting Energy Storage: Status and Perspective, *IEEE/CSC & ESAS European Superconductivity News Forum,* **3** (2008) 1-14.

[4] H. L. Laquer, F. L. Ribe, D. M. Weldon, "Energy Storage and Switching with Superconductors as a Power Source for Magnetic Fields in Pulsed Thermonuclear Experiments and Reactors", *Intersociety Energy Conversion Engineering Conference, Boston*, (1971) 1089-1095.

[5] R. W. Boom, H. A. Peterson, "Superconducting Energy Storage for Power Systems", *IEEE Transactions on Magnetics,* **8** (1972) 701-703.

[6] J. Rogers, H. Boenig, J. Bronson, D. Colyer, W. Hassezahl, R. Turner, R. Schermer, "30-MJ superconducting magnetic energy storage (SMES) unit for stabilizing an electric transmission system", *IEEE Transactions on Magnetics,* **15**(1979) 820-823.

[7] T. R. Abel, "D-SMES for Wisconsin", *Modern Power Systems,* **19** (1999) 28-29.

[8] M. Steurer, C. A. Luongo, P. R. Ribeiro, S. Eckroad, "Interaction between a superconducting coil and the power electronic interface on a 100 MJ SMES system", *IEEE Transactions on Applied Superconductivity,* **13** (2003) 1806-1809.

[9] H. Salbert, D. Krischel, A. Hobl, M. Schillo, N. Blacha, A. Tromm, W. Roesgen, "2MJ SMES for uninterruptible power supply", *IEEE Transactions on Applied Superconductivity,* **10** (2000) 777-779.

[10] Y. Ishigaki, H. Shirahama, K. Kuroda, "Power control experiments using a 5 MJ superconducting magnetic energy storage systems", *Power Electronics Specialists Conference, 1988, PESC '88 Record, 19th Annual IEEE,* **1** (1988) 301-306.

[11] J. Rogers, M. Barron, H. Boenig, A. Criscuolo, J. Dean, R. Schermer, "Superconducting magnetic energy storage for BPA transmission line stabilization", *IEEE Transactions on Magnetics,* **19** (1983) 1078-1080.

[12] H. Hayashi, K. Honda, H. Kanetaka, T.Sannomiya, T. Imayoshi, K. Tsutsumi, F. Irie, M. Takeo, K. Funaki, T. Ezaki, H.Okada, R. Ito, F. Sumiyoshi, S. Ioka, K. Asano, S. Nose, H. Yamamura,"Results of tests on components and the system of 1 kWh/1MW module-type SMES", *IEEE Transactions on Applied Superconductivity,* **9** (1999) 313-317.

[13] H. Hayashi, T. Sannomiya, K. Tsutsumi, F. Irie, F. Sumiyoshi, S. Hanai, K. Asano, S.Nose, "Losses in Superconducting Coils of 1 kWh/1MW SMES", *IEEE Transactions on Applied Superconductivity,* **10** (2000) 816-819.

[14] T.Katagiri, H.Nakabayashi, Y.nijo, T.Tanda, T.Noda, T.nagata, S.nagaya, M.Yamane, Y.Ishii and T.Nitta, "Field test results of 10 MVA/20 MJ SMES for load fluctuation compensation", *IEEE Transactions on Applied Superconductivity*, **19** (2009) 1993-1998.

[15] H.J. Kim, K. C. Seong, J.W. Cho, J.H. Bae, K. D. Sim, K.W. Ryu, B.Y. Seok, S. H. Kim, "Development of a 3MJ/750 kVA SMES system", *Cryogenics*, **46** (2006) 367-372.

[16] W. Kim, S. Kwak, J. Lee, D. Choi, H. Jung, K. Seong, S. Hahn, "Design of HTS magnets for a 600 kJ SMES", *IEEE Transactions on Applied Superconductivity,* **16** (2006) 620-623.

[17] S. Lee, S. H. Park, W.S. Kim, J.K. Lee, S. Lee, C. Park, J.H. Bae, S.H. Kim, K. C. Seong, K. Choi, S. Hahn, "Analysis of Eddy current losses and magnetization losses in toroidal magnets for a 2.5 MJ HTS SMES", *IEEE Transactions on Applied Superconductivity,* **21** (2011) 1354-1357.

[18] L. Ren, X. Ying, Z. Wenping, *et al.*, "Development of a movable HTS SMES system", *IEEE Transactions on Applied Superconductivity,* **25** (2015) 1-9.

[19] J. Bardeen, L. N. Cooper, J. R. Schrieffer, "Theory of Superconductivity", *Physical Review,* **108** (1957) 1175-1204.

[20] A. L. Bindari, M. M. Litvak, "Upper critical field of NbZr and NbTi Alloys", *Journal of Applied Physics,* **34** (1963) 2913.

[21] T. G. Berlincourt, R. R. Hake, "Superconductivity at high magnetic fields", *Physical Review Letters,* **131** (1963), 140-157.

[22] P. J. Lee, "A comparison of superconductor critical currents", Applied Superconductivity Centre, National High Magnetic Field Laboratory, FSU, *http://www.magnet.fsu.edu/magnettechnology/research/asc/plots.html.*

[23] B. T. Matthias, T. H. Geballe, S. Geller, E. Corenzwit, "Superconductivity of Nb_3Sn", *Physical Review,* **95** (1954) 1435.

[24] J. E. Kunzler, E. Buehler, F. S. L. Hsu, J. H. Wernick, "Superconductivity in Nb_3Sn at high current density at a magnetic field of 88 kgauss", *Physical Review Letters,* **6** (1961), 89-91.

[25] T. Kogaku, "Development of cost reduction SMES for load fluctuation compensation and frequency control", *Journal of Cryogenics and Superconductivity Society, Japan,* **40** (2005)159-166.

[26] H. Maeda, Y. Tanaka, M. Fukutomi, T Asano, “A new High Tc oxide superconductor without a rare earth element”, *Japanese Journal of Applied Physics,* **27** (1988) L209-L210.

[27] M. K. Wu, J. R. Ashburn, C. J. Tong, P. H. Hor, R. L. Memng, L. Gao, Z. J. Huang, Y. Q. Wang, C. W. Chu, “Superconductivity at 93 K in a new mixed phase Y-Ba-Cu-O compound system at ambient pressure”, *Physical Review Letters*, **58** (1987), 908-910.

[28] Superpower Inc., http://www.superpower-inc.com.

[29] Sumitomo Electric Inductries Ltd., http://www.sei.co.jp/super.

[30] K. Kinoshita, “HTS development and industrialization at Sumitomo”, 1st Workshop on Accelerator Magnet in HTS, DESY, Germany, (2014), http://indico.cern.ch/event/308828/session/2/contribution/9/material/slides/1.pdf.

[31] X. W. Wu, S. R. Foltyn, P. N. Arendt, W. R. Blumenthal, I. H. Campbell, J. D. Cotton, J. Y. Coulter, W. L. Hultus, M. P. Maley, H. F. Safar, J. L.Smith, “Properties of $YBa_2Cu_3O_7$ thick films on flexible buffered metallic substrate”, *Applied Physics Letters,* **67** (1995) 2397-2399.

[32] A. Goyal, D. P. Norton, J. D. Budai, M. Paranthaman, E. D. Specht, D. M. Kroeger, D. K. Christen, Q. He, B. Saffian, F. A. List, D. F. Lee, P. M. Martin, C. E. Klabunde, E. Hartfield, V. K. Sikka, “High critical current density superconducting tapes by epitaxial deposition of YBa2Cu3Ox thick films on biaxially textured metals”, *Applied Physics Letters,* **69** (1996) 1795-1797.

[33] M. Oomen, W. Herkert, D. Bayer, P. Kummeth, W. Nick, T. Arndt, “Manufacturing and test of 2G-HTS coils for rotating machines: Challenges, conductor requirements, realization”, *Physica C,* **482,** (2012) 111-118.

[34] T. Takematsu, R. Hua, T. Takao, Y. Yanagisawa, H. Nakagome, D. Uglietti, T. Kiyoshi, M. Takahashi, H. Maeda,” Degradation of the performance of a YBCO-coated conductor double pancake coil due to epoxy impregnation”, *Physica C,* **470** (2010) 674-677.

[35] D. Larbalestier, A. Gurevich, D. M. Feldmann, A. Polyanskii,”High-Tc superconducting materials for electric power applications”, *Nature,* **414** (2001) 368-377.

[36] M. N. Wilson, *Superconducting Magnets,* New York: Oxford University Press (1983).

[37] Z. J. J. Stekly, R. Thome, B. Strauss, “Principle of stability in cooled supeconducting magnets”, *Journal of Applied Physics,* **40** (1969) 2238-2245.

[38] C. Polk, R. W. Boom, Y. M. Eyssa, “Superconducting Magnetic Energy Storage (SMES) External Fields and Safety Considerations”, *IEEE Transaction on Magnetics,* **28** (1992) 478-481.

[39] T. Hamajima, M. Shimada, S. Hanai, Y. Wachi, M. Tezuka, H. Takano, “SMES coil configurations with Reduced Stray Field”, *IEEE Transaction on Magnetics,* **9** (1999) 346-349.

[40] G. Schonwetter, “SMES solenoids with reduced stray field”, *IEEE Tranaction on Magnetics,* **30** (1994) 2636-2639.

[41] P. Alotto, U. Baumgartner, F. Freschi, M. Jaindl, A. Kostinger, Ch. Magele, W. Renhart, M. Repetto, “SMES Optimisation Benchmark Extended: Introducing Pareto Optimal Solutions Into TEAM22”, *IEEE Transaction on Magnetics,* **44** (2008) 1066-1069.

[42] A. H. Moghadasi, H. Heydari, M. Farhadi, “Pareto Optimality for the Design of SMES solenoid Coils verified by Magnetic Field Analysis”, *IEEE Transaction on Magnetics*, **21** (2011) 13-20.

[43] K. Tasaki, M. Takahashi, M. Sakai, T. Kuriyama, Y. Sumiyoshi, H. Kasahata, S. Akita, H. Sakaguchi, “Research and development of superconducting magnetic energy storage system”, *Physica C,* **357-360** (2001) 1319-1322.

[44] H. Hayashi, K. Tsutsumi, K. Funaki, M. Iwakuma, K. Tasaki, Y. Sumiyoshi, M. Tezuka, “Design study of a 1 GJ class HTS-SMES (1) Conceptual design of a magnet system”, *Physica C,* **357-360** (2001) 1327-1331.

[45] T. Dai, Y. Tang, J. Shi, F. Jiao, L. Wang, “Design of a 10 MJ HTS Superconducting magnetic energy storage magnet”, *IEEE Transactions on Applied Superconductivity*, **20** (2010) 1356-1359.

[46] K. Higashikawa, T. Nakamura, K. Shikimachi, N. Hirano, S. Nagaya, T. Kiss, M. Inoue, “Conceptual design of HTS coil for SMES using YBCO coated conductor”, *IEEE Transactions on Applied Superconductivity,* **17** (2007) 1990-1993.

[47] C. Schmidt, “Review of steady state and transient heat transfer in pool boiling helium I”, Stability of superconductors, *International Institute of Refrigeration, Comission,* A 1/2, Saclay, (1981) 17-32.

[48] S G Sydoriak, T R Roberts, “Liquid helium technology”, *Pure and Applied Cryogenics*, *Pergamon,* **6** (1966), 115.

[49] Y Xinjie, “Optimization design of SMES solenoids considering the coil volume and the magnet volume”, *IEEE Transactions on Applied Superconductivity,* **18** (2008) 1517-1520.

[50] E. J. Thomas, C.D. Bright,"Optimizing the design of superconducting solenoids", *Cryogenics,* **6** (1966) 10-13.

[51] P.J. Birkner "On the design of superconducting magnetic energy storage systems", *IEEE Transactions on Applied Superconductivity,* **3** (1993) 246-249.

[52] R. Wesche, "Optimization studies of solenoid windings for superconducting magnetic energy storage", *Cryogenics* **32,** (1992) 578-583.

[53] A. C. Borchi, "Design optimization of micro-superconducting magnetic energy storage system", *IEEE Tranaction on Magnetics,* **35** (1999) 4275-4284.

[54] H. Kohei, N. Taketsune, H. Tsutomu, M. Itsuya, "Design of Bi-2223/Ag coil based on genetic algorithm and finite element method", *IEEE Transactions on Applied Superconductivity,* **15** (2005) 1895-1898.

[55] A. Korpela, J. Lehtonen, R. Mikkonen, "Optimization of HTS superconducting magnetic energy storage volume", *Superconducting Science and Technol*ogy, **16** (2003) 833-837.

[56] R. Storn and K. Price, "Differential evolution-a simple and efficient heuristic for global optimization over continuous spaces", *Journal of Global Optimization,* **11**(1997) 341-359.

[57] P. Bruzzone, "The index n of the voltage-current curve in the charaxterisation, and specification of technical superconductors", *Physica C*, **401** (2004) 7-14.

[58] P Fabbricatore, R Musenich, "Critical measurement of Superconducting cables by the transformer method", Measurement Techniques for the characterisation of SC wires and cables, *Handbook of Applied Superconductivity,* **2** (2010) 325-343.

[59] X. W. Cao, "New methods of selecting the optimum geometrical parameters in the design of superconducting solenoids", *Cryogenics,* **27** (1987) 425-426.

[60] E. J. Thomas, C.D. Bright,"Optimizing the design of superconducting solenoids", *Cryogenics,* **6** (1966) 10-13.

[61] P.J. Birkner, "On the design of superconducting magnetic energy storage systems", *IEEE Transacion of Applied Supercond*uctivity, **3** (1993) 246-249.

[62] Z. X. Feng, "Optimization of superconducting solenoid coils", *IEEE Transaction on Magnetics,* **24** (1988) 926-929.

[63] D. Melville, P G Mattocks, "Stress calculations for high magnetic field coils", *Journal of Physics D: Applied Physics,* **5** (1972) 1745-1759.

[64] E. S. Bobrov, J. E. C. Williams, "Stresses in superconducting solenoids", *Mechanics of Superconducting Structures*, F.C. Moon (ed.), ASME, New York, (1980), 13-41.

[65] L. Velimir, E. Natasa, K. K. Dubravka, “Magnetic field of cylindrical coils”, *American Journal of Phys*ics, **74** (2006) 621-627.

[66] U. Bhunia**,** J. Pradhan, A. Roy, V. Khare, U. S. Panda, A. De, S. Bandopadhaya, T. Bhattacharyya, S. K. Thakur, M. Das, S. Saha, C. Mallik, R. K. Bhandari, “Design, Fabrication and Cryogenic Testing of 0.6 MJ SMES Coil”, *Cryogenics,* **52** (2012) 719-724.

[67] A. J. Middleton, C. W. Trowbridge, “Mechanical stress in large high field magnet coils”, *Proc. 2nd Int. Conf. on Magnet. Tech.*, Oxford, (1967) 140-149.

[68] J. Caldwell, “The circumferential stress in large high field magnet coils”, *Applied Mathematical Modelling,* **4** (1980) 228-229.

[69] V. Arp, “Stresses in superconducting solenoids”, *Journal of Applied Physics,* **48** (1977) 2026-2036.

[70] W. H. Gray, J. K. Ballou, “Electromechanical stress analysis of transversely isotropic solenoids”, *Journal of Applied Physics,* **48** (1977) 3100-3109.

[71] W. D. Markiewicz, M. R. Vaghar, I. R. Dixon, H. Garmestani, “Generalized plane strain analysis of solenoid magnets”, *IEEE Transaction on Magnetics,* **30** (1994) 2233-2236.

[72] J. Kokavec, L. Cesnak, “Mechanical stresses in cylindrical superconducting coils”, *Journal Physics D: Applied Phys*ics, **10** (1977) 1451-1459.

[73] "Ansys Multiphysics", ANSYS v14.0 User's Manual, 2012.

[74] V. T. Picaud, P. Heibel, J. M. Kauffmann, “Superconducting coils quench simulation, the Wilson’s method revisited”, *IEEE Tranaction on Magnetics,* **38** (2002) 1253-1256.

[75] Y. M. Eyssa, W. D. Markiewics, J. Miller, “Quench, thermal and magnetic analysis computer code for superconducting solenoids”, *IEEE Transacion on Applied Supercond*uctivity, **7** (1997) 159-162.

[76] X. L. Guo, F. Y. Xu, L. Wang, M. A. Green, H. Pan, H. Wu, X. K. Liu, A. B. Chen, “Over voltage in a multi-sectioned solenoid during quenching”, *Physica C,* **469** (2009) 1930-1934.

[77] Y. Lvovsky, “Quench energies and stsgnant normal zones in cryostable magnets”, *IEEE Transaction on Applied Superconductivity,* **9** (1999) 261-265.

[78] M. N. Wilson, *Superconducting Magnets*, New York: Oxford University Press (1983) 104-106.

[79] A De, S Kumari, V K Khare, S S Pal, A Sadhukhan, V K Meshram, S K Thakur, S Saha, "Design analysis and implementation of a dynamic voltage restorer", *Journal of Low Power Electronics,* **9** (2013) 340-349.

[80] T. Nast, Hand Book in Cryogenic Engineering, J. P. Weisend ed., Taylor and Francis, Philadelphia (1998) 186.

[81] U. Bhunia, S. Saha, A Chakrabarti, "Design optimisation of superconducting magnetic energy storage coil", *Physica C,* **500** (2014) 25-32.

[82] F. Milano, Power System Modeling and Scripting, Springer Publisher, (2010) 407.

[83] M.S.Lubell, "Superconducting toroidal magnets for fusion feasibility experiments and power reactors", *International cryogenic engineering conference*, Kyoto Japan, (1974) 43.

[84] H.E.Knoepfel, Magnetic fields: A comprehensive theoretical treatise for practical use, John Wiley & Sons, New York (2000) 486.

[85] K. Deb, "Multi-objective optimization using evolutionary algorithm", Singapore: Wiley, 2001.

[86] C. Bellan, G. Bossis, "Field dependence of viscoelastic properties of MR elastomers", *International Journal of Modern Physics B,* **16** (2002) 2447-2453.

[87] Z. Varga, G. Filipcsei and M. Zrınyi, "Magnetic field sensitive functional elastomers with tunable elastic modulus", *Polymer,* **47** (2006) 227-233.

[88] D. F. Ostergaard, "A coupled field finite element for magnetostructural analysis", *Journal of Applied Physics,* **63** (1988) 3185-3187.

[89] Theory reference for the Mechanical APDL and Mechanical Applications, ANSYS, Inc. (2009), ver. 12.0.

[90] P. Chen, Y. Dai, Q. Wang Q, Q. Zhang, "Mechanical behavior Analysis of a 1 MJ SMES Magnet, *IEEE Transaction of Applied Superconductivity,* **20** (2010) 1916-1919.

[91] M. Verrecchia, D. Bessete, N. Mitchell, Y. Krichenkov, "ITER-FEAT central solenoid structural analysis and fatigue life assessment," *Fusion Engineering and Design*, **58-59** (2001) 141-146.

[92] N. Mitchell, "Fatigue assessment of the structural steel in superconducting coils for tokamak," *Fusion Engineering and Design,* **19** (1992) 225-233.

[93] S. S. Manson and M. H. Hirschberg, "Fatigue: An interdisciplinary Approach," *Syracuse University Press*, Syracuse, New York, (1964) 133.

[94] G. E. Dieter, "Mechanical Metallurgy", *Mc Graw Hill Book Company*, (1988).

[95] M. N. Wilson, A. K. Ghosh, B. Haken, W. V. Hassenzahl, J. Kaugerts, G. Moritz, C. Muehle, A. Ouden, R. Soika, P. Wanderer, W. A. J. Wessel, "Cored Rutherford cable for the GSI fast ramping synchrotron", *IEEE Transaction of Applied Supercon*ductivity, **13**(2003) 1704-1709.

[96] C. H. Joshi, Y. Iwasa, "Prediction of current decay and terminal voltage in adiabatic superconducting magnets", *Cryogenics*, **29** (1989) 157.

[97] A. Dudarev, V. E. Keilin, Y. Kuroedov, "Quench protection of very large superconducting magnets", *IEEE Transaction of Applied Supercon*ductivity, **5** (1995) 226-229.

[98] O. P. Anashkin, V. E. Keilin, I. V. Kiriya, A. V. Krivykh, V. V. Lysenko, V. R. Portugalsky, "Superconducting Magnet Protection System", *Advances in Cryogenic Engineering*, **37** (1992) 339.

[99] J. F. Kaerner, "A protection system for small high power SMES with power semiconductors working at cryogenic temperature", *IEEE Transaction of Applied Supercon*ductivity, **5** (1995) 266-269.

[100] S. Noguchi, Y. Oga, H. Igarashi, "Quench simulation of SMES consisting of some superconducting coils", *Physica C,* **471** (2011) 1399-1403.

[101] V. S. Kashikhin, L. Elouadhiri, P. K. Ghoshal, D. Kashy, A. Makarov, O. Pastor, L. Quettier, G. Velev, M. Wiseman, "TORUS CLAS12 - Superconducting Magnet Quench Analysis", *IEEE Transaction of Applied Supercon*ductivity, **24** (2014) 1-5.

[102] OPERA-3D is a FEM package of COBHAM, England.

[103] J. Simkin, S. C. Taylor, E. Xu, A. M. Michaelides, "Coupled transient thermal and electromagnetic finite element analysis for the simulation of quench effects in superconducting magnets", *Journal of Optoelectronics and Advanced Materials,* **10** (2008) 1437-1441.